

***IN-SITU* PHOTOEMISSION STUDY OF ZnO FORMED BY
THERMAL OXIDATION**

Suttinart Noothongkaew



A Thesis Submitted in Partial Fulfillment of the Requirements for the

Degree of Doctor of Philosophy in Physics

Suranaree University of Technology

Academic Year 2010

การศึกษาเชิงคอมพิวเตอร์ที่เกิดจากวิธีเทอร์มอลออกซิเดชันโดยใช้โฟโตมิสชัน
แบบอินซิทู



วิทยานิพนธ์นี้เป็นส่วนหนึ่งของการศึกษาตามหลักสูตรปริญญาวิทยาศาสตรดุษฎีบัณฑิต
สาขาวิชาฟิสิกส์
มหาวิทยาลัยเทคโนโลยีสุรนารี
ปีการศึกษา 2553

***IN-SITU* PHOTOEMISSION STUDY OF ZnO
FORMED BY THERMAL OXIDATION**

Suranaree University of Technology has approved this thesis submitted in partial fulfillment of the requirements for the Degree of Doctor of Philosophy.

Thesis Examining Committee

(Asst. Prof. Dr. Chinorat Kobdaj)

Chairperson

(Assoc. Prof. Dr. Prayoon Songsiriritthigul)

Member (Thesis Advisor)

(Asst. Prof. Dr. Supagorn Rugmai)

Member

(Dr. Saroj Rujirawat)

Member

(Dr. Hideki Nakajima)

Member

(Dr. Wut Dankittikul)

(Assoc. Prof. Dr. Prapun Manyum)

Acting Vice Rector for Academic Affairs Dean of Institute of Science

สุพัตริณาด หนูทองแก้ว : การศึกษาเชิงควมออกไซด์ที่เกิดจากวิธีเทอร์มอลออกซิเดชันโดยใช้
โฟโตอิมิชชันแบบอินซิทู (*IN-SITU PHOTOEMISSION STUDY OF ZnO FORMED BY
THERMAL OXIDATION*) อาจารย์ที่ปรึกษา : รองศาสตราจารย์ ดร.ประยูร ส่งศิริฤทธิกุล,
168 หน้า.

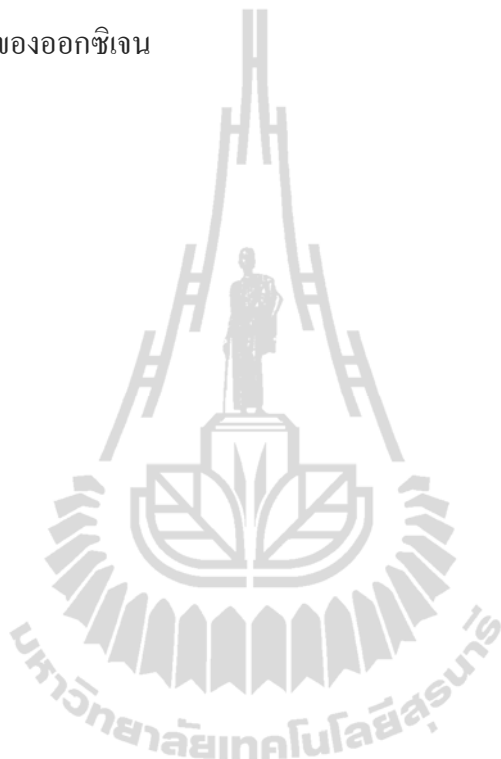
งานวิทยานิพนธ์นี้เป็นการศึกษาการสังเคราะห์เชิงควมออกไซด์ โดยอาศัยเทคนิคการวิเคราะห์
โฟโตอิมิชชันแบบอินซิทูจากแสงซินโครตรอน เทคนิคการเตรียมชั้นของเชิงควมออกไซด์ในงานนี้
ได้แก่นำผิวหน้าสังกะสีที่สะอาดไปให้สัมผัสกับออกซิเจนในสถานะ UHV ที่อุณหภูมิต่ำกว่า 110 องศา
เซลเซียสในบรรยากาศของออกซิเจนที่ความดันต่ำ และการเตรียมโดยอาศัยการลำไอออนพลังงานต่ำ
ทั้งนี้ได้นั้นการศึกษาเชิงควมออกไซด์ที่เตรียมโดยการอบแผ่นสังกะสีบริสุทธิ์ในบรรยากาศของออกซิเจน
ที่ความดันต่ำอย่างเป็นระบบ และการตรวจวิเคราะห์ทั้งเทคนิคโฟโตอิมิชชัน และอเจ็สเปกโทรสโกปี
เป็นแบบอินซิทู เพื่อเลียงปัญหาเกี่ยวกับการปนเปื้อนบริเวณผิวที่ข้อจำกัดของการศึกษาช่วงเริ่มต้น
ของการเกิดเชิงควมออกไซด์ สารตัวอย่างที่เตรียมในบรรยากาศของออกซิเจนที่ความดันต่ำถูกเตรียมใน
ระบบโฟโตอิมิชชันแบบอินซิทูที่มีระดับสุญญากาศ 2×10^{-10} ทอร์รี่ โดยจะมีการทำความสะอาด
แผ่นสังกะสีบางทางเคมีภายนอกระบบวัด และถูกทำความสะอาดในระบบวัดโดยวิธีการที่อาศัยลำ
ไอออนของอาร์กอนพลังงานต่ำ แผ่นบางสังกะสีที่สะอาดถูกสัมผัสกับออกซิเจนที่ถูกปล่อยเข้าไปใน
ระบบวัดจนระดับสุญญากาศอยู่ที่ 5×10^{-7} ทอร์รี่ อุณหภูมิของแผ่นบางขณะการเกิดเชิงควมออกไซด์ถูก
ควบคุมให้อยู่ที่อุณหภูมิห้อง 50 70 90 หรือ 110 องศาเซลเซียส

การศึกษาการเตรียมเชิงควมออกไซด์ ณ อุณหภูมิห้อง โดยให้ผิวที่สะอาดของสังกะสีสัมผัสกับ
แกสออกซิเจนที่ระดับความดันมีค่า 5×10^{-7} ทอร์รี่ เป็นช่วงเวลาที่แตกต่างกันนั้น เชิงควมออกไซด์ที่
เกิดขึ้นศึกษาโดยใช้แสงซินโครตรอน และทำการวัดแบบโฟโตอิมิชชันโดยพิจารณาการเปลี่ยนแปลง
ของสเปกตรัมของสังกะสีที่อยู่ในบรรยากาศของออกซิเจนในแต่ละช่วงเวลาที่แตกต่างกัน พบว่า
กระบวนการเกิดออกซิเดชันจะค่อยๆ เพิ่มอัตราการเกิดออกไซด์อย่างต่อเนื่องจนกระทั่งเข้าสู่ค่าระดับ
ความหนาแน่นหนึ่ง หลังจากนั้นการเกิดออกไซด์จะคงที่หรืออัตราการเกิดออกไซด์ลดลงเข้าสู่ศูนย์ ซึ่ง
จากการเปลี่ยนแปลงของสเปกตรัมที่เกิดขึ้นสามารถนำมาคำนวณระดับความหนาแน่นของฟิล์มบางเชิงควม
ออกไซด์ได้ ซึ่งพบว่ามีค่าความหนาแน่นสูงสุดประมาณ 2 ชั้นอะตอม หรือ 5 อังสตรอม

การศึกษาการเตรียมเชิงควมออกไซด์ ณ อุณหภูมิห้อง 50 70 90 และ 110 องศาเซลเซียส โดยให้
ผิวที่สะอาดของสังกะสีสัมผัสกับแกสออกซิเจนที่ระดับความดันมีค่า 5×10^{-7} ทอร์รี่ พบว่าอัตราการ
เกิดออกซิเดชันบริเวณนี้เกิดขึ้นกำหนดโดยสมการลอการิทึมแบบสองชั้น และหลังจากนั้นอัตราการ
เกิดออกซิเดชันจะเข้าสู่ค่าเป็นศูนย์ที่ระดับความหนาแน่นหนึ่ง ซึ่งขึ้นกับอุณหภูมิของการเกิดออกซิเดชัน
และพบว่าการเกิดออกซิเดชันมีค่าพลังงานกระตุ้นในการเกิดปฏิกิริยาออกซิเดชันเท่ากับ 0.05

อิเล็กตรอนโวลต์ต่อโมล สำหรับขั้นแรกของการเกิดออกซิเดชัน และเท่ากับ 0.081 อิเล็กตรอน โวลต์ต่อโมล สำหรับขั้นที่สอง

นอกจากนี้ได้มีการค้นพบว่า ฟิล์มบางซิงค์ออกไซด์สามารถถูกสังเคราะห์ได้โดยการเหนี่ยวนำด้วยลำไอออนพลังงานต่ำที่ระดมยิงลงบนแผ่นบางสังกะสีที่สะอาด ในบรรยากาศของออกซิเจนที่ความดันที่ 5×10^{-7} ทอร์รี่ หรือที่ระดับต่ำกว่า และพบว่าอัตราการเกิดซิงค์ออกไซด์จะมีค่าเพิ่มขึ้นหากไอออนที่ใช้เป็นไอออนของออกซิเจน



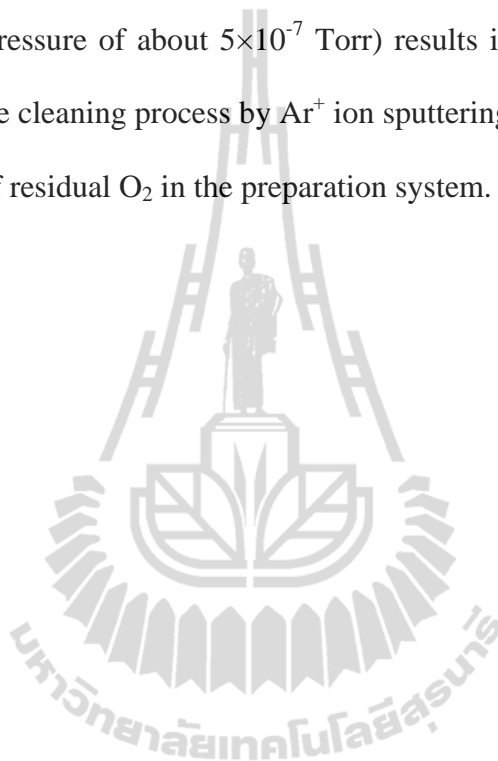
SUTTINART NOOTHONGKAEW : *IN-SITU* PHOTOEMISSION STUDY
OF ZnO FORMED BY THERMAL OXIDATION. THESIS ADVISOR :
ASSOC. PROF. PRAYOON SONGSIRIRITTHIGUL, Ph.D. 168 PP.

ZINC OXIDE / PHOTOEMISSION SPECTROSCOPY / OXIDATION OF ZINC /
SYNCHROTRON RADIATION

The systematic study of the oxidation of zinc has been performed by using *in situ* synchrotron photoemission spectroscopy. This work focuses on the oxide layers formed by exposing clean Zn surface to oxygen in a UHV condition and at temperatures below 110 °C. Polycrystalline Zn foils were used as the substrates. The foils were chemically clean and brought into the preparation of the photoemission spectroscopy. Ar⁺ ion sputtering technique was used to remove surface contaminations before exposing the clean Zn to O₂ at pressure of 5×10^{-7} Torr. PES spectra show that the density of state of the valence band of the Zn foils progressively changes with the oxygen exposure time. The analysis of the spectra allows the determination of ZnO formation. It was found that the oxidation process takes place until reaching the critical thickness, at which the oxidation rate reduces greatly to nearly zero. At the initial oxidation, the oxidation rate follows a two-stage logarithmic equation and later trends to saturate at a certain thickness depending on oxidation temperature. The saturated thickness was determined to be about 2 monolayers or 5 Å for oxidation at room temperature. The saturated thickness was found to increase with oxidation temperature. The two-stage oxidation process may be governed by two kinds of space charge presumably formed in the thin oxide overlayer. At low temperature ranging from room

temperature to 110 °C the activation energies for first and second stage oxidation are 0.05 and 0.081 eV/mol.

The formations of ZnO by ion beam sputtering were studied. It was found that ion bombardment of clean Zn surface with low energy (<3 keV) Ar^+ ions in the presence of O_2 (at pressure of about 5×10^{-7} Torr) results in the formation a thin ZnO overlayer. Thus in the cleaning process by Ar^+ ion sputtering to obtain clean Zn surface, one must be aware of residual O_2 in the preparation system.



School of Physics

Student's Signature_____

Academic Year 2010

Advisor's Signature_____

ACKNOWLEDGMENTS

First of all, I would like to express my gratitude to Assoc. Prof. Dr. Prayoon Songsiriritthigul, my thesis advisor, for his encouragement and endless support. His comments and suggestions helped me to solve the problems. I am also very thankful to Asst. Prof. Dr. Chinorat Kobdaj, Asst. Prof. Dr. Supagorn Rugmai, Dr. Saroj Rujirawat, Dr. Hideki Nakajima, and Dr. Warawat Meevassana, for valuable advice, comments and suggestions for my thesis.

The experimental and mechanical analysis work would have been impossible to finish without Mr. Anusorn Tong-on, Mr. Surachet Rattanasuporn and their groups of Engineering Technicians, these groups set up the optical design of the beam lines.

I would like to thank the Synchrotron Light Research Institute (Public Organization), Ubon Ratchathani University, the Office of the Higher Education Commission and Suranaree University of Technology for financial support.

There are few more people I would like to thank individually. I want to thank Miss Ratchadaporn Supruangnet, Miss. Jarin Osaklung, Miss. Sutassana N Patthalung, Mr. Yutthakarn Ratthanachai, Mr. Thanit Saisopa, and Mr. Phongpan Malaon, for their wonderful friendship, for the great support that they gave me during my Ph.D. studies, and for all the great times we had together.

The last thank you goes to my family; to my mother, my father, my sisters and my brothers, for allowing me to go and make my own mistakes.

CONTENTS

	Page
ABSTRACT IN THAI	I
ABSTRACT IN ENGLISH	III
ACKNOWLEDGEMENTS	V
CONTENTS	VI
LIST OF TABLES	X
LIST OF FIGURES	XI
LIST OF ABBREVIATIONS	XIX
CHAPTER	
I INTRODUCTION	1
1.1 Background	1
1.2 Properties of Zn and ZnO	4
1.2.1 Crystal structure	4
1.2.2 The energy band structure.....	6
1.2.3 Thermal properties	7
1.2.3.1 Thermal-expansion coefficients.....	7
1.2.3.2 Thermal conductivity and specific heat	8
1.2.4 Electrical and optical properties	10
1.3 Material preparation	11
1.4 Oxidation of metals.....	15
1.4.1 Formation of stable metal oxide films at low temperatures.....	16

CONTENTS (Continued)

	Page
1.4.2 Empirical laws of the oxidation rate	18
1.5 Oxidation of Zn	21
II CHARACTERIZATION TECHNIQUES	23
2.1 Photoemission spectroscopy (PES)	23
UPS and XPS spectrum	30
2.2 Auger electron spectroscopy (AES)	32
Elemental sensitivity factors	36
2.3 Surface sensitivity and electron mean free path	37
2.4 Electron energy analyzers	42
2.4.1 Plane mirror analyzer (PMA)	43
2.4.2 Cylindrical mirror analyzer (CMA)	44
2.4.3 Cylindrical deflection analyzer (CDA)	45
2.4.4 Concentric hemispherical analyzer (CHA)	46
2.5 Synchrotron radiation	50
2.5.1 Bending magnet radiation	50
2.5.2 Wavelength shifter and siggler	51
2.5.3 Wiggler magnet radiation	52
2.5.4 Undulator radiation	54
2.6 Background subtraction	56

CONTENTS (Continued)

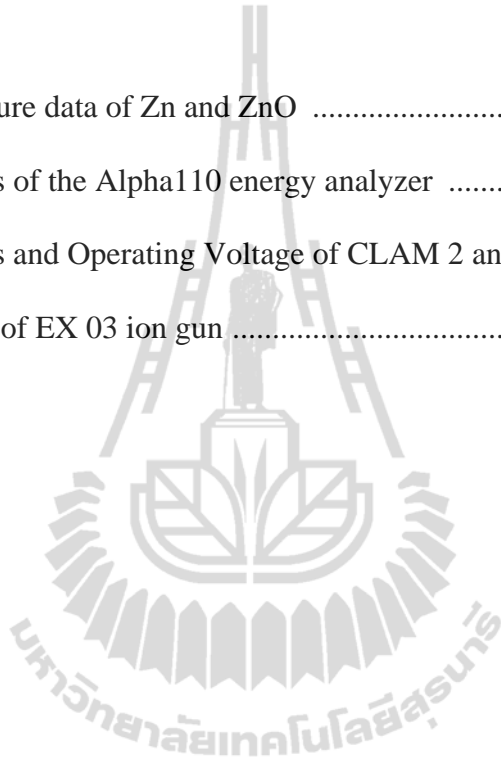
	Page
III INSTRUMENTATIONS AND METHODS	59
3.1 Beamline	59
Photon energy scanning mechanism	63
3.2 Photoemission spectroscopy (PES) beamlines	66
3.2.1 The ARPES system	67
3.2.2 The XPS system	69
3.3 Sample preparation	70
Surface cleaning by ion sputtering	71
3.4 Experimental parameters	72
3.4.1 Temperature	72
3.4.2. Gas flow	72
3.5 Sample holder	73
3.6 Energy analyzer	74
3.6.1 ALPHA110 energy analyzer	74
3.6.2 CLAM2 energy analyzer	77
3.7 Electron gun	79
3.8 Ion gun	80
3.9 AES and PES measurements	82
3.10 Subtract background of photoelectron spectrum	84

CONTENTS (Continued)

	Page
IV RESULTS AND DISCUSSION	86
4.1 PES and AES of Zn foil and ZnO single crystal (0001)	86
4.2 ZnO formed by thermal annealing at 150 °C in air	97
4.3 ZnO formed by sputtering in Ar/O ₂ mixed and O ₂ ambient at room temperature	101
4.4 ZnO formed by O ₂ exposure in UHV environment at room temperature ..	104
4.4.1 Quantitative analysis of PES spectra	115
4.4.2 The thickness of oxide film	117
4.5 ZnO formed by O ₂ exposure in UHV environment at elevated temperatures	128
V CONCLUSIONS	138
REFERENCES	141
APPENDICES	153
CURRICULUM VITAE	168

LIST OF TABLES

Table		Page
1.1	Crystal structure data of Zn and ZnO	6
3.1	Specifications of the Alpha110 energy analyzer	76
3.2	Specifications and Operating Voltage of CLAM 2 analyzer	78
3.3	Specification of EX 03 ion gun	82



LIST OF FIGURES

Figure	Page
1.1 Hexagonal close packing crystal structure of zinc	4
1.2 The hexagonal wurtzite structure of ZnO. Small circles represent Zn atoms while large circles represent O atoms	5
1.3 The LDA band structures of bulk wurtzite ZnO calculated using dominant atomics self-interaction-corrected pseudopotentials (SIC-PP)	7
1.4 Lattice parameters of wurtzite ZnO as a function of temperature	8
1.5 Specific heat of pure and varistor ZnO measured between 1.7 and 25 K	9
2.1 The experimental set up for the photoelectric effect was used by Hallwachs Light emitted from a spark gap passed through the filter (Gips) and the screen (Schirm), impinges on a charged gold-leaf electroscope with connected to the ground body (Erde)	24
2.2 A modern of experimental set-up illustrating PES, monochromatic photon with energy $h\nu$ and polarization are generated by a light source, and directed on the sample. The kinetic energy of the photoelectron can be detected by analyzer	26
2.3 The energy diagrams of the photoemission spectroscopy process. The electron energy distribution produced by incoming photons and measured as a function of the kinetic energy	28
2.4 The three-step model for photoemission: (1) excitation of the electron, (2) electron travel to the surface, and (3) finally escapement	29

LIST OF FIGURES (Continued)

Figure	Page
2.5	A UPS spectrum of a polycrystalline Zn foil taken with 51 eV photons 31
2.6	XPS spectrum of polycrystalline Au for binding energy at $0 \leq E_B \leq 100$, measured with Al-K α radiation ($\hbar\omega = 1487 \text{ eV}$), the Au 5d valence band near the Fermi level ($E_B=0$) and the narrow Au 4f _{7/2, 5/2} core level are clearly seen 31
2.7	The schematic of the experimental setup for basic of Auger electron spectrometer 33
2.8	Schematic diagram of the AES process in basic steps 33
2.9	Auger electron energies for the elements as a function of atomic number, points represent the electron energies of Auger peaks for each element. The larger continuous points represent the most intense peaks 35
2.10	Schematic diagram of an electron emitting from a particular source atom 38
2.11	The probability for an electrons excited at a given depth, $P(d)$ to escape to the surface of the sample 38
2.12	The mean free path of the electrons in solid as a function of their kinetic energy (Hufner 2003) “universal curve” 39
2.13	The probability for an electron to escape from a solid without inelastic energy loss as a function of the depth 41
2.14	The schematic diagram showing the parameters used for considering the probability of any singer photoelectron passing through a thin layer 42

LIST OF FIGURES (Continued)

Figure	Page
2.15 The schematic diagram of PMA	44
2.16 Schematic diagrams of a CMA	45
2.17 Schematic diagram of a CDA showing the angle the cylinder span of 127 degrees	46
2.18 Schematic cross-section of a concentric hemispherical analyzer (CHA)	48
2.19 A hemispherical electron energy analyzer consists of three main parts, a series of lens, analyzer and the detector	49
2.20 Radiation emitted from the bending magnets	51
2.21 The distribution of magnetic field along the beam for a wavelength shifter	52
2.22 Schematic diagram showing the beam divergence of radiation from a bending magnet, a wiggler and an undulator in a storage ring	53
2.23 The calculated flux density as function of a photon energy of radiation generated by a U60 planar undulator, the bending magnet and wavelength shifter at Siam Photon Source	56
2.24 The schematic showing the components of parameter used in the calculation of the Shirley's type background	58
3.1 The photo BL3.2 at the Siam Photon Laboratory	60
3.2 The Optical layout of BL3.2 at the Siam Photon Laboratory	61
3.3 The schematic diagram showing the included angles of the monochromator of BL3.2 at the Siam Photon Laboratory	62

LIST OF FIGURES (Continued)

Figure	Page
3.4	The photo of the grating chamber 65
3.5	Schematic diagram of the sine bar for the rotation of the gratings to scan photon energy at BL3 65
3.6	Show the top-view layout of the photoemission experimental station connected to BL3.2a to utilize undulator radiation 66
3.7	The schematic diagram of the ARPES system at BL3.2a 68
3.8	Schematic diagram of the XPS system at BL3.2a 69
3.9	Show clean Zn foil sheet, a) and Zn foil was spot welded on the molybdenum sample holder, b) 71
3.10	The sample holders are used in the UHV at BL3.2a, a) used in the ARPES chamber, b) used in XPS chamber 73
3.11	Schematic diagram of the ALPHA110 CHA showing the analyzer crosssection and position of Alpha plates 75
3.12	The photo of the ARPES system showing the Alpha110 energy analyzer at BL3.2a of SLRI 76
3.13	Schematic diagram of CLAM2 energy analyzer 77
3.14	The photo of CLAM 2 energy analyzer on the XPSsystem at BL3.2a 78
3.15	Schematic diagram of the LEG63 Electron gun 80
3.16	The photo of the EX 03 ion gun at the PES beamline 81
3.17	Schematics diagram of the EX 03 ion gun 81
3.18	Schematic diagram of PES measurements set-up (ARPES system) 83
3.19	Schematic diagram of PES measurements set-up (XPS system) 84

LIST OF FIGURES (Continued)

Figure	Page
3.20	The photoelectron spectra before and after subtraction of secondary electrons component of the background 85
4.1	Series of photoelectron spectra of zinc foil taken (a) before and (b-g) after surface cleaning by 500 eV Ar ⁺ sputtering for different sputtering times 87
4.2	The first derivative Auger spectra of Zn foil (a) before and (b-d) after sputtering by using 500 eV Ar ⁺ ions 90
4.3	Series of photoelectron spectra of ZnO (0001) spectra before and after sputtering for various times 91
4.4	The first-order derivative of Auger spectra of a single crystal ZnO (0001) sample (a) before and (b)-(d) after sputtering with 500 eV Ar ⁺ ion for various times 93
4.5	Photoemission spectra of a clean Zn foil and a clean single crystal ZnO (0001) 94
4.6	Magified plot of figure 4.5 at the binding energy ranging from 0 to 8.5 eV, below Fermi level 96
4.7	The energy level diagram for the surface of ZnO (a), and an energy band diagram for <i>n</i> -type ZnO semiconductor (b) 96
4.8	The Auger spectra of ZnO formed by thermal oxidation at 150 °C in air for 30 min. The top figures show raw AES spectra, the bottom figure shows the first derivative of AES spectra. The spectra and their derivative are shown for the sample (a) before and after cleaning by Ar ⁺ ion sputtering treatments for 5, 10, and 15 minutes, curves (b) to (d), respectively 98

LIST OF FIGURES (Continued)

Figure	Page
4.9 The Photoelectron spectrum of ZnO formed by thermal oxidation at 150 °C for 30 minutes in air. The figure (a) shows the spectra before cleaning sample, while (b) to (d) show those after sputtering, respectively	100
4.10 PES spectra taken from clean Zn foil before (a) and after sputtering by 3 keV Ar ⁺ ion in an ambient of O ₂ at 5×10 ⁻⁷ Torr (b), 2 keV Ar ⁺ ion in an ambient of O ₂ at 5×10 ⁻⁷ Torr (c), and 1 keV O ⁺ at pressure 1×10 ⁻⁸ Torr O ₂ (d)	101
4.11 The valence band region of the PES spectra taken from a clean Zn foil before (a) and after sputtering by 3 keV Ar ⁺ ion in ambient of O ₂ at 5×10 ⁻⁷ Torr (b), 2 keV Ar ⁺ ion in an ambient of O ₂ at 5×10 ⁻⁷ Torr (c), and 1 keV O ⁺ at pressure 1×10 ⁻⁸ Torr O ₂ (d)	103
4.12 The derivative Auger spectra of clean zinc foil before (a) and after exposure to oxygen with different time exposures varying from 5 to 15 minutes, (b) to (d)	104
4.13 The derivative AES spectra and corresponding concentration of oxygen atom on the surface of the zinc foil; (a) clean surface, (b) after exposure to oxygen for 5 minutes, (c) for 10 minutes, and (d) for 15 minutes	106
4.14 PES spectra of ZnO prepared by thermal methods: The dot curve is for the ZnO formed by thermal annealing at 150 °C in air for 30 minutes, the solid curve is for the ZnO prepared by oxygen exposure in UHV	108
4.15 Zoomed figure 4.14 for ZnO films prepared in air and in UHV environment in the binding energy range of -1 to 8 eV	109

LIST OF FIGURES (Continued)

Figure	Page
4.16 Normalized photoemission spectra of clean surface of Zn foils exposed to oxygen in UHV environment at pressure 5×10^{-7} Torr for various exposure times	112
4.17 Photoelectron spectra in the valence band region for the clean Zn surfaces with out and with oxygen exposure for 15 and 30 min, respectively	113
4.18 Schematic illustration showing the contribution of a photoelectron spectrum taken from a clean Zn after oxygen exposure. Three major photoelectrons are indicated by three different regions, i.e., $I_{Zn\ 3d}$, $I_{O\ 2p\ Zn\ 4s}$, and $I_{Zn\ 4s}$	114
4.19 Schematic drawing showing the variation of sampling depth as function of take off angle in photoemission experiments; (a) normal emission ($\theta=0^\circ$) for greatest depth detection and (b) at shallow take off angles ($\theta>0^\circ$) to increase surface sensitivity	116
4.20 The model used in the calculation of the thickness of oxide film. The thickness of oxide surface was obtained by $n \times d$ in units of angstrom	118
4.21 Calculated ratio of the intensity of Zn 3d photoelectrons emitted from ZnO ($I_{Zn\ 3d_ZnO}$) to the intensity of all Zn 3d electrons ($I_{Zn\ 3d_total}$) as a function of ZnO thickness on thick pure Zn metal	119
4.22 The photoelectron spectra (solid curve) of the samples exposed to oxygen for the exposure times from 5 to 180 minutes, the estimated contribution from Zn metal (dash curve), and the estimated contribution from the ZnO layer (dot curve)	121

LIST OF FIGURES (Continued)

Figure	Page
4.23	The average thickness of ZnO formed on a clean Zn surface as a function of oxygen exposure time 127
4.24	Photoelectron spectra was taken from a clean Zn surface and a Zn surface with a pre-oxidized layer 129
4.25	Photoelectron spectra showing the intensities of the photoelectrons near the Fermi level associated with Zn 4s and Zn 4s-O 2p, (zoom up of figure 4.24) 130
4.26	Photoelectron spectra taken from a Zn foil before and after exposed to oxygen at pressures 5×10^{-7} Torr at the sample temperature of 50 °C for various exposure times 132
4.27	Thickness of the ZnO overlayer after exposing a Zn foil to oxygen at 5×10^{-7} Torr pressures for various exposure times 133
4.28	Thickness of the ZnO overlayer after exposing a Zn foil to oxygen at 5×10^{-7} Torr for various time plotted with logarithm of time 134
4.29	The oxidation rate constant of Zn in O ₂ as a function of the inverse of the temperature (K) 135

LIST OF ABBREVIATIONS

a	major axis of ellipse
a_1, a_2, a_3	spacing parameters
AES	auger electron spectroscopy
A	ampere
A	antiferromagnetic axis
\AA	angstrom
α	(1) twiss parameter, (2) incident angle of mirror and grating, (3) acceptance angle of the electron beam
b	minor axis of ellipse
B	magnetic field amplitude
B_0	peak magnetic field
B_y	magnetic field in the horizontal plane
β	(1) twiss parameter, (2) reflection angle of mirror, (3) diffraction angle of grating
cm	centimeter
CAE	constant analysis energy
CDA	cylindrical deflection analyzer
CHA	concentric hemispherical analyzer
CMA	cylindrical mirror analyzer
CRR	constant retard ration

LIST OF ABBREVIATIONS (Continued)

C_x	the atomic concentration of element x
$^{\circ}\text{C}$	degree Celcius
d	(1) grating groove spacing, (2) slit width of electron energy analyzer and (3) sample thickness
D	diameter
D_x	relative scale factor of element x
ESCA	electron spectroscopy for chemical analysis
$\Delta E/E$	resolution
Δs_1	slit width of the entrance slit
Δs_2	slit width of the exit slit
ΔV	voltage difference between the inner and outer hemispheres of electron energy analyzer
e	electron charge (1.602176×10^{-19} C)
<i>et al.</i>	et alia (and other)
eV	electron-Volt
E_e	electron energy
E_B	binding energy of electron
E_F	The Fermi energy level
E_{KE}	kinetic energy of electron
E_{vac}	the vacuum energy level
$E_{analyzer}^k$	kinetic energy of the electron inside the analyzer

LIST OF ABBREVIATIONS (Continued)

E_p	primary energy of electron
ε	emittance of electron beam
ε_c	critical photon energy
F	optical path function
GeV	gigaelectron volts
γ	the partical energy in units of its rest mass
h	Plank constant
ν	photon energy frequency
I	intensity of the over layer on substrate
I_0	intensity of signal from substrate
I_e	total electron yield
I_x	the peak to peak amplitude of the element x
I_{Ag}	the peak to peak amplitude of the Ag standard
IMPF	inelastic mean free path
κ	thermal conductivity
keV	kiloelectron volts
kW	kilowatts
K	unit of measurement for temperature
K	electron from K -level or core level
L	(1) undulator length, (2) length of the sine-bar
L_1	electron from L_1 - level
L_2	electron from L_2 - level

LIST OF ABBREVIATIONS (Continued)

λ	electron mean free path
m	meter
mm	millimeter
m_0	electron rest mass
mA	milliamperere
M	electron from M -level
μm	micrometer
n	harmonic number of undulator
N	groove density of grating
$N(E)$	electron energy distribution function
$dN(E)/dE$	the differential of Auger spectrum
ϕ	(1) included angle of grating, (2) rotating angle of grating
Φ_{sp}	work function of the spectrometer
p	the momentum of photoelectron
ps	picosecond
$P(d)$	the probability of escape of electron
PES	photoelectron spectroscopy
PEEM	photoemission electron spectroscopy
PMA	plane mirror analyzer
r	source distance
r'	image distance

LIST OF ABBREVIATIONS (Continued)

R	(1) major radius of mirror, (2) linear displacement
RF	radio frequency
R_1, R_2	inner and outer hemisphere of curvature of analyzer
ρ	(1) bending magnet radius, (2) minor radius of mirror
s	second
Sx	sensitivity of element x
SX	soft X-ray
T	tesla
θ	(1) observation angle, (2) incident angle of mirror, (3) deviation angle of grating, (4) incident angle of photon energy
UHV	ultra high vacuum
UPS	ultraviolet photoelectron spectroscopy
UV	ultra violet
U60	undulator of 60 mm of period length
VUV	vacuum ultra violet
XAS	X-ray absorption spectroscopy
XPS	X-ray photoelectron spectroscopy

CHAPTER I

INTRODUCTION

1.1 Background

Zinc oxide (ZnO) is an interesting oxide compound. It is a wide gap semiconductor with a large exciton binding energy of 60 meV and a wide direct gap around 3.27 eV at room temperature (Klinsim, 1975; Chen *et al.*, 2000; Ellmer, 2001; Look, 2001; Djurisic *et al.*, 2002; Look and Claflin, 2004). ZnO crystallizes preferentially in the hexagonal wurtzite structure (space group $P6_3mc$) (Klingshirn, 2007; Ellmer and Klein, 2008) and can be found in nature with the mineral name zincite. Natural ZnO usually contains the small amount of manganese (Mn) and other elements and, thus, its colour varies from yellow to red.

ZnO has a wide range of applications. It has long been used in industry as a major white pigment. It has also been used in other chemistry technology as the material for wet chemical etching (Zheng *et al.*, 2007), low threshold pump power (Gruzintsev *et al.*, 2006) and radiation hardness (Coskun *et al.*, 2004). The most interesting application for ZnO is expected to be in optoelectronics because of its wide direct band gap, corresponding to a photon energy of light in the near ultraviolet region. ZnO has fundamental advantages over GaN (Hufner, 2003). The performance of different types of devices such as sensors, UV laser diodes and flat screen displays may be improved from using ZnO.

The studies of ZnO has begun as early as since 1935 by Bunn (1935) because of its applications in industry, particularly, as a major white pigment. Systematic investigations on ZnO as a compound semiconductor have started after the invention of the transistor (Ellmer and Klein, 2008). The discovery of the good piezoelectric properties of ZnO in 1960 (Hutson, 1960) has led to the first electronic application of ZnO as a thin layer for surface acoustic wave devices in 1976 (Hickernell, 1976). Intensive research activities were carried out on bulk ZnO around the end of the seventies and the beginning of the eighties. Then the interest in ZnO faded because of two main reasons. Firstly, it was not possible at that time to synthesize good quality single crystal *p*-type ZnO. This prevented fabricating *p-n* junction in ZnO, limiting this compound material to be used as optoelectronics devices. Secondly, the interest in semiconductor research shifted to reduced dimensional structures such as quantum wells, which were exclusively based on III-V compound semiconductor materials (Ellmer and Klein, 2008). In the last decade, there was again renewed research interest in ZnO as a semiconducting material because there are reports on *p*-type conductivity, dilute ferromagnetic properties, thin film oxide field effect transistor and rapid progress in nano-structure fabrication. This results in an enormous increase of the number of publications of ZnO in the last few years.

Recently, the study of ZnO is continuously increasing, but the main challenge is to achieve stable *p*-type ZnO. The unstable *p*-type ZnO is caused by native defects and the self compensations which may occur during doping. If stable *p*-type ZnO can be obtained, ZnO will be outstanding material to be used in many applications such as laser diodes and light emitting diodes. Although high quality ZnO thin films were mainly *n*-type, there are some improvements of *p*-type ZnO thin films in the recent

years. This is the results from the development of different growth techniques in the last two decades. Undoubtedly, thermal oxidation is a low cost and simple technique to grow ZnO thin films. The starting material for thermal oxidation could be pre-deposited Zn films (Cho *et al.*, 1999; Wang *et al.*, 2003; Zhao *et al.*, 2004; Alivov *et al.*, 2005; Li *et al.*, 2005). Thus, this thesis work focuses on thermal oxidation of Zn particularly the initial state of the oxidation, or in other words, the interaction of oxygen with Zn surface atoms. Extensive experimental work on the initial oxidation of Zn was performed using low-energy electron diffraction and Auger electron spectroscopy in 1970s (Briggs, 1975; Unertl and Blakely, 1977; Abbati *et al.*, 1979; Krozer and Kasemo, 1980; Gaineyt and Hopkins, 1981). To our knowledge, there has been a discontinuity of such a work despite some unconfirmed interesting findings.

This work devotes to the investigation of the initial states of ZnO formation and systematic study of thermal oxidation of ZnO by using *in situ* high-resolution synchrotron-photoemission measurements of clean Zn surfaces exposed to oxygen in an ultra-high vacuum (UHV) environment.

1.2 Properties of Zn and ZnO

1.2.1 Crystal structure

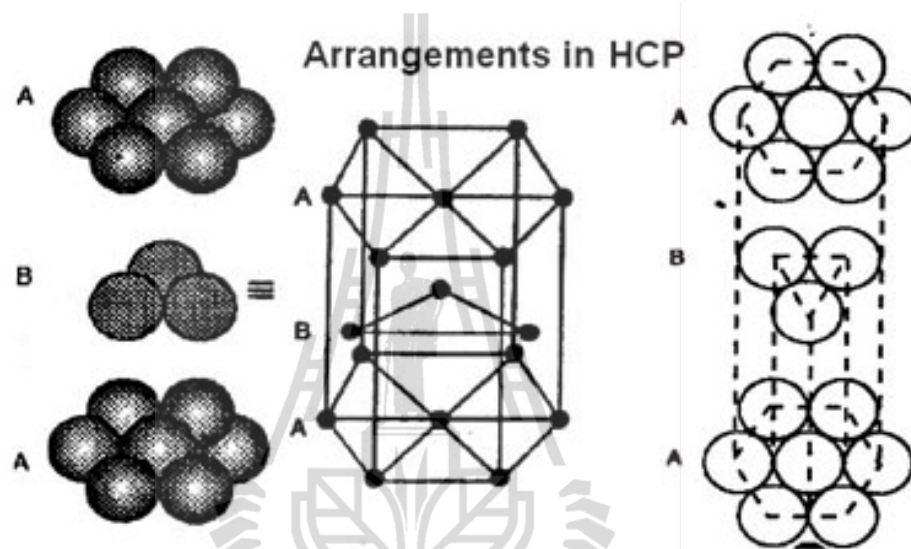


Figure 1.1 Hexagonal close packing crystal structure of zinc.

Zinc (Zn) is metallic solid. It has hexagonal close packing (*hcp*) crystal structure with an atomic ground state configuration $3d^{10}4s^2$ and axes $a = 2.66 \text{ \AA}$, $c = 4.94 \text{ \AA}$ as show in Figure 1.1. The first and second atomic planes are labeled with A and B, respectively. The third plane is directly over the first plane (or A) and succeeding planes are stacked in the repeating pattern ABABA... = (AB).

ZnO is a II-VI compound semiconductor. It has been observed in three crystal structures; wurtzite (B4), zinc blende (B3), and rocksalt (B1). Under atmospheric pressure, the stable phase of ZnO is wurtzite. The zinc blende structure can be stabilized by growing on certain cubic substrates. The rocksalt structure is a stable phase at high pressure.

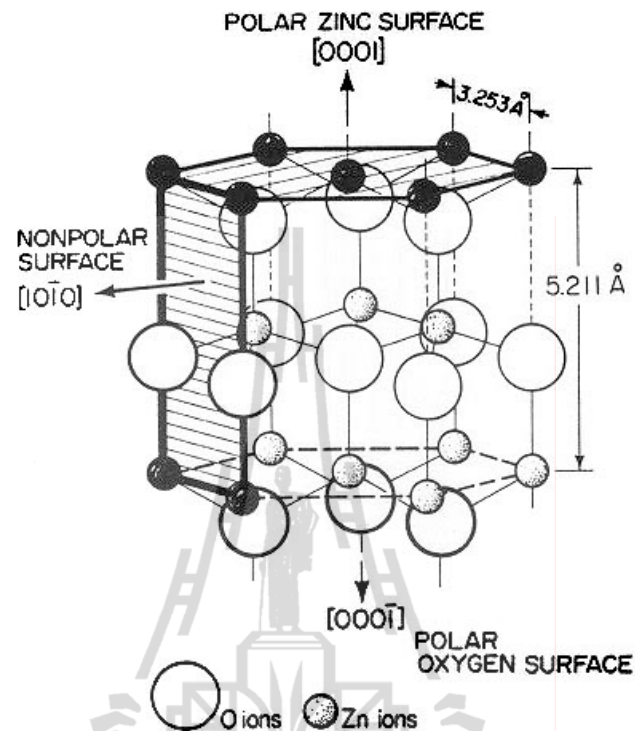


Figure 1.2 The hexagonal wurtzite structure of ZnO. Small circles represent Zn atoms while large circles represent O atoms (Gopel *et al.*, 1982).

Figure 1.2 shows the hexagonal wurtzite structure of ZnO. The conventional bulk unit cell contains two zinc cations and two oxygen anions. The crystal can be viewed as a sequence of O-Zn double layers which are stacked along the c axis or along the (0001) direction. The lattice parameters a and c of the hexagonal unit cell are 3.253 Å and 5.211 Å, respectively. The ZnO crystal exhibits several typical surface orientations. In the conventional labeling, (0001) refers to the surface terminated by Zn atoms, while (000 $\bar{1}$) refers to the surface terminated by oxygen atoms. The summary of crystal structure of Zn and ZnO are given in Table 1.1.

Table 1.1 Crystal structure data of Zn and ZnO.

Crystal structure	Zn	ZnO
Space group	P6 ₃ mc	P6 ₃ mc
Structure	hcp (hexagonal close-packed)	hexagonal wurtzite
Cell parameters	<ul style="list-style-type: none"> • a: 2.66 Å • b: 2.66 Å • c: 4.94 Å • α: 90.000° • β: 90.000° • γ: 120.000° 	<ul style="list-style-type: none"> • a: 3.25 Å • b: 3.25 Å • c: 5.207 Å • α: 90.000° • β: 90.000° • γ: 120.000°
Physical properties		
Melting point	419.53 °C	1975 °C
Density (near r.t.)	7.14 g/cm ³	5.606 g/cm ³

1.2.2 The energy band structure

The electronic properties of materials are governed by the energy band structure. Figure 1.3 shows the energy band structure of ZnO calculated by Jaffe *et al.* (2000). In the calculations, the local density approximation (LDA) and incorporating atomics self-interaction corrected pseudopotentials (SIC-PP) was employed to account for the Zn 3d electrons (Vogel *et al.*, 1995). The band structure is shown along high symmetry lines in the hexagonal Brillouin zone. Both the valence band maxima and the lowest conduction band minima occur at the Γ point $k=0$ indicating that ZnO is a direct band gap semiconductor. The bottom 10 bands (occurring around -9 eV) correspond to Zn 3d levels. The next 6 bands from -5 eV to 0 eV correspond to O 2p bonding state. The first two conduction band states are strongly Zn localized and correspond to empty Zn 4s levels.

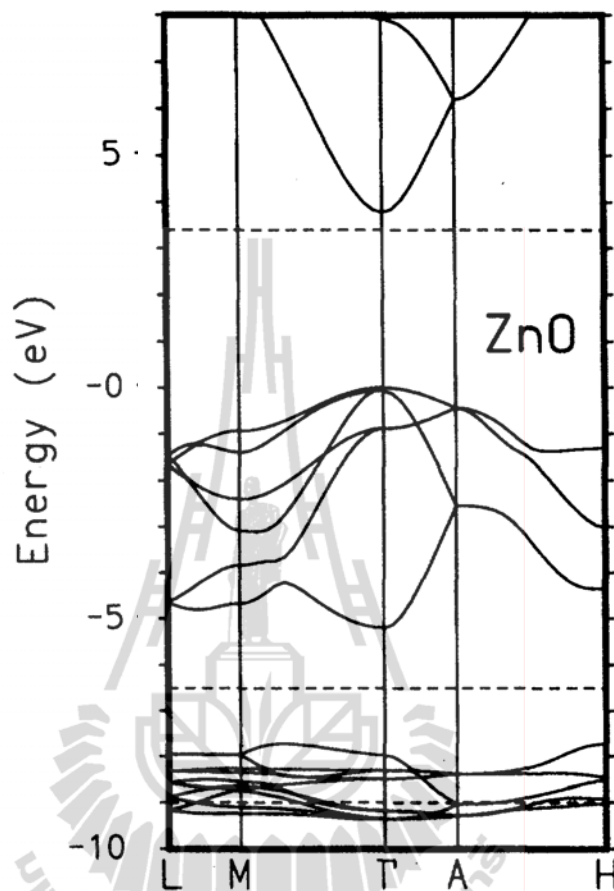


Figure 1.3 The LDA band structures of bulk wurtzite ZnO calculated using dominant atomics self-interaction-corrected pseudopotentials (SIC-PP) (Vogel *et al.*, 1995).

1.2.3 Thermal properties

1.2.3.1 Thermal-expansion coefficients

The thermal expansion coefficients of semiconductors describe the lattice parameters as a function of temperature. Reeber (1970) performed extensive X-ray powder diffraction study on powder ZnO in the temperature range of 4.2-296 K, and obtained the results of the lattice parameters as shown in Figure 1.4. The thermal properties of ZnO thin films have been investigated more recently by Yung Han *et al.*

(1995). It was found that the thermal expansion coefficient of ZnO thin films prepared by RF-magnetron sputtering on Si and GaAs depends on the deposition conditions such as the gas pressure and the substrate temperature. The thermal expansion coefficient of wurtzite ZnO has been reported to have the value in between 5×10^{-6} and $8 \times 10^{-6} \text{ K}^{-1}$ (Han and Jou, 1995). While the thermal expansion coefficient for the zinc blende and rocksalt phase of ZnO are reported to be $1.24 \times 10^{-5} \text{ K}^{-1}$ and $0.16 \times 10^{-5} \text{ K}^{-1}$, respectively (Aoumeur *et al.*, 2003).

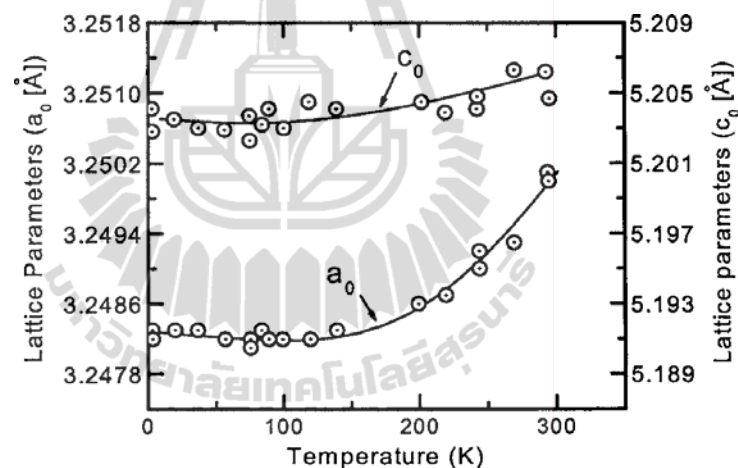


Figure 1.4 Lattice parameters of wurtzite ZnO as a function of temperature (Reeber, 1970).

1.2.3.2 Thermal conductivity and specific heat

Thermal conductivity, κ , is one of the properties to be considered when ZnO is used for high power electronic and optoelectronic devices. For bulk ZnO, there is a small difference in the thermal conductivity at room temperature for different surfaces ZnO (0001), i.e., with Zn terminated surface, shows the thermal conductivity a few

percent higher than ZnO (000 $\bar{1}$), i.e., with O terminated surface (1.16 ± 0.08 W/cmK vs 1.10 ± 0.09 W/cmK) (Florescu *et al.*, 2002). These values are higher than other values reported on ZnO.

The specific heat of materials is related to the lattice vibrations, free carriers, and point and extended defects. Lawless and Gupta (1986) investigated the specific heat of pure ZnO and varistor ZnO, which are ceramics based on heavily doped ZnO, at low temperatures (between 1.7 and 25 K). Specific heat measurements were performed using the pulse method. Figure 1.5 shows that the specific heats of pure and varistor ZnO diverge below 20 K. It can be assumed that the difference in the specific heat is due to the impurities and defects contributions.

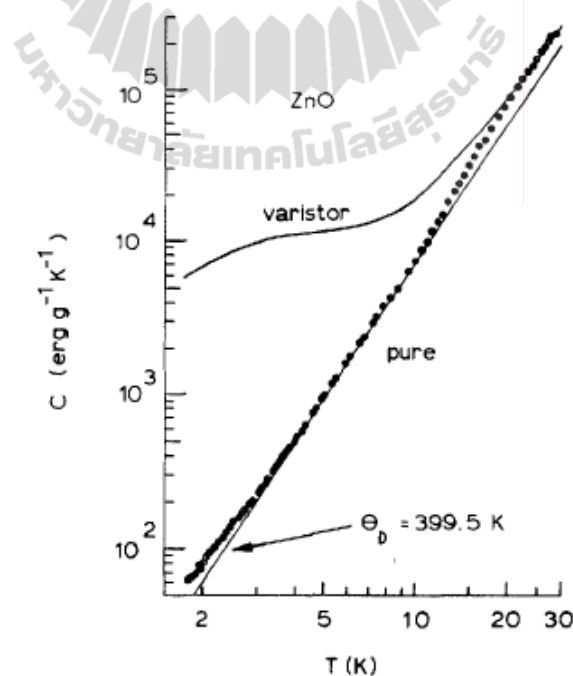


Figure 1.5 Specific heat of pure and varistor ZnO measured between 1.7 and 25 K (Lawless and Gupta, 1986).

1.2.4 Electrical and optical properties

The main driving force for research on ZnO as a semiconducting material is its wide and direct band gap and large exciton binding energy. These properties make it suitable for variety of electronic and optoelectronic applications. For example, a device made by materials with a large band gap has a high breakdown voltage, lower noise generation, and can operate at high temperatures with high operation power. The performance of electron transport in semiconductor is different at low and high electric field. At low electric field, the energy distribution of electrons in ZnO is almost unaffected. This is because the electron cannot gain much energy from the applied field relative to their thermal energy. Therefore the electron mobility is almost constant because the scattering rate does not change much.

Because of the wide band gap, ZnO is transparent in the visible light region with a sharp cut-off in the UV region. This region corresponds to the photon wavelength of 0.3 and 2.5 μm . ZnO is a promising material as a transparent conductive window layer in solar cells. This layer should allow most of the light to pass through to the underlying layer. Under the optimum conditions for depositing ZnO thin film, the transmission of $\sim 90\%$ may be achieved. The transmission and reflection of ZnO in the visible region can be controlled by controlling the doping parameter of ZnO, such as type and concentration of dopants. Sarkar *et al.* (1991) were studies on the electro-optical properties of indium doped zinc oxide (ZnO:In) films produced by the magnetron sputtering technique. The results also show that, the optical band gap was found to slightly increase with the doping concentration, as a function of $N^{2/3}$ (Sarkar *et al.*, 1991).

1.3 Material preparation

ZnO can be prepared by several techniques, such as chemical vapor deposition (CVD), sol-gel, molecular beam epitaxy (MBE), spray pyrolysis, metalorganic chemical vapor deposition (MOCVD), sputtering, thermal oxidation, RF and DC magnetron sputtering, pulsed laser deposition (PLD) (Demian, 1994; Natsume and Sakata, 2000; Look *et al.*, 2002; Nishino and Nosaka, 2004; Liu *et al.*, 2006). High quality *n*-type ZnO could be readily fabricated (Chang *et al.*, 2003). Group III elements such as aluminum, gallium, and indium are normally used as *n*-type dopants of ZnO. Among *n*-type dopants, aluminum was found to be the best for producing ZnO film with high transparency and high conductivity (Chang *et al.*, 2003).

Although, ZnO can easily be obtained as an *n*-type semiconductor, *p*-type ZnO has long been difficult and rarely achieved (Look, 2005). Many attempts have been made to prepare *p*-type ZnO. So far, there were many problems occurring during ZnO preparation processes such as the formation of intrinsic defects, such as oxygen vacancy and Zn interstitial (Joseph *et al.*, 1999). Many different growth techniques and acceptor species have been tried in hope to achieve *p*-type of ZnO. The literature reported that nitrogen is the first candidate and most suitable dopant for producing *p*-type ZnO (Look, 2005). Theoretical works on this topic using first-principles calculations are still contradicting. Earlier study shows that nitrogen could be used to produce shallow *p*-type dopants in ZnO (Kobayashi *et al.*, 1983). However, more recent works, Lyons *et al.* show that N is a very deep acceptor (Lyons *et al.*, 2009). Due to the fact that nitrogen has 5 valence electrons while oxygen has 6 valence electrons when nitrogen replaces oxygen it causes a deficiency of one electron. From experimental point of view, nitrogen doping of ZnO is very practical. Because there

are at least four different gases, namely, N_2 , NO, NO_2 , and N_2O which can easily be used in various vacuum deposition techniques to prepare ZnO thin films

Sato *et al.* (1966) prepared ZnO films on substrates by zinc evaporation in O_2 - N_2 mixed radio-frequency plasmas. Their mixing ratio (N_2/O_2+N_2) was varied from 0% to 100%. They found that the film could be deposited at N_2 mixing ratios within 50% when the substrate temperature was 400 °C, and all of the obtained films were *c*-axis oriented ZnO. While increasing the N_2 mixing ratio, resistivity of the films changed from about 0.1 to 10 $\Omega \cdot cm$. After annealing in air at 450 °C, carrier densities of the films deposited at N_2 mixing ratios under 25% tend to decrease with the N_2 mixing ratio. In contrast, they increased rapidly again when the N_2 mixing ratio is higher.

Futsuhara *et al.* (1998) reported optical properties of zinc oxynitride ($Zn_xO_yN_z$) films prepared with a mixture of argon and nitrogen gases. $Zn_xN_yO_z$ films were deposited onto glass substrates from a ZnO target in N_2 -Ar mixtures by reactive RF magnetron sputtering, and N_2 concentration varied from 0 to 75%. The crystal structures of the films were determined by XRD while chemical bonding states and chemical compositions of the films were analyzed by XPS. The $Zn_xO_yN_z$ films were determined to be polycrystalline with ZnO structure, and their microstructure depended on the nitrogen concentration in the films. The nitrogen concentration in the films was controlled by changing N_2 concentration in the sputtering gas. The $Zn_xO_yN_z$ films showed *n*-type conducting behavior. The photons absorption was found to be via direct transition. The optical band gaps are observed to decrease with nitrogen concentration. The decrease in E_g is probably related to the difference ionicity between Zn-O and Zn-N bonds. According to the Pauling theory (Pauling, 1960)

ionicity in a single bond increases with the difference in values of electron negativity between two elements formed the single bond. The electron negativity of O (3.5) is larger than that of N (3.0), which indicates that the Zn-O bond has larger ionicity than the Zn-N bond. The decrease in E_g is probably attributed to the decrease in ionicity due to the formation of Zn-N bonds. *P*-type ZnO films were not achieved despite the attempts with difference N_2 concentration and difference deposition temperatures (Sato and Sato, 1996; Futsuhara *et al.*, 1998). Computational work using First principle calculations by Limpijumrong *et al.* (2006) showed that H, C and N could passivate N_o acceptors in ZnO. It was demonstrated that the formation of N_2 molecules at O sites $[(N_2)_o]$ and $(NC)_o$ are donor in *p*-type ZnO, indicating that N-doped *p*-type ZnO was not successful. On the other hand, Joseph *et al.* (2001) reported the growth of *p*-type ZnO films by a pulsed laser deposition technique. They used N_2O gas as source of N by passing N_2O (or N_2) with or without carrier gas through an electron cyclotron resonance (ECR) or RF plasma source. The deposition was carried out in a vacuum chamber with base pressure of 1×10^{-8} Torr. During the deposition, the substrate temperature was kept at 400 °C. N_2O gas was believed to prevent O vacancy from occurring and to introduce N as an acceptor, at the same time (Joseph *et al.*, 2001). With Ga and N co-doping technique, they concluded that high resistivity *p*-type ZnO films were obtained by doping with active N alone. The *p*-type conductivity was very much enhanced in terms of conductivity and carrier concentration by a co-doping method (using N as acceptor and Ga as donor dopants). In addition, N doping was effective only with N_2O through an ECR plasma source but not with N_2 gas. The two steps growth, with using high temperature template layer, was quite effective to get well crystallized ZnO films growth at low temperature.

Liang *et al.* (2005) reported the preparation of *p*-type ZnO thin films by plasma molecular epitaxy (P-MBE) using NO as both O and N dopant sources. They found that the reproducible *p*-type ZnO has a minimum resistivity of 9.36 Ω and hole concentration as high as $1.2 \times 10^{18} \text{ cm}^{-3}$. The results from the optical emission spectra of the radical N₂ and NO, it may conclude that, atomic N is suitable for *p*-type ZnO.

Cao *et al.* (2008) prepared *p*-type ZnO by using NH₃ plasma post-treated ZnO thin films. In their method, ZnO films were grown on the α -Al₂O₃ substrate by MBE. NH₃ plasma post treated was operated at low temperature in plasma enhanced chemical vapor deposition (PECVD) system with high purity NH₃ serving as the nitrogen source. The *p*-type ZnO conductivity was obtained by the Hall-effect measurement. The hole density of treated films is $2.2 \times 10^{16} \text{ cm}^{-3}$. During the treatment process nitrogen could incorporate into oxygen positions to compensate some donors, resulting in the transformation from *n*-type to *p*-type.

Although current ZnO research activities are emphasized essentially on the nanostructures, new growth, doping techniques and its applications. However, in term of the structure and growth mechanisms of zinc oxide films a thickness of only a few monolayers (called sub-oxide layers) are of special interest. This is due to the fact that the sub-oxide layers are believed to be precursors for formation of oxide nuclei and subsequent thick oxide film growth. Thus, investigations of the initial stage of the oxidation of Zn might lead to a better understanding of ZnO growth mechanism.

1.4 Oxidation of metals

The studies of the oxidation of metals have long been reported for many years ago. The efforts of scientists have been motivated by both the fundamental interest of the oxidation mechanism and its technology importance. Several good publications and literatures on oxidation of metals are available, for examples, the oxidation of metal films by nitrous oxide (Isa and Saleh, 1971), the oxidation of iron and influence of an electric field at room temperature (Bhavani and Vaidyan, 1981), the oxidation of cadmium (Rossi and Braicovich, 1979), and the oxidation kinetics of aluminide coatings on alloy (Xiang *et al.*, 2006). Most metals are oxidized under suitable conditions and, more importantly, metal oxides show promising properties for technological applications.

The necessity for clean conditions and careful surface preparation for studies in the early stages of oxidation has been known for many years. The initial stages of the oxidation process are usually very sensitive to the conditions of the surface that depend on the cleanliness of surface, gaseous environment, the purity of the metal, the roughness of the surface and surface orientation. The initial stage of oxidation is indeed very complex. It may be either physical or chemical process (Mott and Cabrera, 1947, 1948-49). Physical adsorption occurs with all gas surface combination at sufficiently low temperatures and/or high enough pressures, whereas chemisorption can take place at temperatures well above the boiling point of the gas and will therefore be important for the oxidation process under most conditions of temperature and pressure. Chemisorption is a chemical reaction and involves the rearrangement of valence electrons of the metal and the gas to form a chemical bond. However, recently, both the theoretical and experimental studies of the oxidation of metals have

provided general in-depth information and guidelines for further investigations. As the oxidation mechanism is complicated, all theoretical guidelines has not yet been examined or proved.

1.4.1 Formation of stable metal oxide films at low temperatures

The formation of metal oxides films with thickness less than 100 Å has extensively been investigated by different research groups, for examples, Kubaschewski and Hopkins (1962), Robersts (1962), Hauffe (1965), Lawless (1965), and Fehlner and Mott (1970, 1971). Experimental results from those investigations of the oxidation of various metals, by exposing the metals to oxygen at low temperatures, show that the oxidations of different metals share similar mechanism. At sufficiently low temperature, it is possible to carry out the investigation of the initial growth of the oxides. During the initial stage, the oxidation occurs very rapidly. After that, the oxidation rate drops to very low or negligible values. Normally, a stable oxide film with a thickness of 20-100 Å is finally obtained. Metallic aluminium with a clean surface exposed to air at room temperature, for example, forms a stable alumina oxide with a thickness of about 40-50 Å, while the formation of stable oxides of iron, copper, barium, and other metals occur at the temperature of liquid air. The behaviour of the oxidation process was first explained by Mott (1947a). Earlier, Mott (1939a, 1940) has developed the basic concepts for the growth of thin films by assuming that metal ions and electrons diffuse passing through the oxide layer and then react with the oxygen at the oxide gas interface. The explanation by Mott is given as the followings. Metal ions can travel through the oxide via two possible ways; by the outward movement of interstitials or the inward movement of cation

vacancies. Both cases may depend on the type of the oxide formed. For very thin films with the thickness less than 50 Å, electrons could pass through the film by the quantum mechanical tunneling effect. The probability of the electron incident on a barrier of height V and width x , would penetrate the barrier was given by

$$p = p_0 \exp\left[-\frac{4\pi x}{h}(2mV)^{1/2}\right], \quad (1.1)$$

where p_0 is a numerical factor approximately equal to unity for every thin film with thickness less than 20 Å. Since electrons can cross the oxide layer by the tunnelling effect, as then they can be used up to form oxygen ions. For thicker films of the thickness between 30 and 40 Å, the ions can pass through the thin films rather than electrons, resulting from the presumably slower rate of penetration of electrons. Thus the oxidation growth rate is controlled by the tunnelling effect controlled, and is given by

$$\frac{dx}{dt} = C' \exp\left[\frac{4\pi x}{h}(2mV)^{1/2}\right] = C' \exp\left(-\frac{x}{x_0}\right), \quad (1.2)$$

where $C' \sim 10^7 \text{ cm s}^{-1}$ and $x_0 = \left(\frac{h}{4\pi}\right)(2mV)^{1/2}$. The equation can be integrated to provide a logarithmic law of growth in term of

$$x = A \ln(Bt + 1) \quad (1.3)$$

where x is the thickness of oxide in Angstrom units, t is time in minutes, while A and B are constants. If a thickness of oxide films greater than 50 Å, the tunnelling effect is less effective and the growth essentially stops unless the temperature is sufficiently high.

1.4.2 Empirical laws of the oxidation rate

Several empirical laws have been proposed to explain the time variation of the oxidation of metals, particularly, at high temperature. The three most important laws are the linear law, the parabolic law, and the logarithmic law. In 1922, Tammann *et al.* reported that the interference color changed on the surface of a zinc sample, when heated to 400 °C in air. The oxidation rate was deduced from the color change, and could be explained by the law of exponential, which is given by;

$$t = Ae^{by} - A, \quad (1.4)$$

where y is the film thickness, as obtained from the observation of interference colours on the sample, t is time, and A and b are constants. Later, the linear and parabolic rate laws were proposed by Pilling and Bedworth (1923) to explain the rate of oxidation of cadmium, copper zinc, and other metals at high temperatures. These laws were applied to a particular reaction depending on the Pilling-Bedworth ratio of the molecular volume of the metallic oxide to the molecular volume of the metal. This ratio was determined by Md/mD . Where M and D are the molecular weight and its density of the oxide, respectively, m is the molecular weight of the metal, and d is its density of the metal). If the ratio is less than one, ($Md/mD < 1$), it may be assumed that the oxide coat is porous or may not stick to the surface of the metal; and a linear rate law defines the rate of oxidation.

$$y = kt + A, \quad (1.5)$$

if this ratio is greater than one, ($Md/mD > 1$), the oxide coat adheres to the metal, and an oxide film is formed; time is defined by a parabolic rate law which is given by

$$y^2 = kt + A, \quad (1.6)$$

In equations (1.5) and (1.6), k is a constant and the other symbols are the same as defined for equation (1.4). These two laws were used to explain the rate of oxidation on the basis that the rate limiting factor during reaction was diffusion of some species in the reaction coat. Other researchers have proposed similar explanations using these two laws such as Wangner and Grunewald (1938), Mott (1940). An empirical rate law proposed by Bangham and Stafford (1925) is given as;

$$\frac{dy}{dt} = kt^{-(1-A)} \quad (1.7)$$

This equation was fitted to the data obtained for the reaction of oxygen at zinc oxide surfaces at temperatures below 400 °C. This equation was extended to explain oxidation at lower temperatures by Vernon *et al.* in 1939. For the oxidation temperatures in the range between 25 °C and 400 °C, it was found that the reaction time followed a logarithmic law given by;

$$W = k \log(at + c) \quad (1.8)$$

where, W is weight gain due to the oxide film, t is time, while k , a , and, c are constants. For c is equal to unity, W is equal to y (y is a thickness of oxide film), this law is the same as that of $y = k \ln(Bt + 1)$ which was firstly determined by Tammann and Koster reported in 1922. Thus, this law was proposed independently by a group of Tammann in 1922 and Vernon and in 1939. The logarithmic law was pioneered by Tammann. His work was obtained the experimental results by using a simple color method. These results were not considered highly accurate. Consequently, the importance of this law was considered by the work of Vernon. Although, the oxidation rate laws are still not well established, however, these three laws are quite

often used to explain the oxidation of metal. Those three laws may be summarized as followed:

The Linear Law: The oxidation rate is governed by the equation $y = kt + A$. This law applies when the films formed on metals are porous or non-continuous, or in those cases where the film falls completely away from the metal as it is formed. Thus, a continually renewed metallic surface is available for reaction.

The Parabolic Law: The oxidation rate is governed by the equation $y^2 = kt + A$. This law applies when the oxidation rate of a metal is controlled by diffusion of ions and by migration of electrons or positive holes through the oxide film.

The Logarithmic Law: The oxidation rate is governed by the equation $y = k \ln(Bt + 1)$. This law applies when the oxidation occurs in the lower temperature range or when thin films are formed. In general, the increasing of oxide films can be explained by using the logarithmic law with time, except that, when the films thickness is greater than about 10 \AA , several breaks have been found in the oxidation curve. The logarithmic equation was first defined by Tammann *et al.* in 1922. Since then the initial oxidation behaviors of many metals have been explained by the logarithmic equation under specific condition of temperature and time. In the literature the logarithmic laws have been used to explain; the oxidation kinetics of zinc (Vincent and Uhlig, 1965), oxidation kinetics of copper in the thin film range (Krishanmoorthy and Sircar, 1969), the oxidation of metal films by nitrous oxide (Isa and Saleh, 1971), the oxidation of titanium in the temperature range between 25 and $400 \text{ }^\circ\text{C}$ (Smith, 1973), the oxidation of iron at room temperature (Bhavani and Vaidyan, 1981), aluminide (Xiang *et al.*, 2006), and many other reports which are not

mentioned here. Note that, for a metal oxide, two laws have been commonly found to explain the oxidation process. Those are the parabolic law and the logarithmic law.

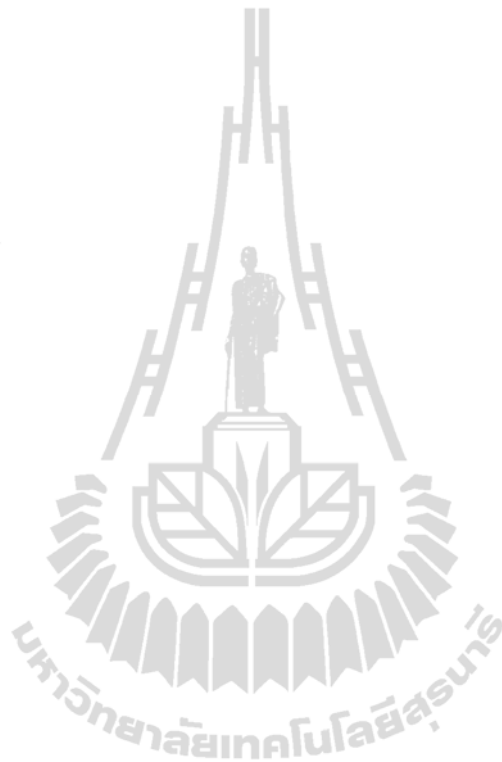
1.5 Oxidation of Zn

Metallic Zn does not indicate any catalytic activity under reaction conditions. This is in contrast to ZnO which exhibits a unique physical property and a high activity for chemisorption of gas such as hydrogen and carbon monoxide. Generally, the oxidation of Zn is very simple chemical reaction which is given by (L'vov *et al.*, 2004).



Therefore, the oxidation of Zn has been extensively studied both experimentally and theoretically. Extensive experimental works on the initial oxidation of Zn were performed using electron spectroscopy and low-energy electron diffraction (Briggs, 1975; Unertl and Blakely, 1977; Abbati *et al.*, 1979; Krozer and Kasemo, 1980; Gaineyt and Hopkins, 1981). The growth rate of ZnO increased linearly with increasing pressure. The rate is independent of temperature over the range from 77 to 425 K. The obtained ZnO was polycrystalline or amorphous in structure (Unertl and Blakely, 1977). It was also found that the surface of zinc during oxidation was heterogeneous and consisted of ZnO islands and intermediate regions of chemisorbed oxygen (Briggs, 1975). A model of the oxidation was proposed that there is competition between oxygen diffusion into the bulk and oxygen retention at the sample surface with the formation of the oxide phase (Abbati *et al.*, 1979). While the theoretical study of oxygen chemisorption on Zn surface has been reported by Miyazaki in 1983. After that, to our knowledge, the activities on the studies of the

oxidations of Zn were stopped, due to the difficulty to synthesis *p*-type ZnO and the shift of semiconductor research to reduced dimensional structures based on III-V compound semiconductor.



CHAPTER II

CHARACTERIZATION TECHNIQUES

The investigations of the initial stage of oxidation process of metals require an ultra-high vacuum (UHV) environment and surface sensitive measurement techniques. More importantly, the measurements used in the investigations should be performed *in situ*. The measurement techniques employed in this work are electron spectroscopic techniques, i.e., photoemission spectroscopy (PES). PES is generally known as X-ray/ultraviolet photoelectron spectroscopy (XPS/UPS) and Auger electron spectroscopy (AES). This thesis work was carried out at the photoemission experimental station of the synchrotron beamlines BL3.2a and BL4 (old beamline) at the Synchrotron Light Research Institute (SLRI). This chapter provides basic information necessary for the electron spectroscopic techniques.

2.1 Photoemission spectroscopy (PES)

PES is a technique to measure the spectra of photoelectrons emitting from the atoms in the materials excited by electromagnetic wave from the UV to X-rays regions. It is a direct and powerful technique to obtain the electronic structures of matters. In addition, chemical information of the materials such as elemental and chemical compositions may be deduced from photoelectron spectra. It should be noted that PES is a surface sensitive technique. This is because of a short escape depth of electrons in solids, mentioned below. Historically, emission of electrons from solids

caused by the interaction of light and matter has long been observed, and is a phenomenon well known today as the photoelectric effect. The phenomenon was first discovered by Heinrich Hertz (at Karlsruhe) and Wilhelm Hallwachs (at Dreshen) in 1887 (Reinert and Hufner, 2005). The experimental set up is illustrated in Figure 2.1. They observed that negative charge was removed from a solid when its surface is irradiated by UV light, and thus the positive charge was built up on the irradiated metals. When the UV light impinges on the metallic plate of a charge electroscope, the negative charge current could be detected. It should be noted that the electron was not discovered yet at that time. The explanation of the phenomenon was not comprehended at the time of the discovery.

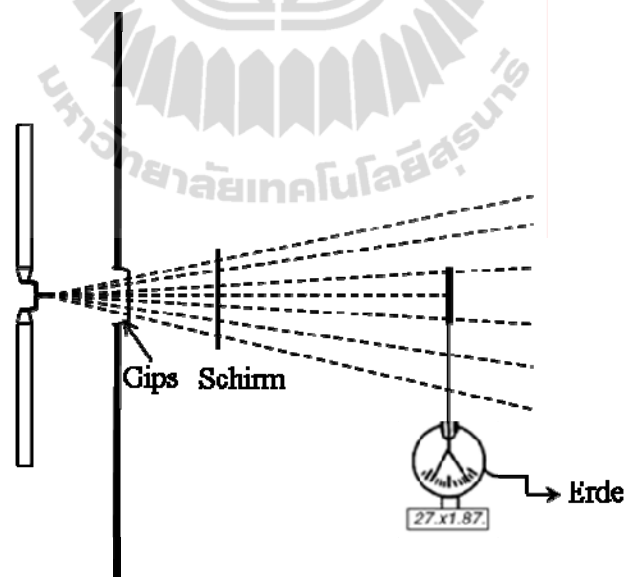


Figure 2.1 The experimental set up for the photoelectric effect used by Hallwachs (Hallwachs, 1916). Light emitted from a spark gap pass through the filter (Gips) and the screen (Schirm), impinges on a charged gold-leaf electroscope with connected to the ground body (Erde).

The explanation of the photoelectric emission on the quantum nature of light was proposed by Einstein in 1905. He introduced the concept of the photon. With the energy conservation law, he could find the relationship between the photon energy (which is directly proportional to the frequency of light) and the kinetic energy of the emitted electrons. The relation between the intensity of light and the number of emitted electrons could also be well explained. The photoemission spectroscopic technique performed today is still based on the same principle of photoelectric effect existing for over a hundred years ago. However, the advances in the instrumentations allow us to performed PES experiment with better resolution and higher sensitivity. The resolution of the electron energy analyzer has been push to the limit of technology, and that energy resolution of about 1 meV is now possible. In addition to a UV discharge lamp and a laboratory X-ray tube, a synchrotron light source provides tenability of photon energy, high brilliant light and controllable various types of polarization.

From the early day of PES, the technique was used intensively for chemical analysis, and thus ESCA (electron spectroscopy for chemical analysis) was known. ESCA, also known as XPS (X-ray photoelectron spectroscopy) employs characteristic X-rays caused by bombarding of energetic electrons on a metallic anode (mainly aluminium and magnesium). The photon energy for K_{α} X-ray lines for aluminium and magnesium are 1486.7 and 1253.6 eV, respectively. In ESCA or XPS, the excitation energy is well suited to obtain the binding energy of core electrons in solids. In order to obtain information of valence electrons, lower excitation energy is used. The most common excitations are He-I (21.22 eV) and He-II (40.8 eV) lines from a discharged lamp. These excitations fall in the UV region, and thus the technique is called UPS

(ultraviolet photoelectron spectroscopy). Synchrotron light sources provide great flexibility to PES because of its salient properties such as the continuous spectrum covering from infrared to hard X-rays, high brilliance, controllable polarization and pulse times structure. Thus, there are variations of PES techniques, for examples, angle- and/or spin resolved PES, core level PES (or ESCA/XPS), valence band PES (or USP), imaging PES (or imaging/micro XPS).

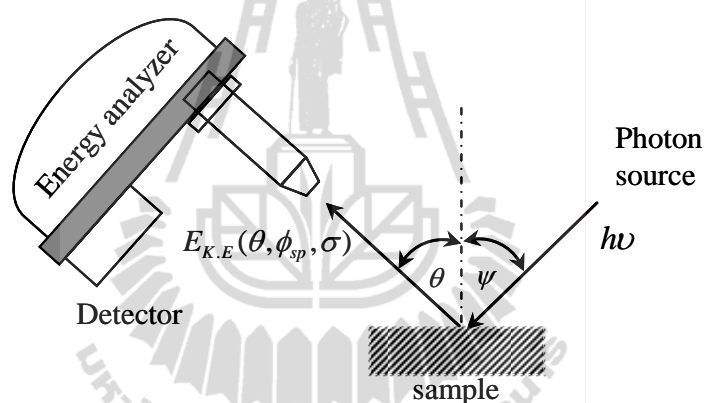


Figure 2.2 A modern of experimental set-up illustrating PES, monochromatic photon with energy $h\nu$ and polarization are generated by a light source, and directed on the sample. The kinetic energy of the photoelectron can be detected by the energy analyzer.

Figure 2.2 illustrate an experimental set-up for PES experiments. The basic principle for PES measurements is as the following. When light with sufficient photon energy impinges on a solid sample with an angle of incidence of ψ , photon energy is absorbed and photoelectrons are emitted from the surface of the sample with a maximum kinetic energy is given by equation (2.1),

$$E_{K.E.}^{\max} = h\nu - \phi_{sa}, \quad (2.1)$$

where, ν is the photon frequency while ϕ_{sa} is the work function of the sample. The kinetic energy $E_{K.E.}$ of the photoelectrons is analyzed with respect to the emission angle and kinetic energy by an electron energy analyzer. From the measurement, the binding energy of the photoelectron can be obtained through the law of energy conservation, which is given as

$$E_{K.E.} = \hbar\omega - \phi_{sp} - |E_B|, \quad (2.2)$$

$$E_{K.E.} = \frac{p^2}{2m}; p = \sqrt{2mE_{K.E.}}, \quad (2.3)$$

where, $\hbar\omega$ is photon energy, eV, E_B is the binding energy, and ϕ_{sp} is the spectrometer work function. The magnitude of the momentum can be obtained when the kinetic energy $E_{K.E.}$ of the photoelectron is known, thru a simple relation between energy and momentum, i.e., $p = \sqrt{2mE_{K.E.}}$. The emission angle of the photoelectrons provides additional information of their momentum p (*wave vector* $k = p/\hbar$). The component parallel and perpendicular to the sample are obtained from the polar (ν) and azimuthal (φ) emission angles.

The fundamental principle of the photoemission process is graphically illustrated in Figure 2.3. The figure shows the relation between the energy level diagram and the energy distribution of electrons produced by light with photon energy of $\hbar\omega$. The electrons in the solid sample associate to either core levels or valence band. The binding energy of electrons in solids is measured with respect to the Fermi level while the binding energy of electrons in free atoms or molecules is measured

with respect to the vacuum level. For a metallic sample, the Fermi energy E_F is located at the top of the valence band and has an energy separation by ϕ_{sp} from the vacuum level E_{vac} . If photon absorption occurs in a core level with binding energy E_B , the photoelectron can be detected with their kinetic energy $E_{K.E.} = \hbar\omega - \phi_{sp} - |E_B|$ in the vacuum level. Notice that binding energy is equal to zero at E_F ($E_B=0$ at E_F) and the kinetic energy in vacuum is measured with respect to E_{vac} while in a solid the physical reference is E_F . In actual data accumulation, the reference point for molecules and atoms is taken to be E_{vac} , while in solids E_F is taken as the “natural” which is zero. The natural abscissa for the photoelectron is the kinetic energy with its zero at the vacuum level of the sample.

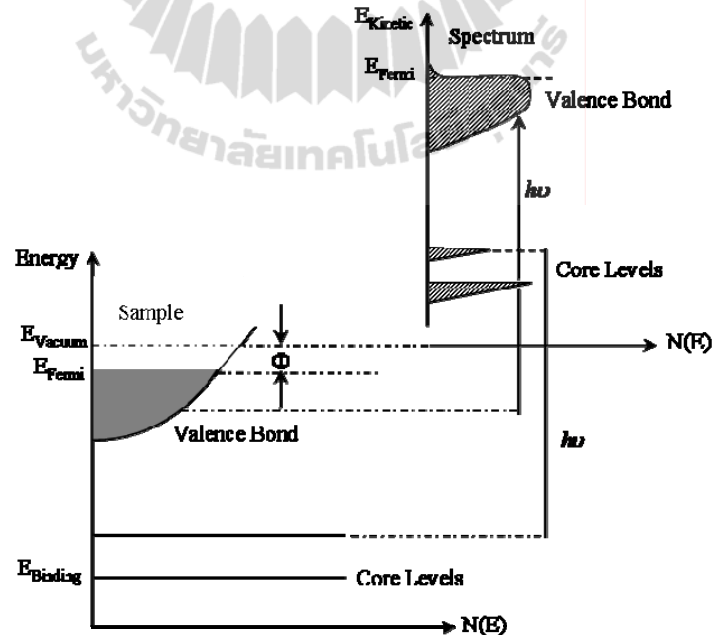


Figure 2.3 The energy diagrams of the photoemission spectroscopy process. The electron energy distribution produced by incoming photons and measured as a function of the kinetic energy.

It is interesting to briefly mention about the photoemission processes that necessary as a theoretical guideline for detailed calculations. The most accepted model for explaining photoemission phenomenon is the three-step model. The model is illustrated in Figure 2.4. It involves three steps, i.e.,

- (1) The photo-ionization step, the photon is absorbed and an electron is excited.
- (2) The electron travels through the sample to the surface.
- (3) The electron will escape from the surface into vacuum if it still has the kinetic energy higher than the work function of the sample, where it is detected.

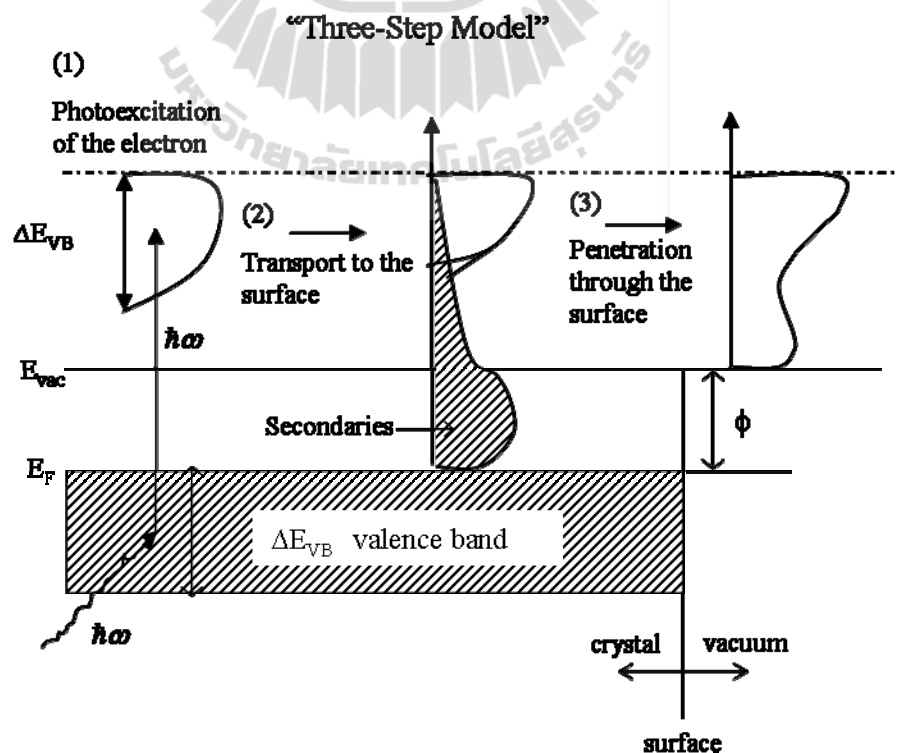


Figure 2.4 The three-step model for photoemission: (1) excitation of the electron, (2) electron travel to the surface, and (3) finally escapement (Hufner, 2003).

UPS and XPS spectrum

The photoemission experiments in the early times were carried out by several groups starting from the early 1960s. The first success activity on UPS (ultraviolet photoelectron spectroscopy) was reported by the groups of Spicer (Stanford). They measured the valence band spectrum on copper (Cu) (Spicer and Berglund, 1964) and they proposed the three-step model (Berglund and Spicer, 1964) as illustrated in the Figure 2.4. The group of Turner *et al.* (1970) performed UPS on gases using a type of VUV excitation source which is differentially pumped gas discharge lamp that until today is commonly used in UPS setups. The structure in the valence band is best achieved at lower photon energies because of both the superior energy and momentum resolution. Figure 2.5 shows a PES spectrum of a polycrystalline Zn foil taken with photon energy 51 eV at normal electron emission angle at the BL4 beamline of the Siam Photon Laboratory. It is clearly shown that the binding energy is located at 0-2.5 near the Fermi level it is the flat 4s valence band. The binding energy is located between 9 and 11.3 eV it is the structure 3d band. This energy is measured with respect to the Fermi energy at $E_F=0$ eV.

XPS technique has extensively been developed by the group of Siegbahn in Uppsala. The main propose was to study of core level binding energies of solids (Nordling *et al.*, 1957). A typical XPS spectrum is shown in Figure 2.6. This figure shows intensity of photoelectrons of polycrystalline gold as a function of the binding energy was taken with $\hbar\omega = 1487\text{eV}(AlK\alpha)$. It clearly shows the (5d6s) valence band close to the Fermi level and the 5p and 4f core levels. Usually, the Au 4f levels are used to as a reference to calibrate the position of the Fermi level. The Au 4f levels are located at binding energy 84.0 ± 0.1 eV ($4f_{7/2}$) and 87.7 ± 0.1 eV ($4f_{5/2}$) below the E_F .

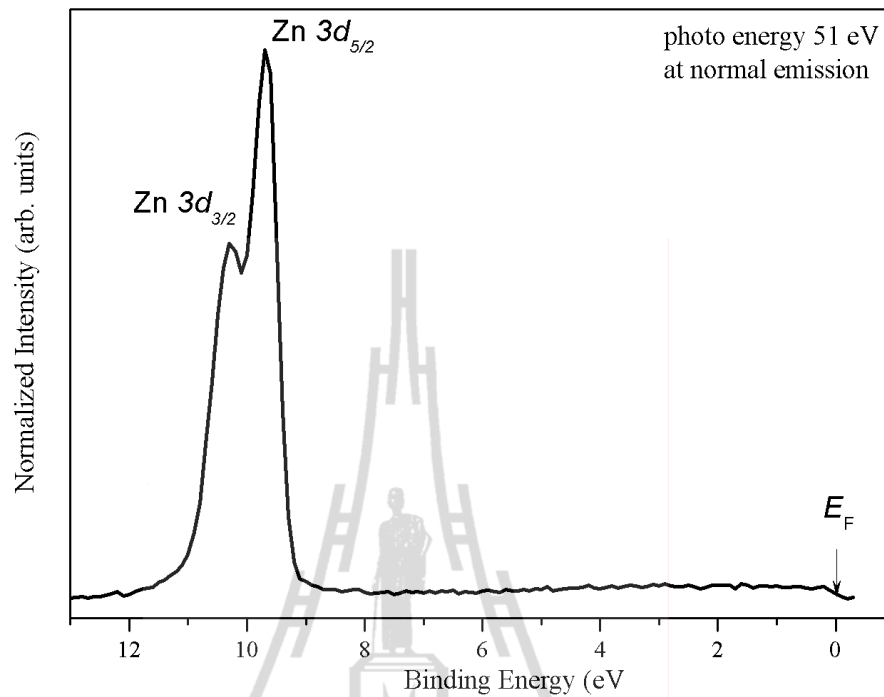


Figure 2.5 A UPS spectrum of a polycrystalline Zn foil taken with 51 eV photons.

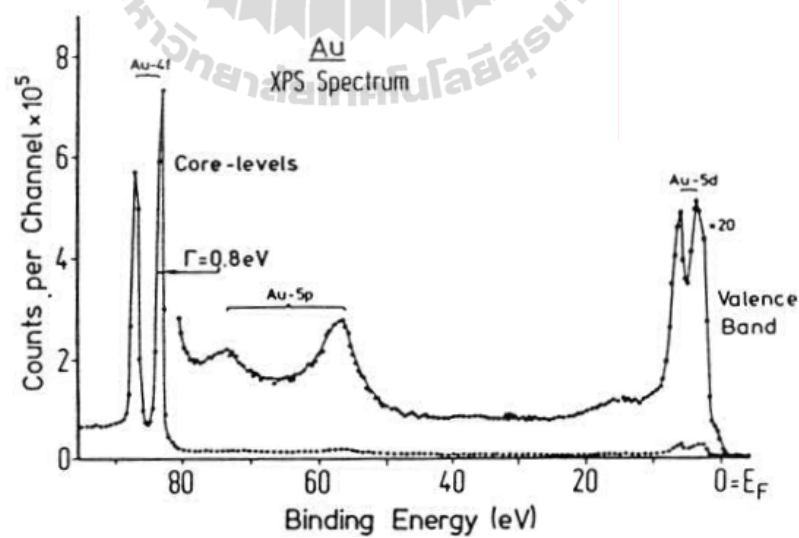


Figure 2.6 XPS spectrum of polycrystalline Au for binding energy at $0 \leq E_B \leq 100$, measured with Al- K_α radiation ($\hbar\omega = 1487$ eV), the Au 5d valence band near the Fermi level ($E_B = 0$) and the narrow Au $4f_{7/2, 5/2}$ core level are clearly seen (Nordling *et al.*, 1957).

It is important to note that XPS is a surface sensitive technique. The region studied by XPS is only from the surface and extending $\sim 30\text{-}50 \text{ \AA}$ maximum into the bulk, depending on materials. This limitation is governed by the fact that photoelectrons emitted from the greater depths suffer energy loss by inelastic scattering processes.

2.2 Auger electron spectroscopy (AES)

The Auger effect was discovered by Pierre Auger in the 1925 during his experiments with X-ray. He observed the ejected Auger electron from along a beam of X-ray. AES is one of several techniques is widely used in surface analysis for obtaining the chemical composition of solid surfaces. This technique is a surface sensitive spectroscopy for chemical analysis in a few nanometers (or $5 \text{ to } 20 \text{ \AA}$) near the surface regions (Chourasia and Chopra, 2004), and it can detect all elements above helium.

The schematic of the experimental setup for basic AES is shown in Figure 2.7. The electrons from an electron gun impinge onto the sample surface and then the secondary electrons are emitted from surface subsequently. The emitting electrons are energy-analyzed an electron spectrometer. This experiment is necessary to carry out under UHV condition because it is limited by the mean free path of electrons in the kinetic energy range of 20 to 2500 eV. The main components of an AES spectrometer are;

- 1) UHV environment
- 2) Electron gun
- 3) Electron energy analyzer

4) Data recording and output system

AES process can be considered by the following three basic steps;

- 1) Atom ionization (the ionization energy to remove core electrons)
- 2) Electron emission (the Auger process)
- 3) Analysis of the emitted Auger electrons

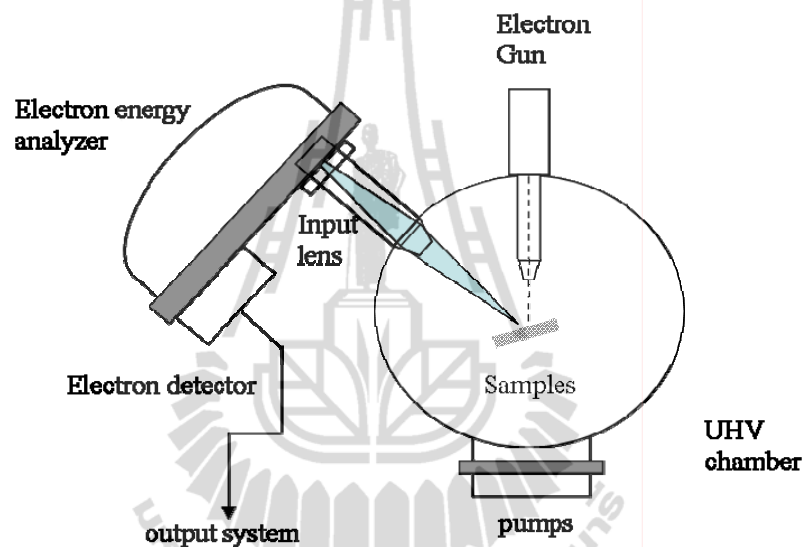


Figure 2.7 The schematic of the experimental setup for basic of Auger electron spectrometer.

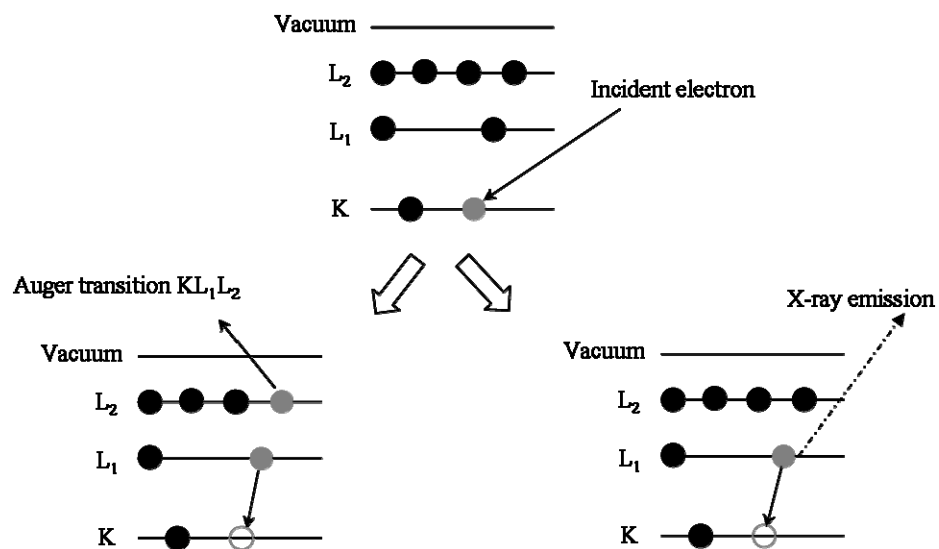


Figure 2.8 Schematic diagram of the AES process in basic steps.

The competing between the AES process and X-ray emission process are shown schematically in the Figure 2.8. The initial state of AES process is initiated by the ionization process of an atom under electron bombardment. If the incident energy of primary electron E_p (typically having a primary energy in the range 2-10 keV) is higher than the ionization threshold of the core level, the atom is ionized by removing an electron from a core level. After the removal of an electron from core level, of course, the upper level electron (L_1) will immediately fall to a lower level (in the K - level). When electron from L_1 drops into the K level by one of two ways which may occur in the process; X-ray fluorescence or Auger emission. In this process, the energy ($E_K - E_{L_1}$) is simultaneously transferred to a second electron, as in the L_2 level. This electron is ejected from the atom as an Auger electron. The kinetic energy of the Auger electron is give by the equation below;

$$KE = E_K - E_{L_1} - E_{L_2} - \phi, \quad (2.4)$$

where, ϕ is the work function. It is obvious there are three electronic levels involve in an Auger process. Thus there are several possible Auger transitions such as KL_1L_1 , KL_1L_2 , LM_1M_2 . It is obvious that at least two state and three electrons are involved in the Auger process therefore neither H nor He can be detected with Auger technique. AES technique can be used for detecting elements from Li on up in the periodic table of elements. The kinetic energy of Auger electron is in the range between 0 and 2400 eV, (see in the Figure 2.9). The escape depth of electrons is localized to within a few nanometers from the surface. AES is a high surface sensitivity due to the short mean free path of the electrons. In general at low energies auger emission and x-ray emission, they are indistinguishable between Auger and

X-ray emissions. Auger electrons are detected by an electrons spectrometer. These electrons show small peaks in the total energy distribution function $N(E)$. Due to Auger peaks are superimposed on a large continuous background, therefore the Auger signals are detected by differentiating the energy distribution function $N(E)$ which can remove the large background. Thus the differential of spectrum is the function $dN(E)/dE$. Usually, Auger spectrum of an element in derivative mode plotted as a function of electron energy (eV).

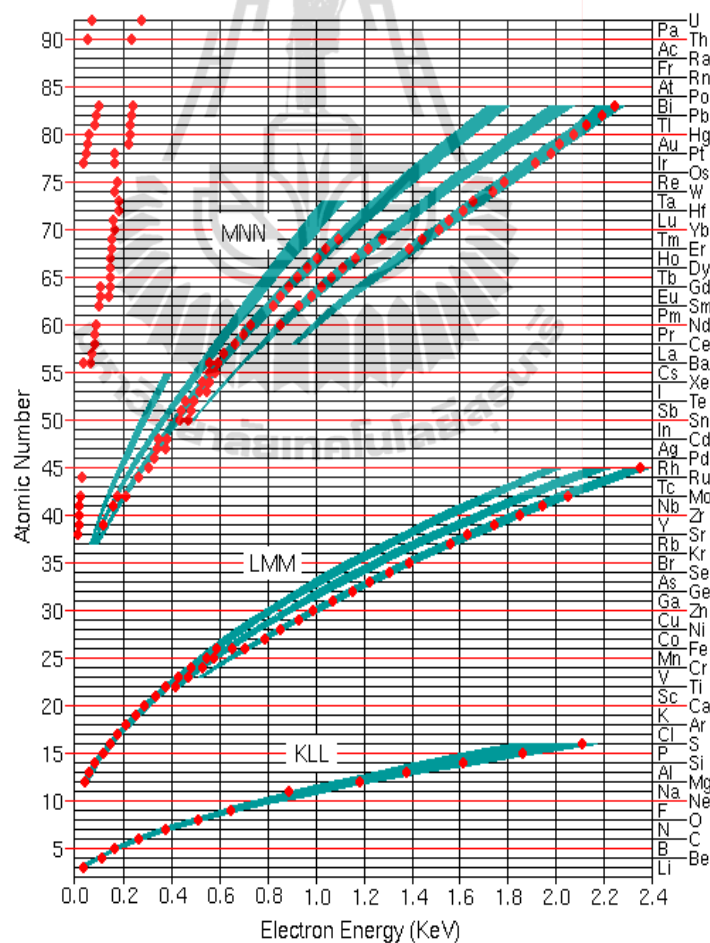


Figure 2.9 Auger electron energies for the elements as a function of atomic number, points represent the electron energies of Auger peaks for each element. The larger continuous points represent the most intense peaks (Carlson, 1975).

Elemental sensitivity factors

In quantitative surface analysis by AES, it is assumed that the surface composition of the sample is homogeneous within the near surface region. Elemental sensitivity factors are widely used in AES quantitative analysis. The atomic concentration (C) of an element x in a sample can be determined from the following equation.

$$C_x = \frac{I_x/S_x}{\sum_{i=1..n} (I_i/S_i)}, \quad (2.5)$$

where, I_x and I_i are the intensity of the Auger signal of element x, (from the unknown specimen), and pure element standard, i, respectively. S_x and S_i are the relative sensitivity of element x and pure element standard, i, respectively. The summation (Σ) is the ratio of all other elements which are present in the sample, i is number of elements. If the variations in the backscattering factor and escape depth in material is not considered, or neglect. The result of this method is considered semi-quantitative. For the main advantage of this method, the standards and insensitivity to surface roughness are neglected. In order to avoid the large number of pure element standards, so the AES signal from the specimen is compared with the AES signal from a pure silver (A_g) target. Thus, the elemental sensitivity factors relative to silver can be easily used in equation (2.5). It is necessary to use the sensitivity factor on the peak to peak height, due to the data are finally showed in the differential mode. This method can use only when the peak shape is invariant with the matrix. Thereby, the atomic concentration of element x is determined by

$$C_x = \frac{I_x}{I_{A_g} S_x D_x} \quad (2.6)$$

where, I_x and I_{Ag} are the peak-to-peak amplitude of the element x from the test specimen, and from the Ag standard, respectively. D_x represents a relative scale factor between the spectra for the test specimen and silver.

2.3 Surface sensitivity and electron mean free path

A surface sensitivity of technique is the technique that is sensitive to atoms which are located near the surface of sample than atoms located in the bulk. It means that, the main part of signals of atoms comes from the surface region within a few atomic layers, while the signal comes from much deeper into the bulk of solid is small. The surface sensitivity must occur from the emission and detection of photoelectrons emitted from the surface. If only those electrons which can pass through the surface, at the same time, when they leave from the solid, their initial energy (E_0) are detected. In XPS experiments, photoelectrons emitting from the sample will be considered. In practices, these electrons will appear to be peaks in the photoelectron spectra. If the photoelectrons lose their energy due to inelastic scattering process, they will contribute to the background. During an electron is travelling through the solid, it can lose some energy by “inelastic scattering”. The inelastic scattering process could lead to two cases; firstly, a reduction in the electron energy, secondly, a change in the direction of travel. Figure 2.10 illustrates the possible trajectories of electrons which are emitted from a particular source atom. It shows that the black arrows are electrons traveling with their initial energy, E_0 , while the dash-dot arrows are electrons trajectories after to an inelastic scattering process. Only the black traces they extend out of the solid and there are corresponding to electron which would be detected by the detector.

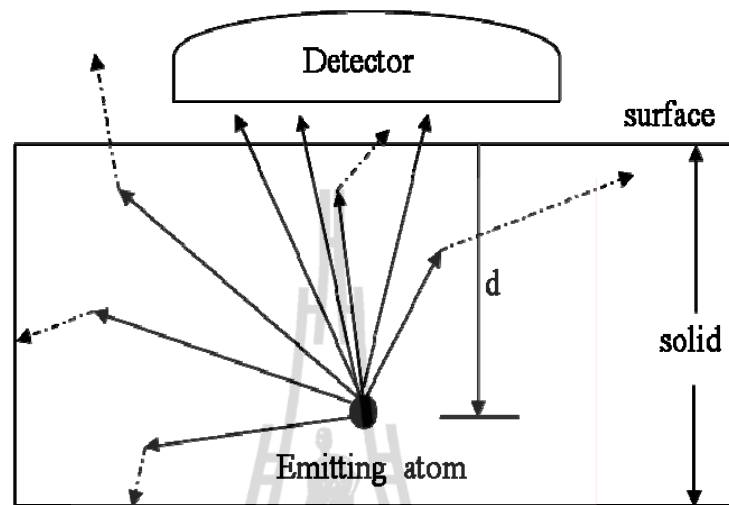


Figure 2.10 Schematic diagram of an electron emitting from a particular source atom.

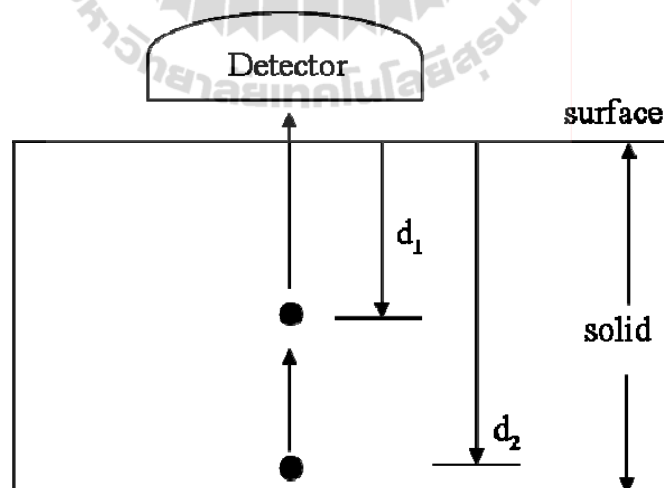


Figure 2.11 The probability for an electrons excited at a given depth, $P(d)$ to escape to the surface of the sample.

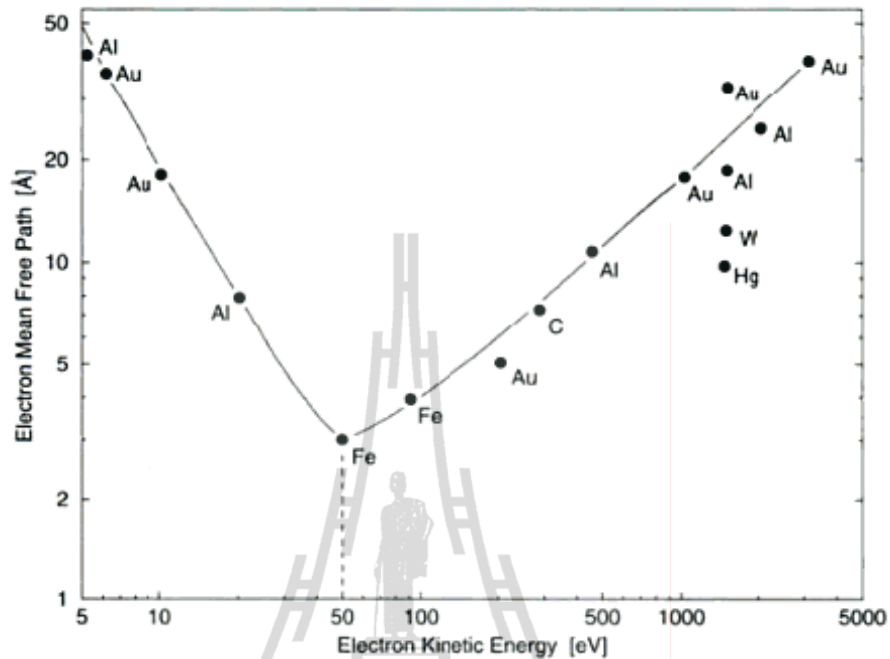


Figure 2.12 The mean free path of the electrons in solid as a function of their kinetic energy (Hufner, 2003) “universal curve”.

For surface spectroscopy, it is widely useful to specify the advantages of electrons as compare to photons, atoms or ions because electrons have found the widest application as the following

- 1) The escape depth of electrons is only a few Å and electrons are suited to study electronic states in the surface region of a sample.
- 2) The energy of electrons easily tunable by electric fields and there are easily focused.
- 3) Electrons are easily to detect and count.
- 4) Electron is easy to analyze the energy and the angle by using electrostatic fields.
- 5) Electrons have been detected after that they were vanish.

Of course, working with electrons, there are some disadvantages, such as; firstly, the problem to obtaining an excellent vacuum in the experiment, secondly, it difficult to distinguish between surface and bulk properties of surface if electrons, there are very small escape depth.

Recently, the mean free path or the inelastic mean free path has been investigated intensively for establishing electron spectroscopy, such as in particular PES (namely XPS or ESCA), as a quantitative analytical tool. PES is a surface sensitive technique. The most generally accepted way to achieve surface sensitivity is the determination of the escape depth of exited electrons. The average distance for an electron traveling in matters without losing its energy by inelastic scattering is called the “inelastic mean free path” IMFP, or λ . The mean free path for unscattered photoelectrons is characterized by a minimum of approximately 5 Å at kinetic energy between 20 and 100 eV. In most XPS experiments, the kinetic energy of photoelectrons is in the range between ~10 and 2000 eV. Those photoelectrons have a maximum IMFP of ~20 Å. Thus detected photoelectrons, appearing as peaks in the photoelectron spectra, are emitted from the region below the surface with the maximum depth of less than ~20 Å. With a tunable light source, the kinetic of the interested photoelectron can be chosen to have the minimum value of IMFP to allow PES to be sensitive to the surface.

The probability for a photoelectron emitted at the depth d to travel to the surface without energy loss due to inelastic scattering is given by

$$P(d) = \exp(-d/\lambda) \quad (2.7)$$

where, λ is the IMFP for the photoelectron with kinetic energy E . The probability for electrons to escape without inelastic scattering, $P(d)$, is shown as a graph in Figure

2.13. It is clear that the $P(d)$ decreases very rapidly and goes to zero at a distance $d > 5\lambda$. The majority of electrons escaping from the sample without inelastic loss come from a distance, $d = 1\lambda$ (63%), and 23% of electrons come from 2λ , while 9% of electrons come from 3λ . All of electrons (>95%) were detected coming from within 3λ of the surface.

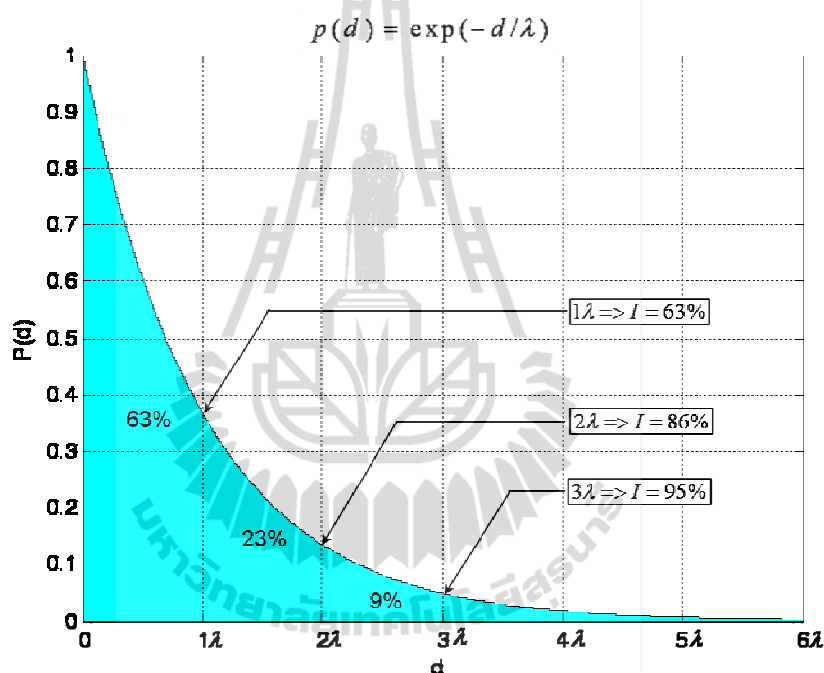


Figure 2.13 The probability for an electron to escape from a solid without inelastic energy loss as a function of the depth (Tougaard and Mohai, 1988).

The IMFP may be used to calculate the thickness of surface films, for example as shown in the Figure 2.14, where material, B is a substrate and it is covered by a thin film of a different material, A. The intensity of XPS signal from underlying of substrate is reduced due to inelastic scattering process of photoelectrons, occurring when they pass through the layer of material A. If the probability of a single photoelectron passing through the over-lying layer is given by $P(d) = \exp(-d/\lambda)$

(the same as the equation 2.7), where d is the thickness of the over-lying layer A. If I_0 is the intensity of signal from substrate without any covering layer, the intensity I the signals with the over-layer can be found from the following relation

$$I = I_0 \exp(-t/\lambda) \quad (2.8)$$

Equation (2.8) can be used to estimate the thickness of a thin over-lying layer if λ is known. It is noted that the accuracy of the final quantitative result for the composition of the surface atom layer depends essentially on the accuracy of IMFP.

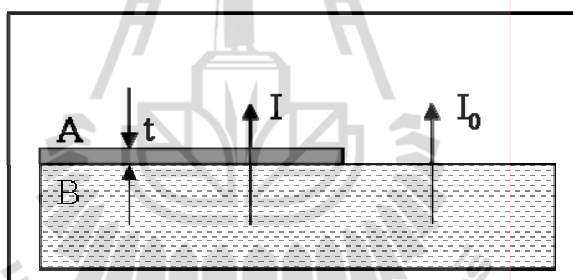


Figure 2.14 The schematic diagram showing the parameters used for considering the probability of any single photoelectron passing through a thin layer.

2.4 Electron energy analyzers

PES experiments require sufficiently good vacuum conditions. Normally, the base pressure of the PES must be 1×10^{-9} Torr or lower. For demanding experiments, vacuum in the range of 5×10^{-11} Torr is necessary. The advantage of using synchrotron light is that the vacuum pressure in the PES does not rise as there is no heat source like an electron filament in X-ray tubes. Thus, PES can be performed at the base pressure of the system. This is essential for the investigation of surfaces of

materials that degrade rapidly by residual gases in the system. PES experimental set up is shown in the Figure 2.2. In laboratory set up, a PES system has one or two light sources such as a UV and an X-ray source. The laboratory photon sources can be replaced by a synchrotron radiation source.

The electron energy analyzers in PES systems exist in different types. There are, in principle, four methods to analyze the energy of a charged particle. Those are the followings.

- 1) the use of resonances in a scattering process,
- 2) the time-of-flight method,
- 3) the deceleration of the particles by a retarding electric field, and
- 4) the change of the orbit of a particle by an electric or magnetic fields.

The last two methods are best suited for PES. The most common type used for PES experiments are electrostatic electron energy analyzers, which exist in various configurations. Those are the plane mirror analyzer (PMA), cylindrical mirror analyzer (CMA), cylindrical deflection analyzer (CDA), and the concentric hemispherical analyzer (CHA). CHA is the most commonly used as an electron energy analyzer. Brief descriptions of different configurations of electrostatic electron energy analyzer are given below.

2.4.1 Plane mirror analyzer (PMA)

PMA, or a parallel plate mirror analyzer, is the simplest configuration of an electrostatic analyzer. The analyzer is composed of two parallel plates with a distance d and potential difference V . Electrons enter the analyzer at the entrance slit. Only electrons with proper kinetic energy can travel pass thru the exit slit. The trajectories

of electrons from the entrance to exit slits are parabolic. The entering and the exiting angles for this type of analyzer are 45 degrees as illustrated schematic diagram of PMS in Figure 2.15. In order for transmission to occur, the potential difference between the two plates is given by;

$$V = E_0 d / eL_0 \quad (2.9)$$

where, E_0 is kinetic energy of electron (eV), e is charge of the electron.

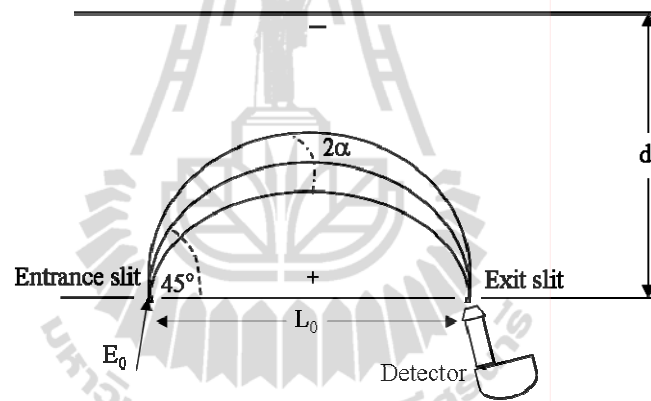


Figure 2.15 The schematic diagram of PMA.

2.4.2 Cylindrical mirror analyzer (CMA)

CMA is more advanced than PMA. It consists of two cylinders and the potential difference between cylinders is V . The entrance and exit slits are on the inner cylinder. The angle between the center of the cylinders and the electrons is 42.3 degrees. The trajectories of electrons can be shifted either up or down more parabolic than the elliptical shape, as shown in Figure 2.16. The relation between the potential difference and the kinetic energy of an electron is given by the following equation;

$$V = 1.3E_0 \ln(R_{out} / R_{in}) \quad (2.10)$$

where, $L_0 = 6.1(R_{in})$, and E_0 is in volts. R_{in} and R_{out} are the radii of the inner and outer cylinders, respectively. CMA is good for experiment that does not require high resolution such as AES.

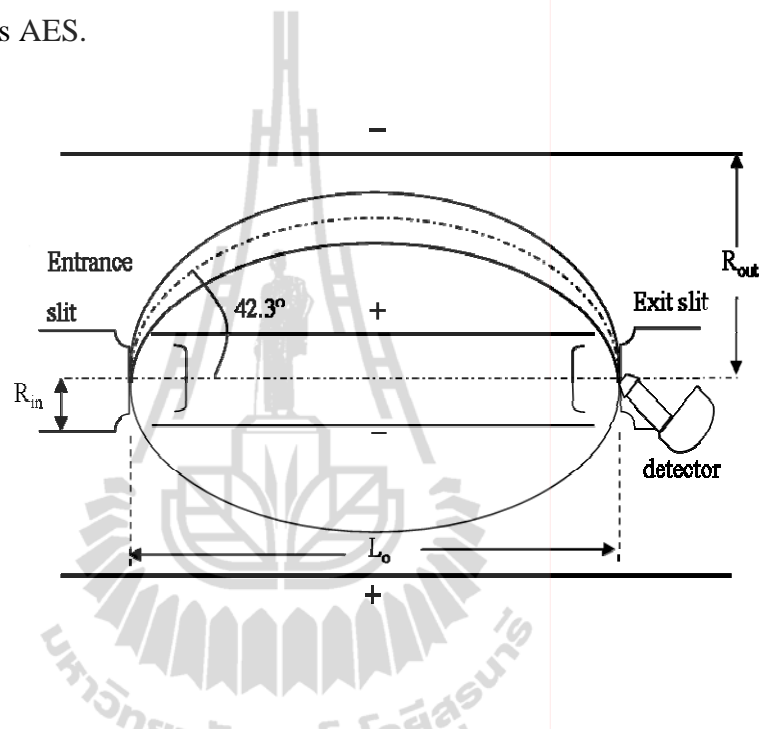


Figure 2.16 Schematic diagram of a CMA.

2.4.3 Cylindrical deflection analyzer (CDA)

CDA consists of two cylinders. The electrons travel in the analyzer with 127-degree deflection. Thus, this type of analyzer is sometime called “127-degree analyzer”. The potential difference in a CDA is given by

$$2V = E_0 (R_{in} / R_{out}) \quad (2.11)$$

where, E_0 is the energy of incoming photoelectrons (eV). CDA is excellent for high resolution application, however, the transition of this analyzer is rather low. The schematic diagram of CDA is shown in the Figure 2.17.

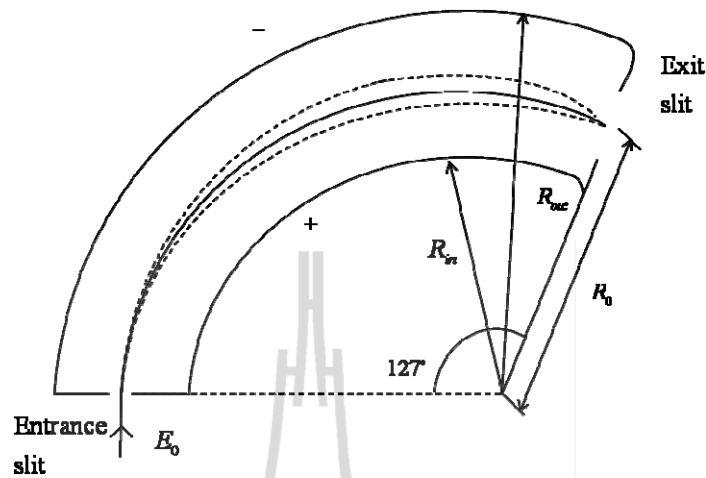


Figure 2.17 Schematic diagram of a CDA showing the angle the cylinder span of 127 degrees.

2.4.4 Concentric hemispherical analyzer (CHA)

CHA, or hemispherical deflection analyzer, is used in most PES system nowadays. The basic diagram of a CHA is shown in Figure 2.18. CHA consists of two concentric hemispheres of radii R_1 and R_2 for the inner and outer hemispheres, respectively. Both inner and outer hemispheres are applied with potentials $-V_1$ and $-V_2$, respectively. It is noted that V_1 is less than V_2 . Electrons entering the entrance slit will make a curved motion and pass thru the exit slit if the kinetic energy is proper. This kinetic energy is called pass energy. Electrons with higher kinetic energy will hit the outer hemisphere while electrons with lower kinetic energy will hit the inner hemisphere. Thus only electrons in a narrow energy region can pass through the exit slit and be detected by a detector. Typical energy of electron can be detect by a CHA is in the range of 0-2500 eV for electrons.

The radius R_0 in the Figure 2.18 is the median equipotential surface between inner and outer hemispheres. The collinear points with the centre of curvature are the

source S and focus F . The potential V_0 along the median line of hemispheres is given by

$$V_0 = \frac{V_1 R_1 + V_2 R_2}{2R_0} \quad (2.12)$$

If electrons of energy $E = eV_0$ enter the analyzer tangentially to the median surface of the radius R_0 , the potential of V_1 and V_2 and circular orbits of radius R_0 are described by the following equation;

$$V_1 = V_0 \left[3 - 2 \left(\frac{R_0}{R_1} \right) \right] \quad (2.13)$$

and

$$V_2 = V_0 \left[3 - 2 \left(\frac{R_0}{R_2} \right) \right] \quad (2.14)$$

From which

$$V_2 - V_1 = V_0 \left(\frac{R_2}{R_1} - \frac{R_1}{R_2} \right) \quad (2.15)$$

or

$$e\Delta V = E \left(\frac{R_2}{R_1} - \frac{R_1}{R_2} \right) \quad (2.16)$$

Equation (2.16) can be re-written in the form, $E = ke\Delta V$, where k is the spectrometer constant.

Electrons of the correct energy E are injected tangentially at the source S . Then they are focused at F , for the complete hemisphere of radius R_0 . Electrons are injected into analyzer at an angle $\delta\alpha$ to the correct tangential direction and energy

ΔE must be the difference from the correct energy E . Thus, the shift of ΔR along the radius of R_0 from the correct focal position, which is given by;

$$\Delta R = 2R_0 \left[\frac{\Delta E}{E} - (\delta\alpha)^2 \right] \quad (2.17)$$

For the base resolution is given by;

$$\frac{\Delta E_b}{E} = \frac{W_1 + W_2}{2R_0} + (\delta\alpha)^2 \quad (2.18)$$

where, W_1 and W_2 are the width of the entrance and exit slits respectively. Note that, the energy resolution of the CHA will depend on the square of the angular spread, in term of $(\delta\alpha)^2$.

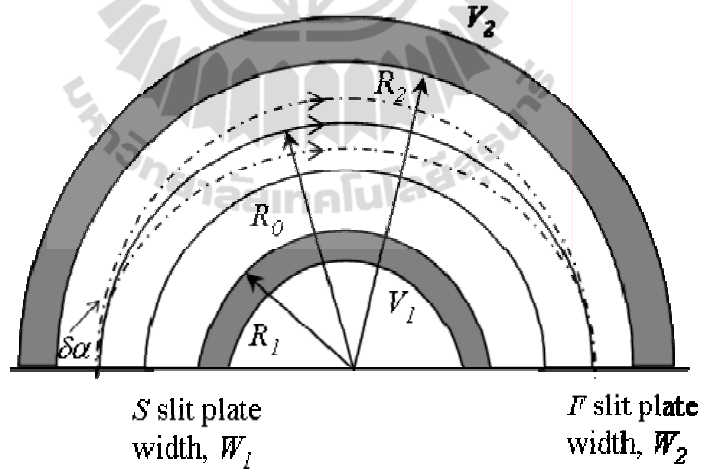


Figure 2.18 Schematic cross-section of a concentric hemispherical analyzer (CHA).

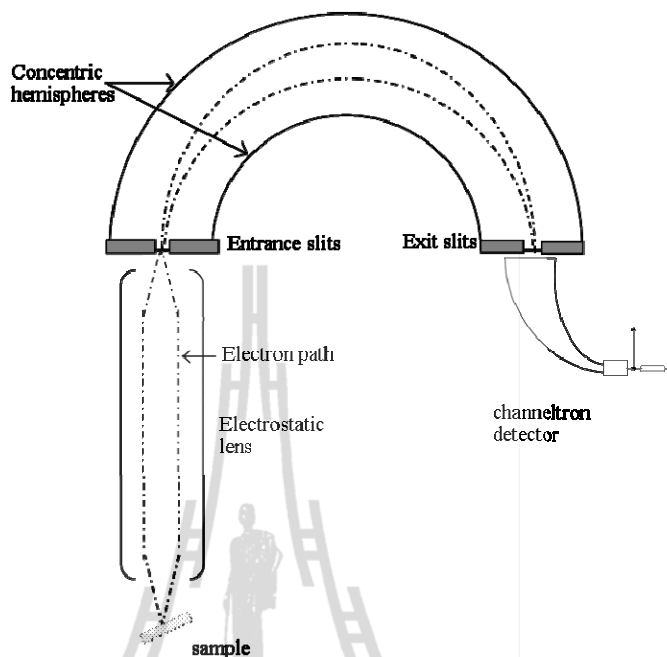


Figure 2.19 A hemispherical electron energy analyzer consists of three main parts, i.e., a series of lens, an analyzer and the detector.

Figure 2.19 shows a series of lenses placed before the CHA. CHA is designed to operate in two energy analyzing modes, Constant Retard Ratio (CRR) and Constant Analysis Energy (CAE). In CRR mode, the energy of all the electrons is reduced by a constant ratio. It means that if electrons with an energy of 1000 eV are to be detected and the retard ratio is 10, then the energy of the electrons is slowed down to 100 eV and the pass energy is set to 100 eV. For the CAE mode, the pass energy is constant, for example if the pass energy is 50 eV and the electrons with energy of 1000 eV are detected. Then the energy of the electrons is reduced by 950 eV. When using the CRR mode gives constant resolving power, which resolving power of these is proportional to the inner and outer hemispheres. The CAE mode provides a constant energy resolution across the energy range of electron energies and is used for XPS.

2.5 Synchrotron radiation

Synchrotron radiation is electromagnetic wave emitted when a relativistic charged particle is in a curved motion. The particle may be electron, positron, proton or any ions. The most common particle used in synchrotron light sources is an electron. There are three different kinds of device in synchrotron light source that used for generating synchrotron radiation. The three devices are electro-/permanent magnetic devices since the curved motion of charged particles can be achieved by the Lorentz force. These devices are a bending magnet, wavelength shifter/wiggler and undulator. Brief descriptions of the devices and their radiation are given below.

2.5.1 Bending magnet radiation

Bending magnets are used to define the storage ring of synchrotron light sources. Ideally, synchrotron radiation from a bending magnet is emitted by an electron circulating in any point along the curved path. It appears that the radiation move around the storage ring as shown in the Figure 2.20. It shows that, in the vertical non deflecting plane there is no focusing. The radiation is very much collimated with an opening angle of $1/\gamma$ (Widemann), typically 0.1 to 1 milliradian (mrad), where γ is the particle energy in units of its rest mass.

Electrons circulating in the storage ring are constrained to move into the equidistant bunches. The distance between two bunches is equal to integer multiple, usually is equal to unity, of the RF-wavelength (60 cm for 500 MHz) while the length of each bunch is 1 to 3 cm or 30 to 100 picosecond (ps), this parameter is depending on beam energy and RF-voltage.

The radiation emitted from a bending magnet is a broad spectrum, in principle, from microwaves up to the critical photon energy. Because the bending magnets define the geometry of the storage ring, it cannot be freely choose the field strength and, thus, the critical photon energy is fixed.

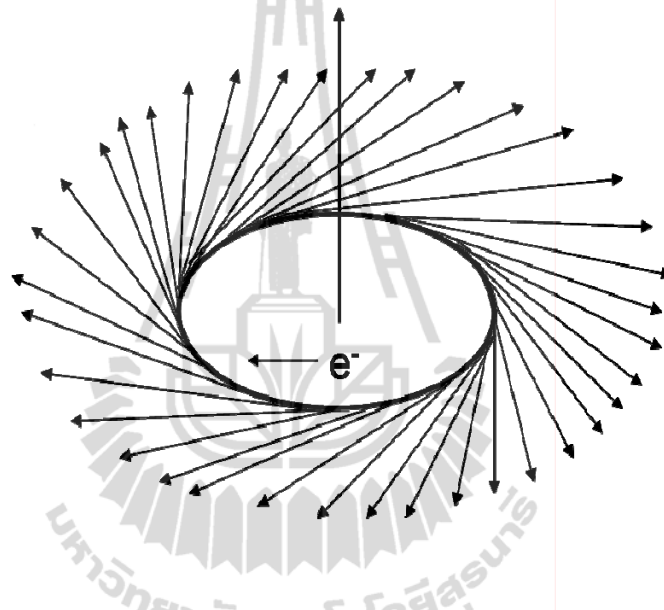


Figure 2.20 Radiation emitted from the bending magnets.

2.5.2 Wavelength shifter and wiggler

The wiggler is an insertion device used for producing harder x-ray radiation in a low energy storage ring. The simplest wiggler magnet is called the wavelength shifter. Wavelength shifter may consist of three or five superconducting dipole magnets, with alternatively magnetic field directions. The limitation to three or five poles is dependent on the technical and may be superconducting magnet and cryogenic-technology progresses. A three pole wavelength shifter shows schematically in the Figure 2.21.

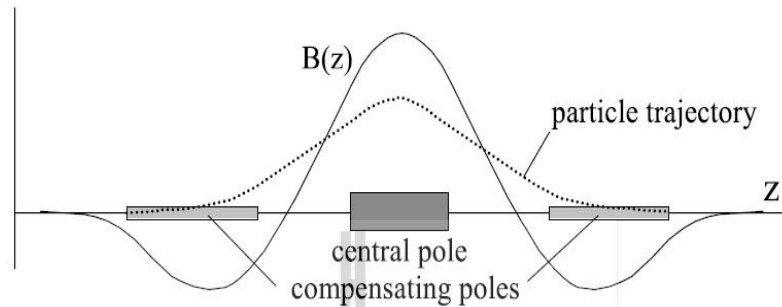


Figure 2.21 The distribution of magnetic field along the beam for a wavelength shifter.

When the electron beam traverses the wavelength shifter, it is deflected up and down or right and left, so that there is no net deflection. Thus, the longitudinal field distribution in the horizontal plane deflecting wavelength shifter must meet the condition.

$$\int_{-\infty}^{\infty} B_y(y=0, z) dz = 0 \quad (2.19)$$

It is clear that only the central pole high field is used as the radiation source, while both side of the pole is used to compensate the beam deflection from the central pole of wavelength shifter. Usually, the end poles are longer than the central poles and can operate at a lower field. The enhancement of radiation can be obtained by increasing the number of pole.

2.5.3 Wiggler magnet radiation

The simplest wiggler magnet is called the wavelength shifter, which generates one oscillation of the electron beam. The total electron bending angle is large than the opening angle of the radiation ($\leq 0.05^\circ$). Generally, the center pole of wiggler magnet

magnet is operated at a field higher than the bending magnets of the ring, and can expand the proton spectrum at high energies. The spectral distribution is a smooth continuum that is similar to the bending magnets as shown in the Figure 2.22. But the intensity is higher than the bending magnets due to the contribution of many magnet dipoles in the wiggler.

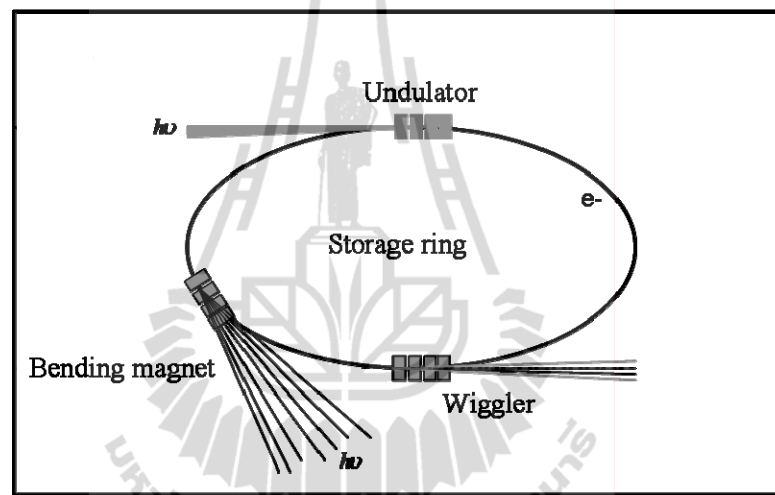


Figure 2.22 Schematic diagram showing the beam divergence of radiation from a bending magnet, a wiggler and an undulator in a storage ring.

The spectrum of wiggler radiation is characterized by the critical energy. The critical energy from wigglers and bending magnets is given by;

$$\varepsilon_c = \frac{3hc\gamma^3}{2\rho} = 0.06651BE^2 \quad (2.20)$$

where, B is the magnetic field of wiggler or bending magnet in kG, ρ is the radius of curvature, the critical energy is in units of keV, the beam energy is in units of GeV. The wiggler can extend the spectrum to higher photon energies, which is dependent

on the ratio of the wiggler field to bending magnet field. The number of magnet poles was used to increase the photon flux and to enhance the wiggler radiation. The radiation is a well collimated beam with beam divergence of a few mrad.

2.5.4 Undulator radiation

Synchrotron radiation generated by undulator is different from the radiation generated by bending magnets and wigglers. Fundamentally, an undulator consists of a periodic structure of dipole magnets. The length of the undulator with a wavelength λ_p is alternated by the static magnetic field. Electrons traverse the periodic magnet structure under forced oscillations. And thus the electron emits radiation at the wavelength of its periodic motion in the undulator. The radiation generated by undulator is intense and is concentrated in narrow ranges of the spectrum. Also, it is collimated in the plane of the electron orbit. Thereby the radiation is introduced through the synchrotron beamline for experiments. It is given by;

$$K = \frac{eB\lambda_p}{2\pi m_e c} \quad (2.21)$$

where, e is the particle charge, B is the magnetic field, λ_p is the wavelength, m_e is the electron rest mass, and c is the speed of light. This equation is determined the nature of the electron motion. If, $K \ll 1$, the radiation produced, which lead to narrow energy in the spectrum due to the amplitude of oscillation is small. While, if $K \geq 1$, the amplitude of oscillation is bigger and radiation contribution from each field period summation independently, and their energy lead to a broad spectrum of energy. Radiation in this regime is called “wiggler”, it’s no longer undulator. Undulators can

give several orders of magnitude higher flux than the bending magnet and in high requirement at synchrotron radiation facilities.

At the Siam Photon Laboratory of the Synchrotron Light Research Institute (Public Organization) the light source is the U60 undulator and the bending magnet. They are used to produce synchrotron radiation. The radiation is produced from the U60 undulator is almost 4 orders of magnitude higher than produced from the bending magnet. The light spectra is produced by U60 undulator it cover all K-edge of important light elements such as C, N, and O. L-edge of important metals starting from light element Na up to 3d transition metal Ni. The U60 can produce the most valuable light which will be used in many different areas of research and covers several measurement techniques. The techniques are using synchrotron light (from U60) to study such as angle resolved photoemission spectroscopy (ARPES), X-ray photoelectron spectroscopy (XPS), X-ray absorption spectroscopy (XAS), and photoemission electron microscopy (PEEM).

Figure 2.23 shows the calculated photon flux density of synchrotron radiation generated from the Siam Photon Source as a function of photon energy.

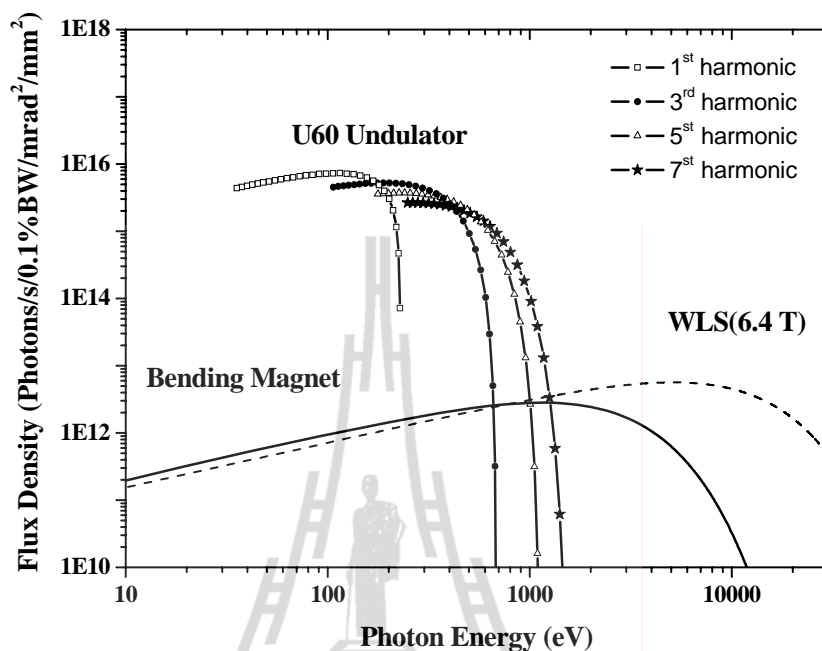


Figure 2.23 The calculated flux density as a function of photon energy of radiation generated by a U60 planar undulator, the bending magnet and wavelength shifter at the Siam Photon Source (Songsiriritthigul *et al.*, 2007).

2.6 Background subtraction

It is well known that PES is a direct technique to obtain the valence band density of states (DOS) of materials, which provides the information about the properties of materials. In photoemission experiments, valence electrons are ejected from the specimen by excitation photons. Large part of valence band DOS contains the background resulting from either elastic or inelastic scattering of the electrons in the specimen. The intrinsic nature of the asymmetric background step associated with most peaks in the photoelectron spectrum, while extrinsic or the secondary electrons effects can be found in the spectrum. The secondary electrons are the electrons that loss their kinetic energy during the transport to the exposed surface by the inelastic

scattering. This the background need to removed. In this work, the secondary electrons background of the spectra was subtracted using Shirley type background (Shirley, 1972). The Shirley type background is easily determined from the experimental data as the integral of the peak. Background subtraction method requires an iterative approach which can be performed by a computer programming. The algorithm can be expressed as following.

The Shirley background intensity $B(\varepsilon)$, where ε is kinetic energy, within photoemission spectra is define as the integrated intensity of the inelastic scattering electrons at lower kinetic energy. With this condition, the background matches the measured spectrum outside the region of the peak which is given by.

$$B(\varepsilon) \equiv A \int_{\varepsilon}^{\infty} P(\varepsilon') d\varepsilon' = A \int_{\varepsilon}^{\infty} [M(\varepsilon') - B(\varepsilon')] d\varepsilon' \quad (2.22)$$

where, P is intrinsic spectrum intensity, M is the measured intensity, and A is a constant of the inelastic scattering yield. The parameters for the calculation are defined in the Figure 2.24. The measured intensity in a photoemission spectrum is given by M_i , where $i=1$ at its lowest points the kinetic energy, and $i=N$ at its highest points the kinetic energy. The background value at the start point are given by

$$B_N = B_{N-1} = M_N \quad (2.23)$$

The first guess of A is given by

$$A^{(0)} = 0.002 \quad (2.24)$$

For the trial of background is $B_i^{(0)}$, which are calculated one by one from high kinetic energy to lower kinetic energy by using the first guess of $A^{(0)}$, which is given by;

$$B_i^{(0)} = B_N + A^{(0)} \sum_{j=i+1}^N (M_j - B_j^{(0)}) \quad (2.25)$$

And, if $A^{(1)}$ is the next iteration, it can found from the following relation;

$$A^{(1)} = A^{(0)} \left(1 + \frac{M_1 - B_1^{(0)}}{M_1} \right) \quad (2.26)$$

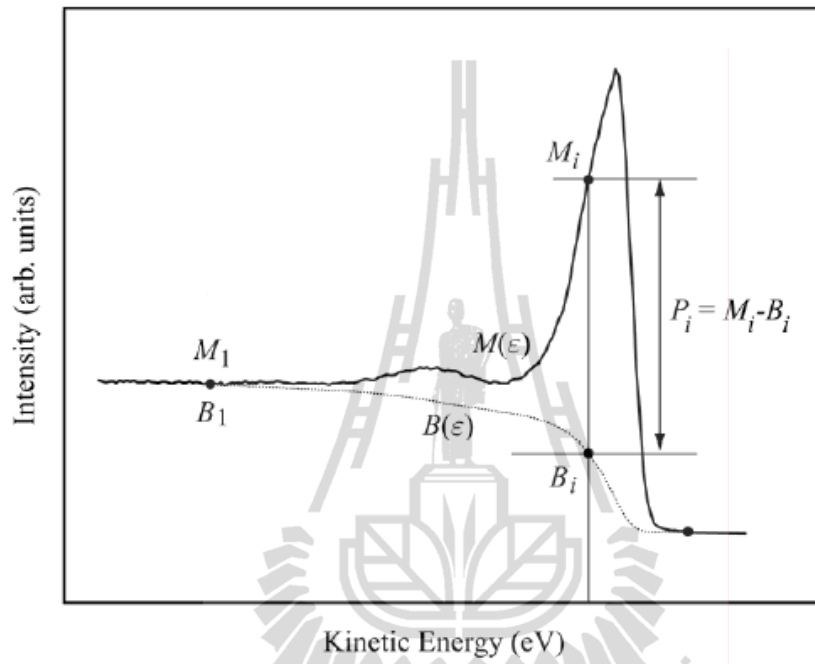


Figure 2.24 The schematic showing the components of the parameters used in the calculation of the Shirley's type background.

CHAPTER III

INSTRUMENTATIONS AND METHODS

This chapter provides principle and descriptions of the instrumentations and experimental methods employed in the thesis work. The experiments were carried out using the old photoemission beamline BL4 and the new photoemission beamline BL3.2a at the Synchrotron Light Research Institute (SLRI). The photoemission experimental station of BL4 was relocated and connected to BL3.2a with minor modifications. The main advantage for the new beamline is the high brilliant light from the planar undulator, comparing to bending magnet radiation. Major beamline subsystems/components and equipments installed at the experimental stations are described below.

3.1 Beamline

The BL3.2 beamline at SLRI was constructed using most of mechanical component of the old BL4 beamline. The optical layout of BL3.2 was newly designed. The specifications of the mirror and gratings are different from those of BL4. BL3.2 was designed to cover wider energy range. The source for BL3.2 is the planar undulator while the source for the old BL4 was bending magnet. Only the optical layout of the current beamline will be explained below.

The photo of BL3.2 is shown in Figure 3.1. This beamline was designed for both chemical analysis and investigations of electronic structures of solids and solid

surfaces. The beamline has two branches downstream the monochromator, i.e., BL3.2a and BL3.2b. The two branchlines are operated in a time sharing mode. BL3.2b is dedicated for LEEM-PEEM (low-energy electron microscopy-photoemission electron microscopy). BL3.2a is designed primarily for ARPES (angle-resolved photoemission spectroscopy) and AIPES (angle-integrated photoemission spectroscopy). In addition, X-ray absorption spectroscopy (XAS) for light elements may also be performed at BL3.2 in the total and partial electron yield modes. Moreover, with the imaging capability of the LEEM-PEEM system, imaging XPS (X-ray photoelectron spectroscopy) and imaging XAS experiments are also possible to be carried out at BL3.2b.



Figure 3.1 The photo BL3.2 at the Siam Photon Laboratory.

The optical layout of the BL3.2 is shown in the Figure 3.2. The optical beamline may be divided into three main parts, i.e., a pre-focusing system, a monochromator, and two post-focusing systems (Songsirithigul *et al.*, 2007).

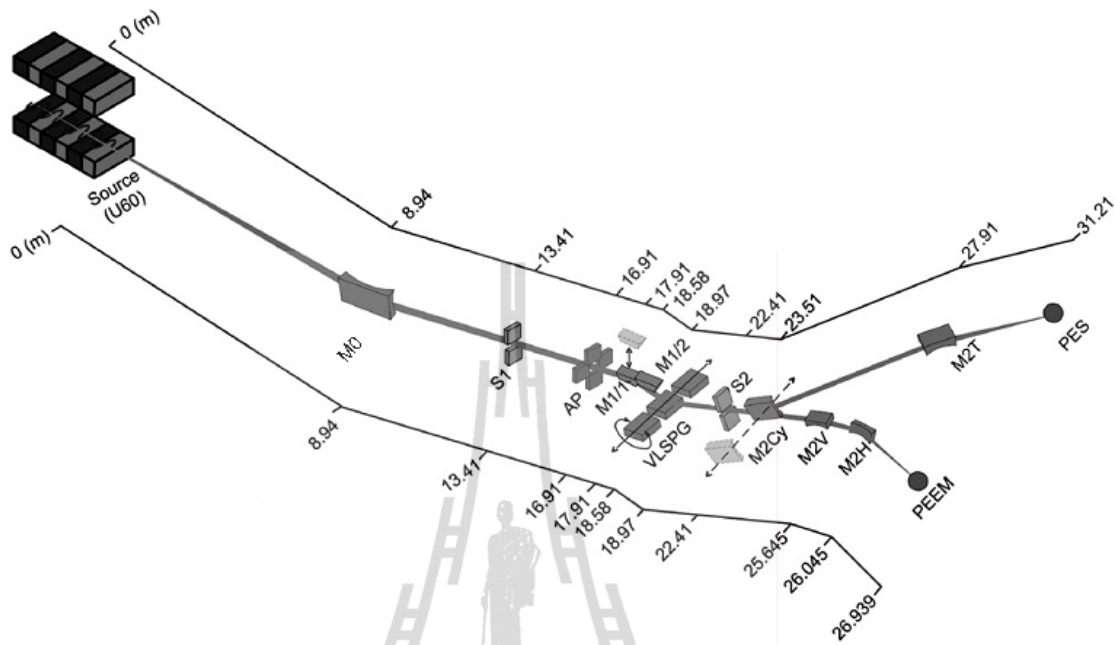


Figure 3.2 The Optical layout of BL3.2 at the Siam Photon Laboratory.

A toroidal mirror (M0) is used as an optical element to deflect the light beam 6° horizontally and sagittally focus the source into an entrance slit (S1) of the monochromator. The demagnification of M0 in the vertical direction is 2, i.e., the beam size in the vertical direction at the entrance slit is expected to be 2 times smaller than that at the source position. (Songsiriritthigul *et al.*, 2007).

The monochromator used in this beamline is a varied line-spacing plane grating (VLSPG) monochromator. It was designed to cover a wide range of photon energy with three gratings and two fixed included angle, i.e., 167.5° and 172.5° . The monochromator consists of an entrance slit (S1), two focusing spherical mirrors (M1/1 and M1/2), an aperture, three exchangeable VLSPGs and an exit slit (S2). M1/1 and M1/2 are exchangeable, allowing the included angle to be selected for low and high photon energy ranges. The three gratings have different line density at the

center of the grating (N_0), i.e., 600, 1200, and 2400 lines/mm. The grating with N_0 of 600 lines/mm is used for the energy ranges of 40-160 eV. The gratings with N_0 of 1200 and 2400 lines/mm are used for the energy ranges of 220-1040 eV. The low energy and high energy ranges can be selected by selecting between the spherical mirror M1/1 and M1/2. For the photon energy ranges of 40-160 eV, M1/1 moves upward, allowing the beam pass through the second focusing spherical mirror which is M1/2, as illustrated in Figure 3.3.

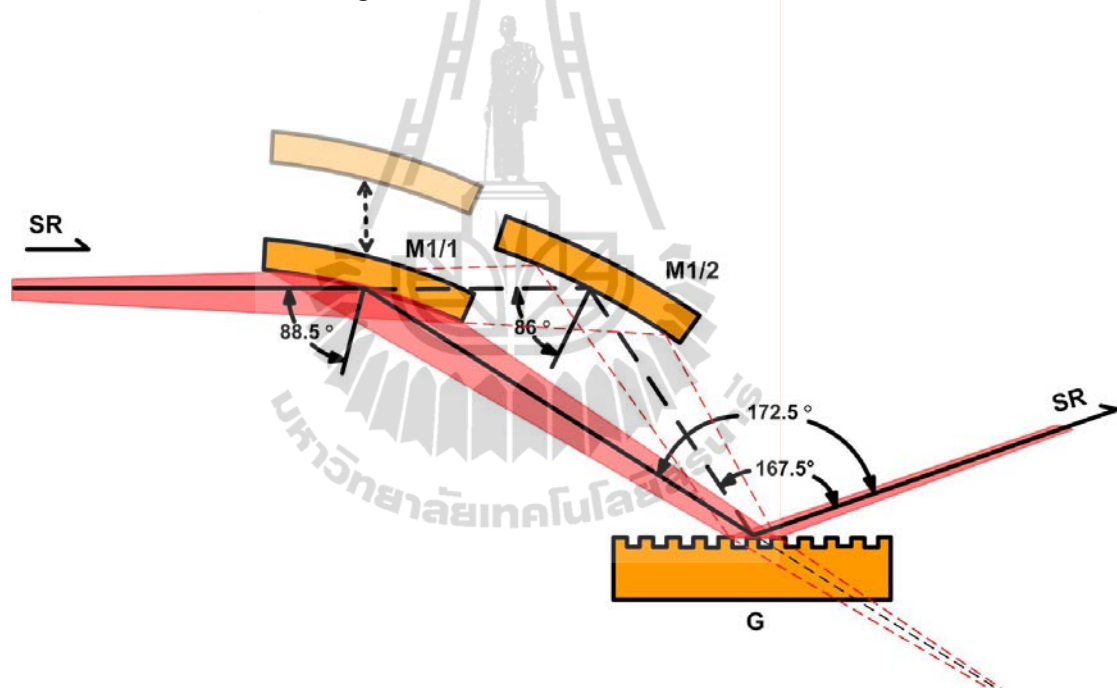


Figure 3.3 The schematic diagram showing the included angles of the monochromator of BL3.2 at the Siam Photon Laboratory.

The advantage of this type of a monochromator is that scanning of photon energy can simply be done by rotating the grating as show in the Figure 3.4. For the whole photon energy range the monochromatic light beam is focused at the position of the exit slit, S2, it means that, no movement of the exit slit is necessary when photon energy is changed.

After light is monochromatized, a cylindrical mirror M2Cy can be used to deflect the beam horizontally to branchline BL3.2a for photoemission experimental station. Without M2Cy on the optical axis, the monochromatized beam will be focused by a K-B mirror system onto a sample position of the LEEM-PEEM.

Photon energy scanning mechanism

The monochromator of BL3.2 was designed to cover a wide photon energy range. To scan photon energy, the grating of the monochromator is rotated. The rotation is simply done by a sine bar driven by a stepping motor. The rotation of the stepping motor is controlled by the home-developed software using LabView program. Thus, only a linear movement driven by a step motor is required for photon energy scanning. To assure the reproducibility alignment of the scanning mechanism, a linear encoder is necessary. Thus, the high precision ND281B Heidenhain linear encoder is used for accurate positioning. The accuracy of the encoder is 0.01 micron. The three gratings are installed on a rotation table. The exchange or adjustment of the grating is done by a linear translation of the table driven by a manual linear drive as shown in the Figure 3.4. This figure shows the external of the grating chamber and the sine bar, which is located inside the UHV chamber and is connected to the step motor via the bellow.

The relation between the constant included angle, light wavelength, and the angle of rotation for the monochromator is given by

$$Nk\lambda = 2 \sin \phi \cos \theta, \quad (3.1)$$

where, $2\theta = \alpha - \beta$ is the included angle, $2\phi = \alpha + \beta$ is the rotating angle with respect to the normal of plane of the grating surface. The included angles for the

monochromator of BL3.2 are 167.5° and 172.5° for the low energy and high energy ranges, respectively. For the zero-order light, θ is the angle of incidence and the angle of reflection, which are 83.75° and 86.25° for the low and high energy ranges, respectively. A linear translation of the motion drive for the sine bar and the angle of rotation of the grating can be found from the following relation.

$$R = L \sin \phi, \quad (3.2)$$

where, R is the linear displacement, L is the length of the sine bar. By substituting equation (3.2) into the equation (3.1), the relationship between the linear motion and the rotating angle can be written as follow.

$$\lambda = \left(\frac{2 \cos \theta R}{NkL} \right), \quad (3.3)$$

where, k is the diffraction order. Since $\lambda = hc / E$ (E is the photon energy (eV), h is the plank's constant, c is the speed of the light), the relationship between the linear displacement and the photon energy can be given by

$$E = \frac{1}{R} \times \left(\frac{hcNLk}{2 \cos \theta} \right), \quad (3.4)$$

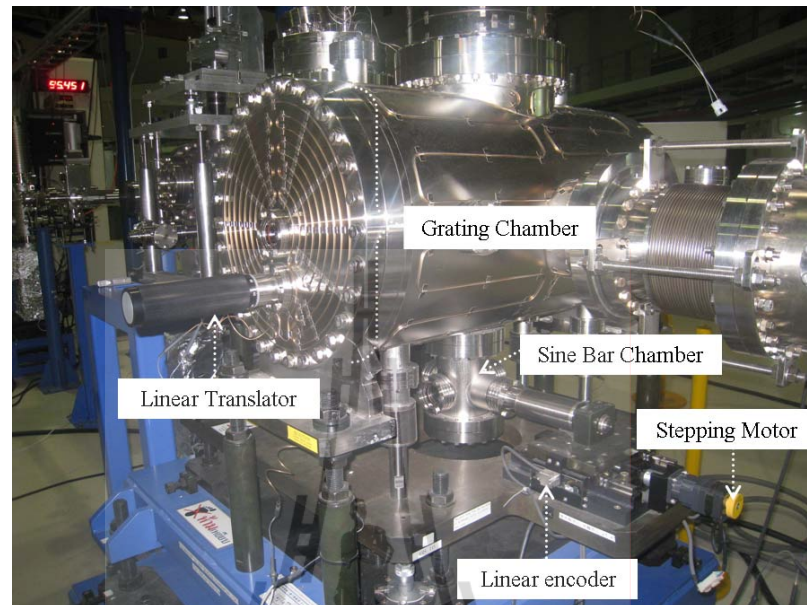


Figure 3.4 The photo of the grating chamber.

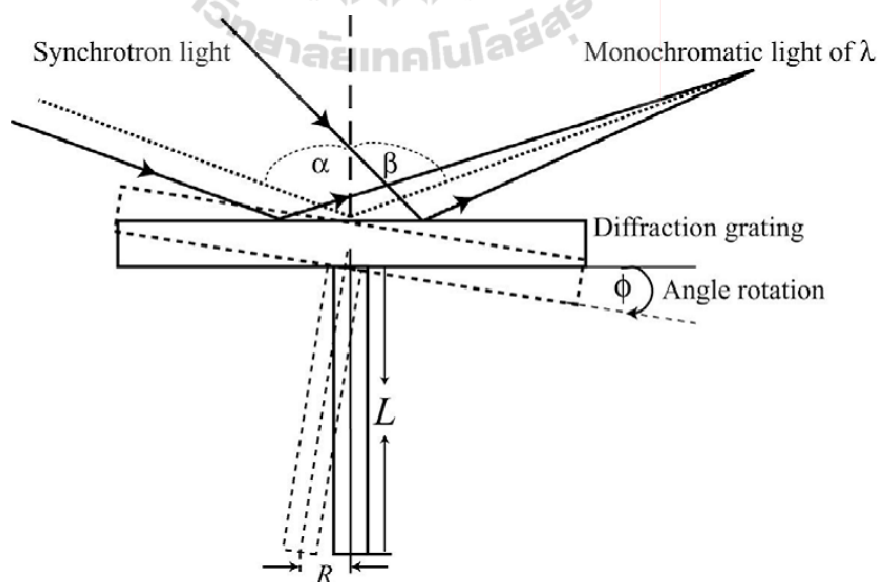


Figure 3.5 Schematic diagram of the sine bar for the rotation of the gratings to scan photon energy at BL3.

3.2 Photoemission spectroscopy (PES) beamlines

Photoemission experiments carried out during the course of this work employed two beamlines at SLRI, i.e., BL4 and BL3.2a. The experimental station was originally connected to BL4 before the beamline was dismantled. The same experimental station was relocated and connected to BL3.2a with some minor modifications. More than half of this thesis work was carried out at BL3.2a using radiation from the first undulator of SLRI.

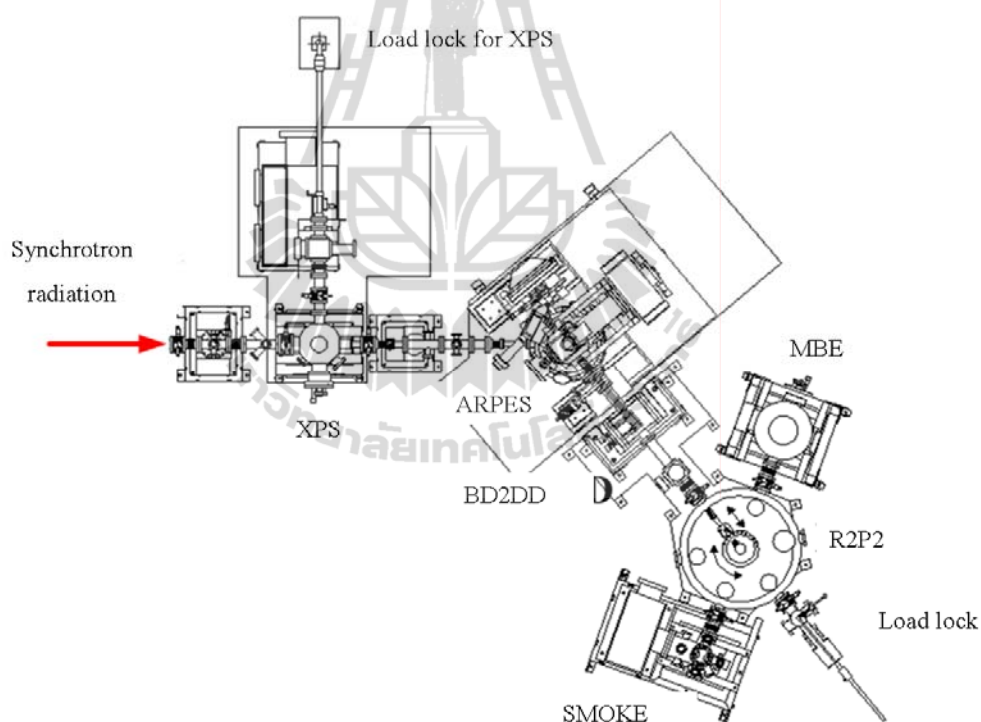


Figure 3.6 Show the top-view layout of the photoemission experimental station connected to BL3.2a to utilize undulator radiation.

Figure 3.6 shows the top-view layout of the experimental station of BL3.2a. The station may be divided into four main ultra high vacuum (UHV) systems. The first one is located at the most upstream, which is an X-ray photo spectroscopy (XPS)

system. This XPS system is equipped with a Thermo VG Scientific CLAM2 electron energy analyzer. Downstream of the XPS system is an angle-resolved photoemission spectroscopy (ARPES) system. This ARPES is connected to the metal molecular beam epitaxy (MBE) and surface magneto-optic Kerr effect (SMOKE) systems via a UHV sample transport system. Only XPS and ARPES systems are used in this thesis work, and thus the description of the systems will be summarized below.

3.2.1 The ARPES system

The ARPES system consists of two main UHV chambers. Those are the analysis chamber and the sample preparation chamber. The schematic diagram of the ARPES system is shown in Figure 3.7. The two main chambers are vacuum-isolated by a gate valve. The preparation chamber is for surface cleaning by ion sputtering or by electron beam heating. This preparation chamber is equipped with an ion sputter gun. A long linear translation of manipulator is installed on top of preparation chamber allowing the sample to be either in the preparation chamber or in the analysis chamber by a linear translation of the manipulator. The analysis chamber is equipped with an electron gun for AES technique, a Thermo VG Alpha110 electron energy analyzer for AES and photoemission (UPS, XPS and ARPES) measurements. The base pressure in the analysis chamber is $\sim 1 \times 10^{-10}$ Torr, which is necessary for photoemission experiments. The ARPES system is evacuated by two ion pumps and two titanium sublimation pumps to obtain UHV the ultimate pressure in the preparation and analysis chambers. During ion sputter cleaning process, a turbomolecular is used for evacuation of the preparation chamber.

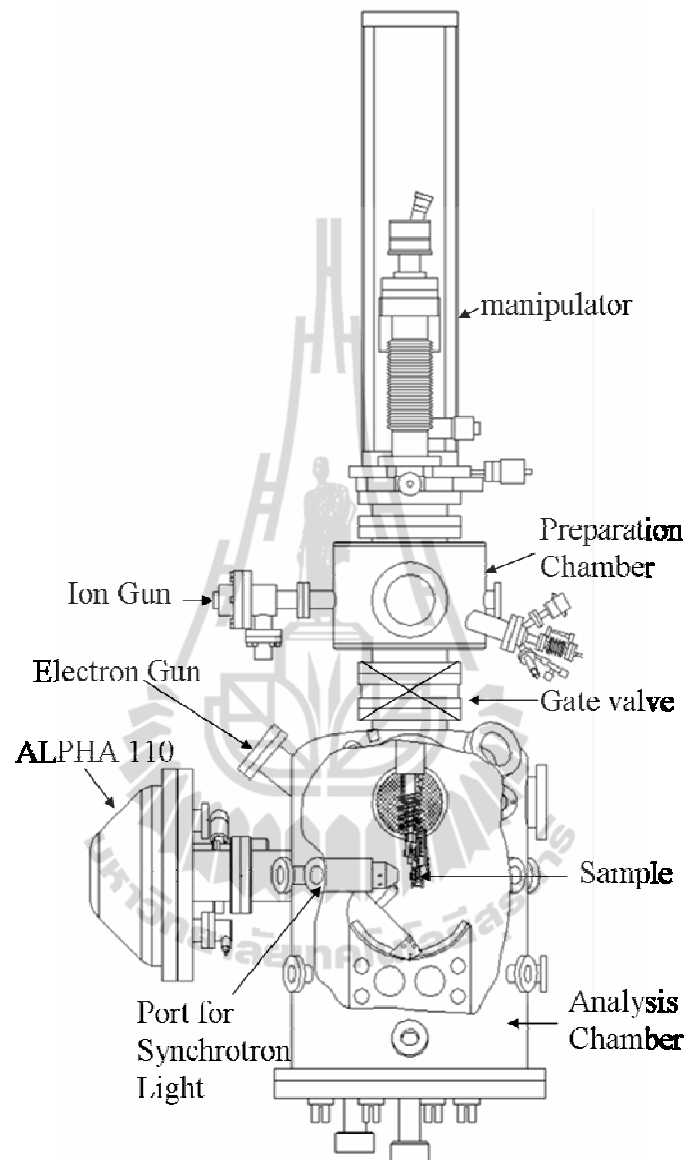


Figure 3.7 The schematic diagram of the ARPES system at BL3.2a.

Different excitation sources are available at the photoemission experimental station. Those are electron gun, UV discharged lamp, and synchrotron light source. Synchrotron light beam is designed to focus onto the sample of the ARPES system. The size of the light beam is less than 100 micron in a diameter.

3.2.2 The XPS system

The main equipment of the XPS system is an electron energy analyzer manufactured by the Thermo VG Scientific company. The system is also equipped with a sample load-lock system to prevent breaking of UHV condition during introduction of the sample into the analysis chamber. It is noted that the photon beam is not focused on the sample, and thus the beam size is rather large. The system is also equipped with an ion sputter gun for surface cleaning. Two needle valves for gas inlet allow the introduction of gases into the analysis chamber. One of the valves is for argon gas for surface cleaning by ion sputtering. The analysis chamber of the XPS is evacuated by an ion pump combined with a titanium sublimation pump. The base pressure of the analysis is $\sim 3 \times 10^{-10}$ Torr.

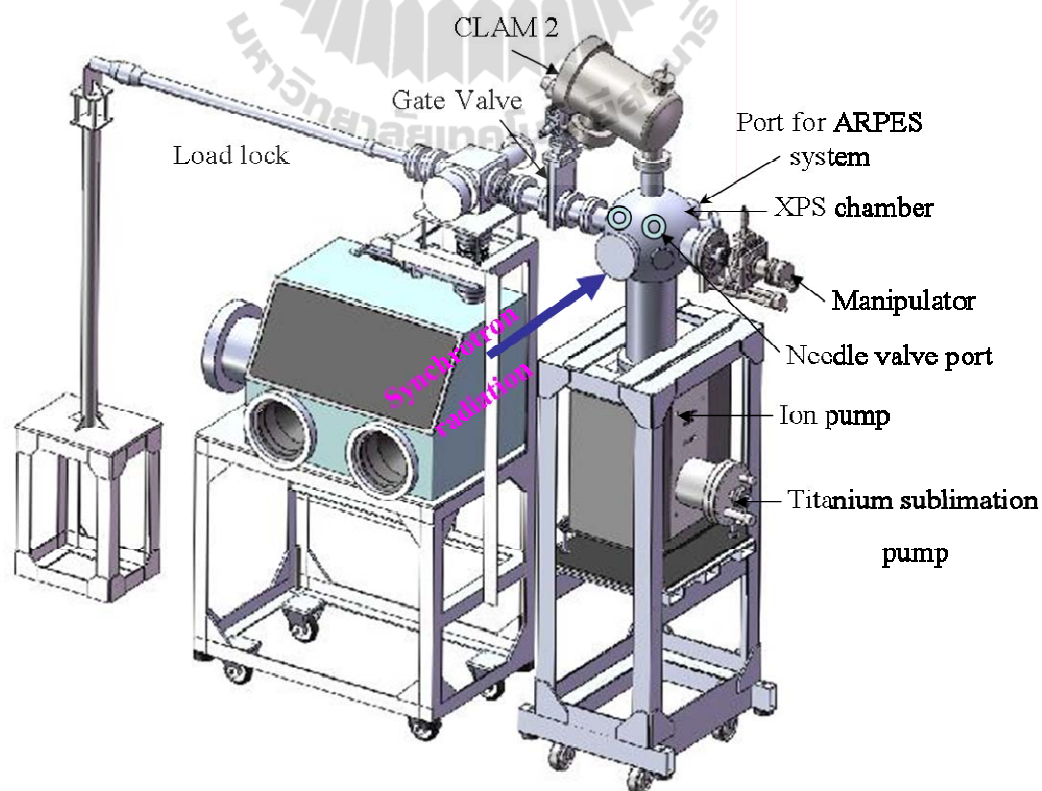


Figure 3.8 Schematic diagram of the XPS system at BL3.2a.

3.3 Sample preparation

The photoemission spectroscopy is a surface sensitive technique. It is well known that surface adsorption of foreign atoms or molecule alters the intrinsic nature of the surface regarding both atomic arrangement and the electronic structure. Thus is necessary that the surface must be atomically clean prior to photoemission measurements.

The samples used in this work are polycrystalline zinc foil supplied from the Nilaco Corporation. The purity of the polycrystalline zinc foil is 99.99%. The thickness of the foil is 0.05 mm. Zinc foils were cut into a size of about 5×5 mm. After that, zinc foil sample were cleaned in chemical solutions, before loading into the vacuum system. The reference sample used was a single crystal ZnO (0001).

To form ZnO by oxidation at elevated temperature in air, a zinc foil was cleaned by dipping in alcohol mixed with 10% bromine for a few seconds. After that the foil was cleaned in methanol in an ultrasonic bath for 10 minutes. Finally, the sample was subsequently washed several times by de-ionized water and dried by spraying nitrogen gas, respectively.

Zinc foils used for forming oxide layer by thermal oxidation in a UHV condition were cleaned in an ultrasonic bath in alcohol and in de-ionized water for 10 minutes, respectively. After that the samples were dried by purging of nitrogen gas. The final step before loading into the PES system is spot welding. Spot welding is a process in which contacting sample surfaces on to the sample holder, joined by the heat. The heat is obtained from resistance when electric current is passed through the sample. Figure 3.9, a) show clean Zn foil sheet while b), Zn foil was spot welded on the molybdenum sample holder.

Then the sample was introduced into the analysis chamber by a load lock system. The cleaning procedures in vacuum were performed by Ar^+ ion sputtering. The sample was sputtered by Ar^+ ions to remove surface contaminations, until the surface is perfectly clean. This thesis work, the cleaning surface was obtained by 0.5 keV Ar^+ ion sputtering in the UHV chamber.

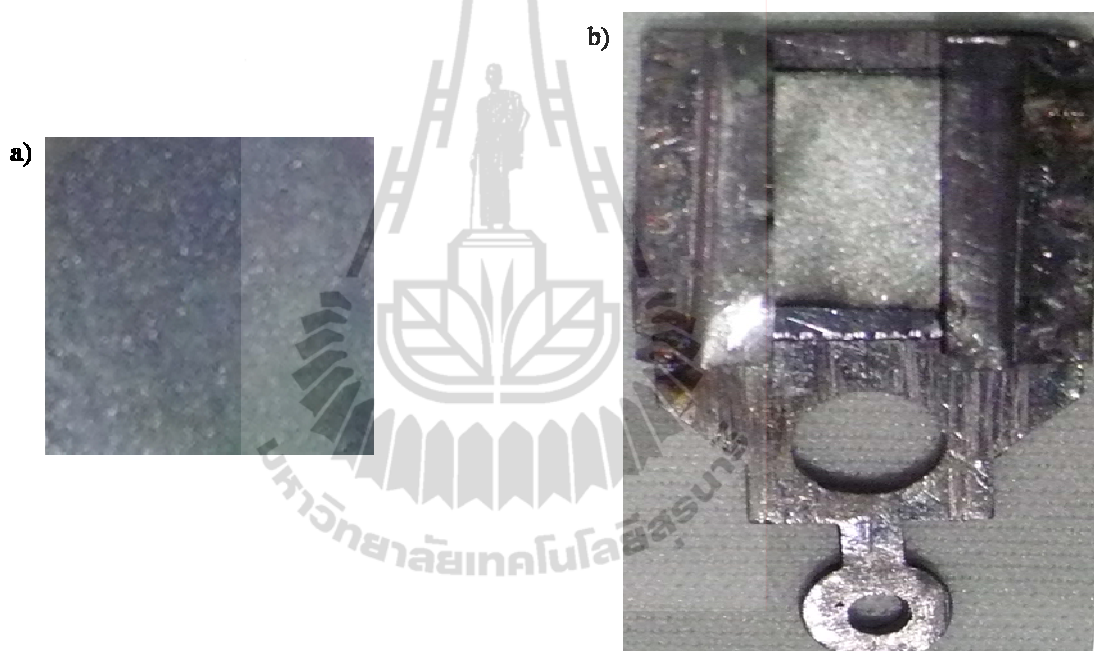


Figure 3.9 Show clean Zn foil sheet, a) and Zn foil was spot welded on the molybdenum sample holder, b).

Surface cleaning by ion sputtering

Although samples are chemically cleaned prior to the introduction into the vacuum system, it is unavoidable that the surface of the samples will be contaminated by adsorbed gas molecules. The common method to remove these adsorbed gas molecules is by a physical process using low energetic Ar ions to bombard on the

surface. The adsorbed gas molecules on the surface could be removed. The typical energy for the ions is less than 3 keV. Normally, the energy is kept at minimum to reduce the damage of the surface crystallinity. Normally, AES or XPS will be performed to assess the cleanliness of the surface. Typical surface impurities are carbon and oxygen.

3.4 Experimental parameters

3.4.1 Temperature

The sample is heated by using electron beam bombardment. The temperature of the sample is read from the thermocouple type-K was used in this thesis work. It is inserted under the zinc foil placed on the sample holder to monitor the temperature of the zinc foil during heating. This thermocouple can read temperature up to 1200 °C. To study oxidation of the zinc foil in UHV environment at elevated the temperature. The temperature is raised from room temperature (27 °C) to 110 °C, below the melting point of zinc foil (410 °C).

3.4.2 Gas flow

Argon and oxygen gases used for sputter cleaning and oxidation of zinc foil surface, respectively. The gas was let into the analysis chamber along stainless steel tubing. Good control of these gas flows is achieved using a combination of needle valves and CCG gauge controllers. Sputter cleaning is a standard *in situ* cleaning process used to obtain clean zinc foil surfaces. Argon gas is widely used for this process due to it is noble gas and thus does not interact chemically with other gases. Argon gas of high purity 99.99% was let into the preparation chamber, raising the

vacuum pressure from the base pressure to $\sim 3 \times 10^{-6}$ Torr for sputtering process. While the oxidation of zinc foil by exposure of a clean surface to oxygen, oxygen gas of ultra high purity 99.9995% was let into the system, raising the pressure from the base pressure to $\sim 5 \times 10^{-7}$ Torr .

3.5 Sample holder

The sample holder is attached to one end of the manipulator. Thus the sample can be transferred between the preparation chamber and the analysis chamber. In addition, the manipulator is used to move and rotate the sample to align the samples inside the UHV system with respect to the synchrotron light beam and the angle of emissions of photoelectrons. The sample holder is equipped with an electron-beam heater and type K thermocouple. The photo of the sample holder used in the ARPES and XPS chamber is show in Figure 3.10 a) and b), respectively.

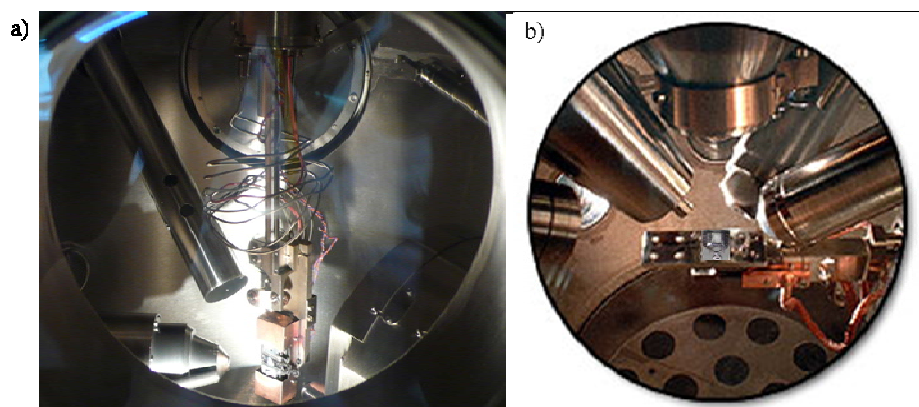


Figure 3.10 The sample holders are used in the UHV at BL3.2a, a) used in the ARPES chamber, b) used in XPS chamber.

3.6 Energy analyzer

Different types of energy analyzer have long been developed. These are a plane mirror analyzer (PMA), a cylindrical mirror analyzer (CMA), cylindrical deflection analyzer (CDA) and concentric hemispherical analyzer (CHA). The principles of all types of analyzers are described in chapter II. Considering performance and ease of construction, CHA is the most suitable for photoemission techniques. The main advantages of CHA are high resolution and high transmission, and UHV compatibility. In addition, an electron static lens can be integrated into the analyzer allowing longer working distances and controllable size of the analyzed area.

The photoemission experimental station of BL3.2a is also equipped with two CHA electron energy analyzers manufactured by Thermo VG Scientific. The first one is an ALPHA110 energy analyzer. The second one is a CLAM2 analyzer. Both ALPHA110 and CLAM2 analyzer will be described in the following.

3.6.1 ALPHA110 energy analyzer

An Alpha110 energy analyzer is a hemispherical analyzer. It is to provide a high performance analyzer of surface analysis applications. It has a rather wide gap between the two hemispheres. The detector is a multi-channeltron array, consisting of 7 channeltrons. The main advantage of using channeltrons is that they have high sensitivity and a large dynamic range. More importantly, they are cheaper than multi-channel detector (MCD). The energy resolution can be selected by selecting the width of the entrance slit of the analyzer. Four different widths controlled by a single rotary drive are available for selection. The ultimate value of energy resolution of the

Alpha110 analyzer is less than 5 meV. The energy resolution of the analyzer is given by this equation.

$$\Delta E = E_p \left(\frac{W}{2R} + \frac{\alpha^2}{2} \right), \quad (3.5)$$

where, W is the width of the slit, R is the mean radius of hemisphere, E_p is the pass energy, α is the acceptance angle. It is clearly that, ΔE is independent on the, W , R , and E_p , but it is dependent only on the acceptance angle α . This angle is determined by the width of the entrance slit. For the Alpha110 energy analyzer, an Alpha plate is fitted at the entrance slit of analyzer. The Alpha plate is used for limiting the acceptance angle for finding optimum energy resolution, in a combination with the width of the slit. Figure 3.11 shows the analyzer cross-section and the position of the Alpha-plates. The Alpha110 energy analyzer installed at the photoemission experimental station of BL3.2a is also shown in the photo in Figure 3.12.

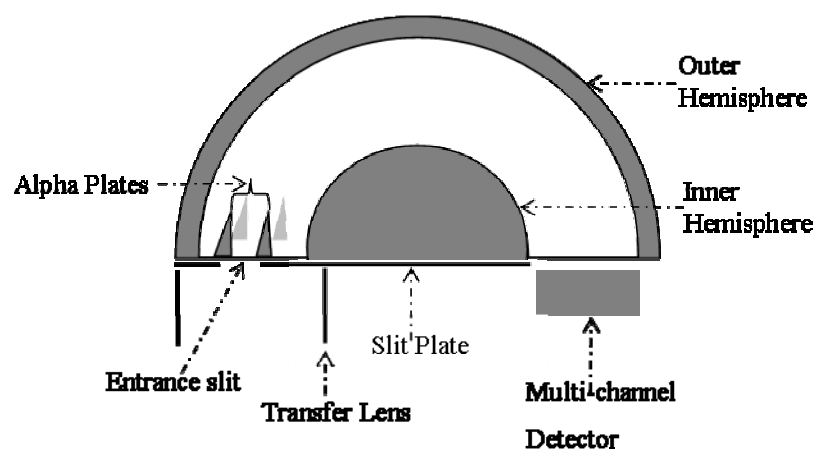


Figure 3.11 Schematic diagram of the ALPHA110 CHA showing the analyzer cross-section and position of Alpha plates.



Figure 3.12 The photo of the ARPES system showing the Alpha110 energy analyzer at BL3.2a of SLRI.

Table 3.1 Specifications of the Alpha110 energy analyzer.

Analyzer	110 mean radius hemispherical
Lens	Multi-element input lens
Detector	Flange-mounted 7-channeltron detector
Energy resolution	< 5 meV
High sensitivity	For XPS, UPS, AES
Angle resolved	XPS capability
μ -metal	For good performance at low kinetic energy

3.6.2 CLAM2 energy analyzer

A CLAM2 energy analyzer is a mean radius of 100mm and 150° spherical sector analyzer. It was designed to be used for AES, XPS, UPS, and other techniques. The CLAM2 spectrometer is installed on the XPS system, which is dedicated for chemical analysis. The CLAM2 consists of three main parts the lens, analyzer and detector as shown in the Figure 3.13.

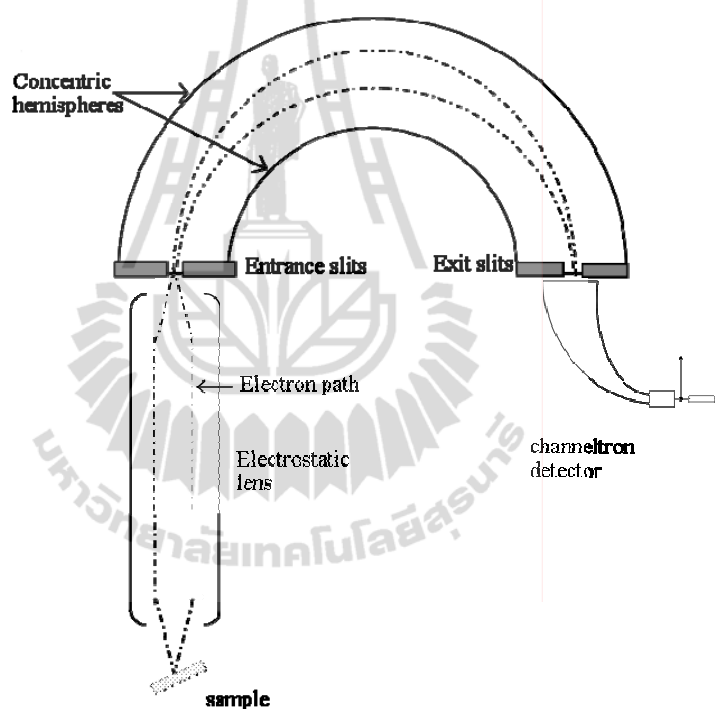


Figure 3.13 Schematic diagram of CLAM2 energy analyzer.

The lens of CLAM2 is an electrostatic lens, consisting of two elements. It is an optical element to transfer the electron source on the sample to be at the entrance slit of the energy analyzer. It is designed to focus electrons emitted from the sample at the position of the entrance slit of analyzer. The analyzer acts as a narrow band filter, electrons with too high energy will hit the outer hemisphere and electrons with too low energy will hit the inner hemisphere. Consequently, only electrons having

specific energy level can pass through the exit slit of analyzer to the detector. The detector used in CLAM2 is a channeltron. The CLAM2 analyzer is used at PES beamline as shown in Figure 3.14 it is fitted to the XPS system.



Figure 3.14 The photo of CLAM 2 energy analyzer on the XPS system at BL3.2a.

Table 3.2 Specifications and Operating Voltage of CLAM 2 analyzer.

Analyzer	100 mm mean radius
Lens	Electrostatic lens
Detector	Single Channeltron
Inner Hemisphere	0 to -2500 V
Outer Hemisphere	0 to -2500 V
Retard	0 to -2500 V
Magnetic	0-3 A
Lens N	0 to -8000 V
Lens R	0 to -8000 V

3.7 Electron gun

The electron gun at the experimental station of BL3.2a is used as an excitation source for AES measurements. The schematic diagram of the gun is illustrated in Figure 3.15. It consists of five main components, i.e., a filament, grid, lenses, apertures and scanning quadrupoles. This electron gun is a LEG63 model manufactured by the Thermo VG Scientific. The LEG63 model is a medium resolution and electron beam energy of 5 keV, this source was designed for pulse counting AES. The electron beam can be produced by hot filaments and focused onto a sample by the electron lenses which may be either magnetic or electrostatic. For the magnetic lenses there have low aberration and provide the best performance. However, these lenses have some problems due to the fact that they are complicated and expensive. For the electrostatic lenses are easier to connect in a UHV system. Electrostatic gun could be easily used and the spatial resolution of the order of a micron. Electrostatic lenses are used in the LEG 63 model which the spot size is less than 50 μm at beam current of 10 nA. A good working distance is about 60 mm between source and sample.

For AES measurement when sample is excited by an electron beam from electron gun then Auger electron emitted from the sample with appropriate kinetic energy pass through the entrance slits located in front of the input lenses and exit slits of the analyzer when the potential difference between two hemispheres is applied. Then these electrons are directed into the channeltron or electron multiplier located at after the exit slit is used to detect the electrons. Varying voltage at the sweep supply and then the Auger data can be obtained, usually these spectra more pronounced by electronic spectral differentiation.

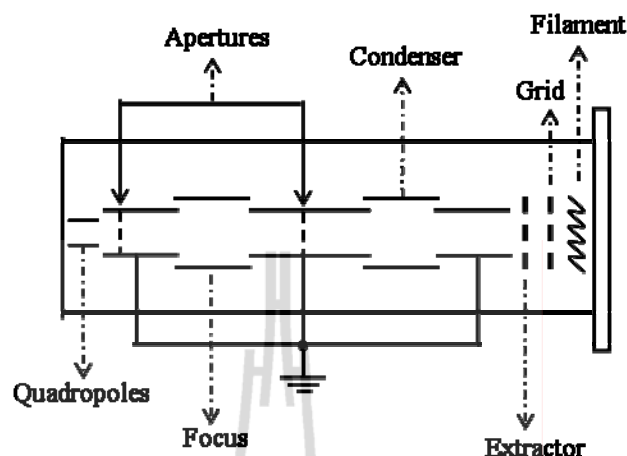


Figure 3.15 Schematic diagram of the LEG63 Electron gun.

3.8 Ion gun

The ion gun is an electron impact ion source then generates ions from a gas introduced into the gun. Primarily, it was designed and developed by Thermo VG for sample cleaning in surface analysis experiments. The ion gun EX 03 was used in this thesis work as shown in the Figure 3.16. Several gas species, such as argon, (Ar), helium (He), Ne, Rr and Xenon (Xe) are allowed to use for this ion source. The argon gas is the most commonly used for sputter cleaning of samples.

Figure 3.17 is a schematic diagram of the EX 03 ion gun. The general function of the EX03 ion gun is to ionize gas atoms in the source of ion gun. Then they are accelerated and pass through the sample, these process are controlled by the lens column. Ions are produced at high positive potential and then are accelerated them through the gun to produce a beam of ions, the ion beam energy in a range from 500 eV to 3.0 keV.

Gas is fed into the source and a needle valve is used to control the rate of flow of gas. A filament within the source region is heated to emit electrons. So that

electrons are accelerated into the source cage. The electron motions in the source cage and some electron hit with gas atoms. That is causing removing negatively charge and forming positively charged.

The ions generated in the ion source are accelerated pass through the aperture in the extractor lens element, can occur at the positive potential. Then the ion beam is shaped and focused on to the sample by using the electrostatic lens. The pressure should be less than 1×10^{-5} mbar for operation and maintenance of the equipment. Table 3.3 is shown the specifications of the EX 03 ion gun which is used at the PES beamline.



Figure 3.16 The photo of the EX 03 ion gun at the PES beamline.

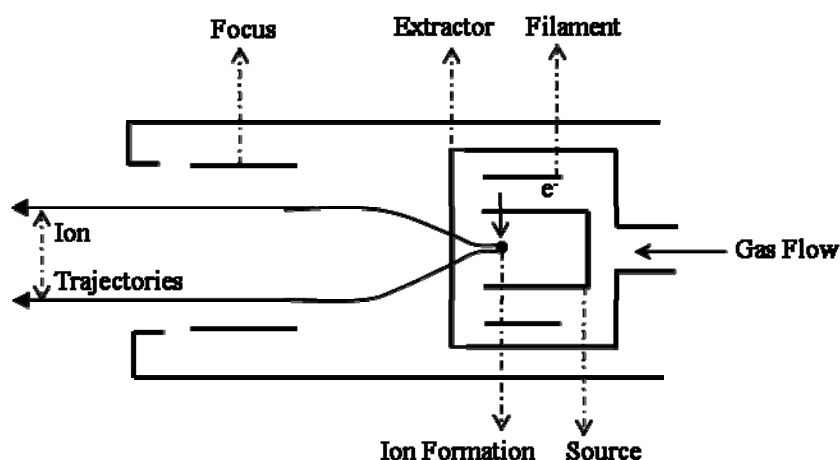


Figure 3.17 Schematics diagram of the EX 03 ion gun.

Table 3.3. Specification of EX 03 ion gun.

Energy range	300 eV to 3000 eV
Target currents	>20 μ A (at 3 keV) >10 μ A (at 500 eV)
Working distance	100 mm (50-200 mm)
Gas species	Ar, He, Ne, Kr, Xe. (inert gases)
Operating pressure	$<1 \times 10^{-5}$ mbar.
Mounting flange	70 mm UHV

3.9 AES and PES measurements

AES and PES measurements in this thesis work were carried out using two different systems as described below.

First part of the experiments of AES and PES was performed at the in the ARPES system of beamline 4. These measurements were carried out with the set-up as shown in Figure 3.18. For PES measurements, the sample was aligned in such way that the sample surface was oriented at 50 degrees with respect to the incident synchrotron light beam. The Alpha 110 analyzer is fixed to the photoemission chamber at the angle of 0° (normal emission) with respect to the sample surface. The energy of the photons was chosen to be 51 eV for PES measurements. For AES measurements, the 5 keV electron beam was used for the excitation.

After loading the samples was into the UHV system, the surface of sample was cleaned by Ar^+ ions sputtering until the cleanliness of the surface of the sample was achieved. To form ZnO by exposure of a clean surface to oxygen the substrate at

room temperature, oxygen gas was let into the photoemission system, raising the vacuum pressure from the base pressure of $\sim 1 \times 10^{-10}$ Torr to $\sim 5 \times 10^{-7}$ Torr for various exposure times.

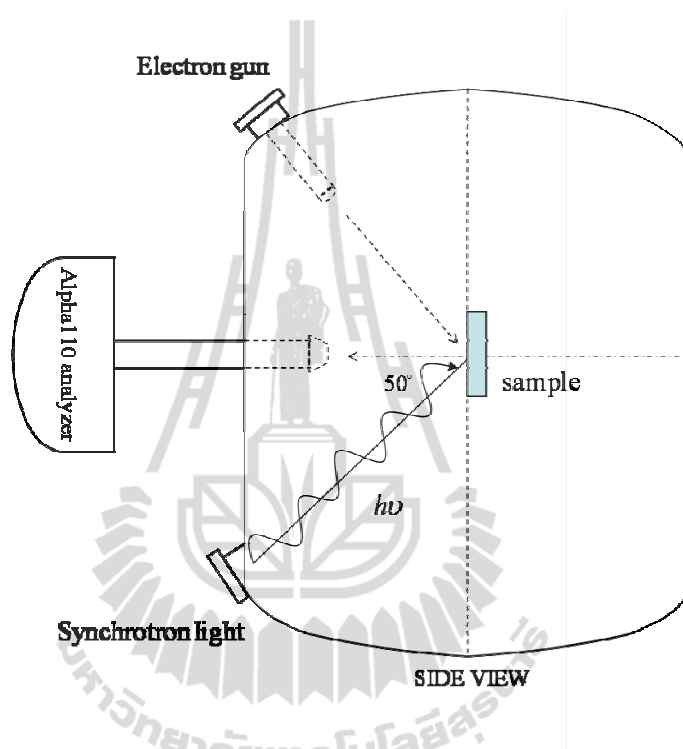


Figure 3.18 Schematic diagram of PES measurements set-up (ARPES system).

The second part of the experiments was performed at BL3.2a in the XPS system. PES measurements were carried out with the set-up as shown in Figure 3.19. The CLAM 2 analyzer is fixed at the angles of 50° with respect to the sample surface of normal. While the synchrotron light source port is fixed at the angle of 40° with respect to the surface of normal. ZnO formed by O_2 exposure of clean zinc foil in UHV at elevated temperature were performed in this system. To obtain a good reference photoelectron spectrum of a clean Zn surface, the measurements were performed at the base pressure of $\sim 2 \times 10^{-10}$ Torr. Thus one of the samples was

introduced into the analysis chamber thru a load-lock system to prevent breaking of UHV condition. The clean surface was obtained by 0.5 keV Ar⁺ ion sputtering in the analysis chamber.

All PES spectra were normalized to the incidence photo flux measured by the drain current of a gold mesh located between the post-focusing mirror and the sample.

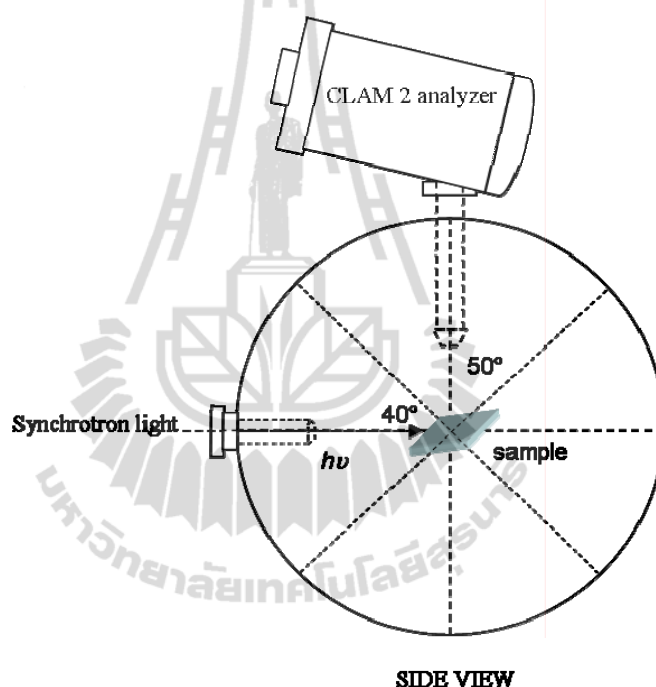


Figure 3.19 Schematic diagram of PES measurements set-up (XPS system).

3.10 Subtract background of photoelectron spectra

Photoemission spectra from measurements consist of intrinsic spectra and extrinsic spectra or the secondary electrons background. In this thesis work the secondary electrons background of the spectra was subtracted using Shirley type background (Shirley, 1972), which was explained in chapter 2.6, this method suitable for quantitative analysis of the surface. Figure 3.20 shows the photoelectron spectrum

before and after background subtraction. The background is also shown in the figure. The background is considered to occur during the transport of the electrons to the surface. The dot curve (SIG) is the raw data from experimental of clean zinc foil, the dot-dash curve is Shirley background (BG), and the solid curve (SIGsBG) is spectrum after background subtraction.

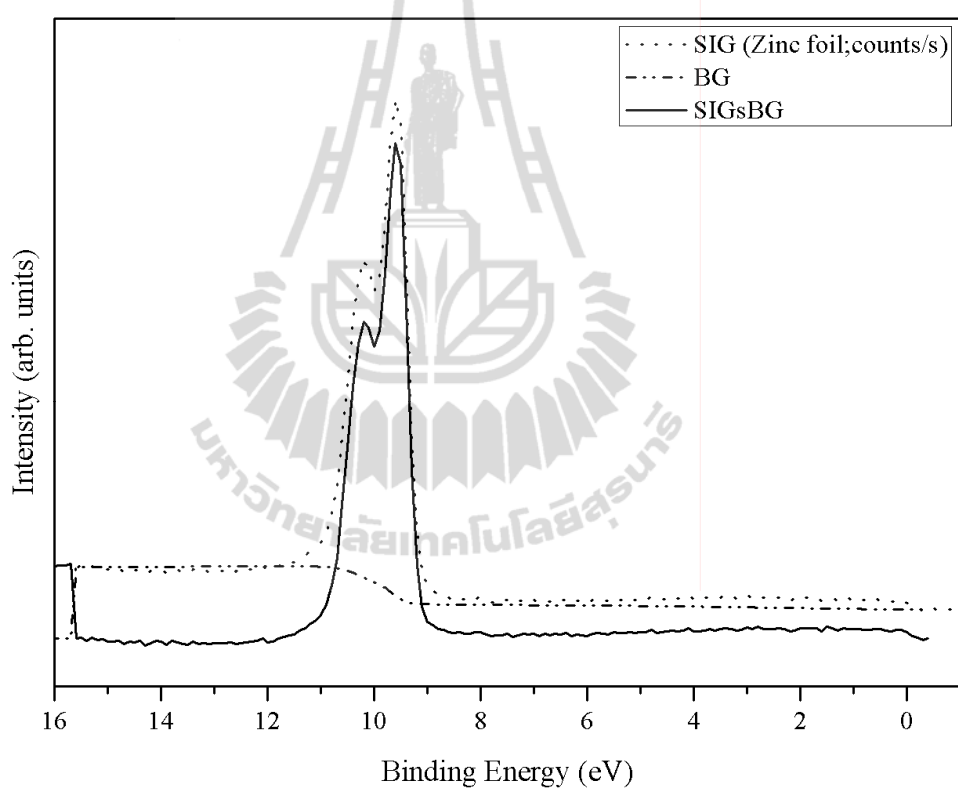


Figure 3.20 The photoelectron spectra before and after subtraction of secondary electrons component of the background.

CHAPTER IV

RESULTS AND DISCUSSION

In this work, the formation of ZnO was prepared by exposing Zn foils in air and in an UHV environment. To investigate the initial stage of oxidation process, oxidation of zinc was performed in a controlled environment, i.e., in UHV conditions and the measurements were performed *in situ*. The main parts of this work concentrate on *in situ* investigations of clean Zn foils exposed to oxygen in UHV conditions at temperatures of 110 °C and below. Synchrotron PES was used as an *in situ* technique to study the oxide films. The formation of ZnO induced by ion sputtering will also be reported.

4.1 PES and AES of Zn foil and ZnO single crystal (0001)

The necessity for clean conditions and careful surface preparation for studies of the early stages of oxidation has been known for many years. This is because the initial stages of the oxidation process are usually sensitive functions of the conditions of the surface. Proper surface cleaning procedure is necessary to assure reliable experimental results. Surface contaminants such as carbon, oxygen, or other elements must not be present on the surface of zinc prior to oxidation. Surface cleaning by Ar⁺ ion sputtering of the starting Zn foils has carefully been examined. A Zn (0001) single crystal sample has also been used for comparison. AES is the main technique to verify

the cleanliness of the surface. PES spectra were also been used to double check the surface conditions prior to exposure of the samples to oxygen.

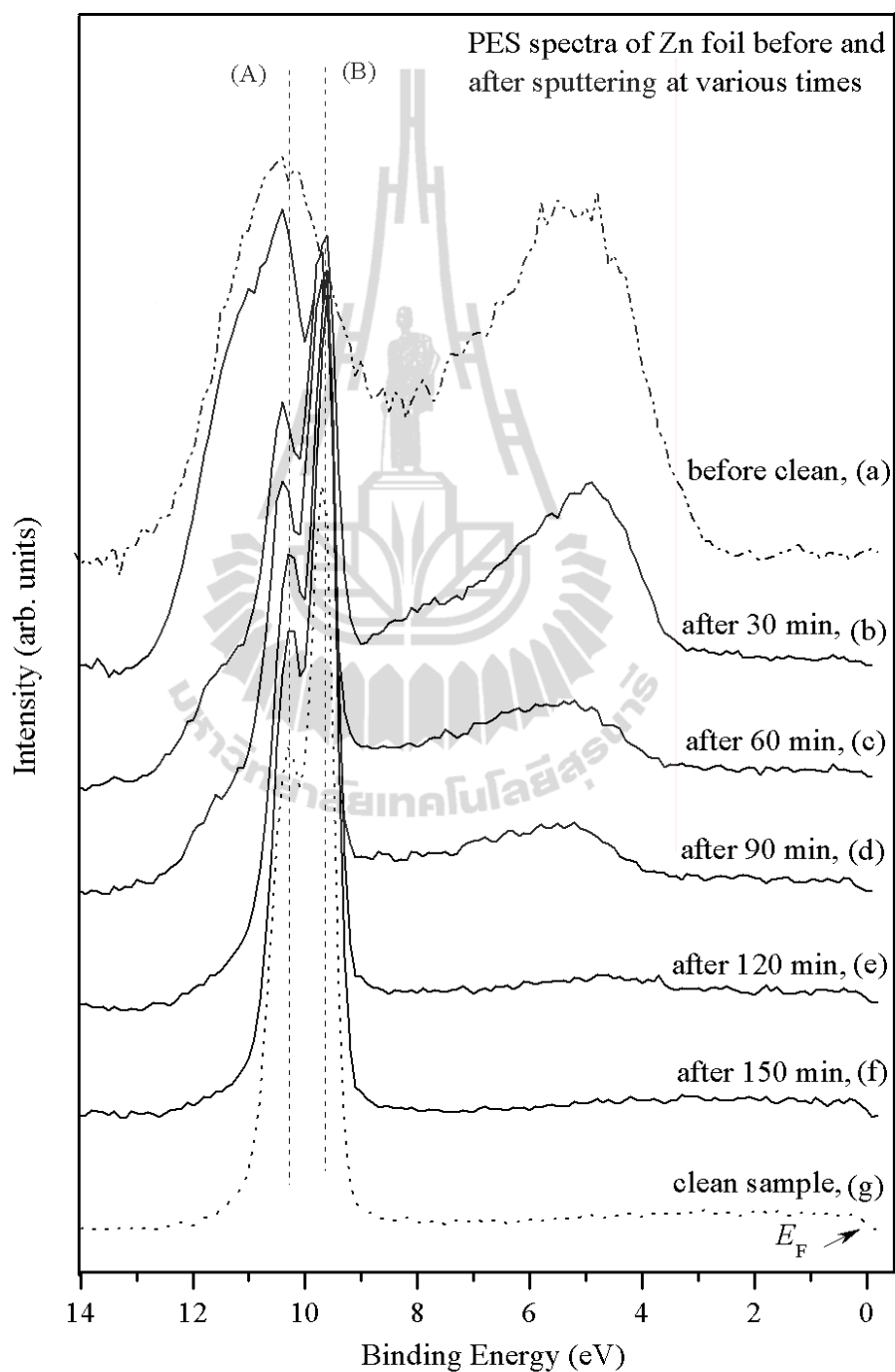


Figure 4.1 Series of photoelectron spectra of zinc foil taken (a) before and (b-g) after surface cleaning by 500 eV Ar^+ sputtering for different sputtering times.

Figure 4.1 shows the series of photoelectron spectra of metallic Zn foil before and after surface cleaning by Ar^+ ions sputtering with an ion energy of 500 eV for various times. The sample was introduced into the PES system without sputtering contains large amount of surface contaminations. Cleaning process by ion sputtering was repeated as many times as necessary until the contamination such as carbon or oxygen was removed from surface below the detection limit. The results shown in the figure are from the sputtering cycle of 30 minutes. Before and after each sputtering cycle, the PES spectrum was taken to check a clean surface of sample. The energy of the excitation for PES measurements was 51 eV. The measured spectrum is normalized with the photoelectron current measured by a gold mesh placed in between the post focusing mirror and the sample (Songsiriritthigul *et al.*, 2001). The secondary electrons background of the spectra was subtracted using the Shirley method (Shirley, 1972). This method was used in the spectral analysis was carried out throughout this thesis work. The spectrum of Figure 4.1(a) drawn with a dash-dot curve was taken from a Zn foil before sputter cleaning. The distinguished features are the two broad peaks. The one covering the regions from 8 to 12.5 eV may be attributed to a Zn 3d peak while the other covering from 2 to 7.5 eV may be attributed to surface contamination. The binding energy in this thesis work was referred directly to the Fermi level. The Fermi level of Zn foil was calibrated to be at 0.0 eV (Briggs, 1975; Barr, 1994). The solid curves as shown in Figure (b) to (f) are series of spectra after sputter cleaning at various times. With a longer sputtering time, the Zn 3d peak become narrow and shifts toward lower binding energy. The peak at lower binding energy, associated with surface contaminations, decreases with a sputtering time, as expected. The spectrum of a clean Zn surface is shown in Figure 4.1(g), plotted with a

dotted line. It contains two sharp overlapping peaks labeled as A and B (at 10.5 and 9.9 eV), corresponding to Zn $3d_{3/2}$ and $3d_{5/2}$ energy levels, respectively. The Zn $4s$ valence band of the clean metallic Zn is seen as a broad band from the Fermi level extending to the Zn $3d$ band. It is interesting to note that when the Zn metal transforms to ZnO, the Zn valence electrons near the Fermi level are reduced due to the electrons from $4s$ transfer to the oxygen atoms. This means that the oxygen atoms bond with Zn atoms to form ZnO. As a result, O $2p$ - Zn $4s$ bonding is appeared in the valence band regions, while the intensity of Zn $3d$ peak is decreased and the peak is shifted towards higher binding energy.

Figures 4.2(a)-(d) show the derivative Auger spectra of Zn foil taken (a) before and (b-d) after cleaning by sputtering with Ar^+ ion 500 eV for various times. The AES spectra were measured with the primary electron energy of 5 keV at an angle of normal emission with respect to the surface normal. The AES spectrum of Figure 4.2(a) was taken before sputter cleaning. The spectrum shows the main peaks of Zn *LMM* (997 eV) and the peaks resulting from surface contaminations, i.e., C *KLL* (272 eV) and O *KLL* (510 eV). Figure 4.2(b) indicated that carbon was removed by Ar^+ cleaning sputtering for 60 minutes. The peak to peak amplitudes of the first derivative of oxygen decreases by Ar^+ sputtering for 120 minutes, as shown in Figure 4.2(c). After sputtering for 180 minutes, no carbon and oxygen were observed as shown in Figure 4.2(d).

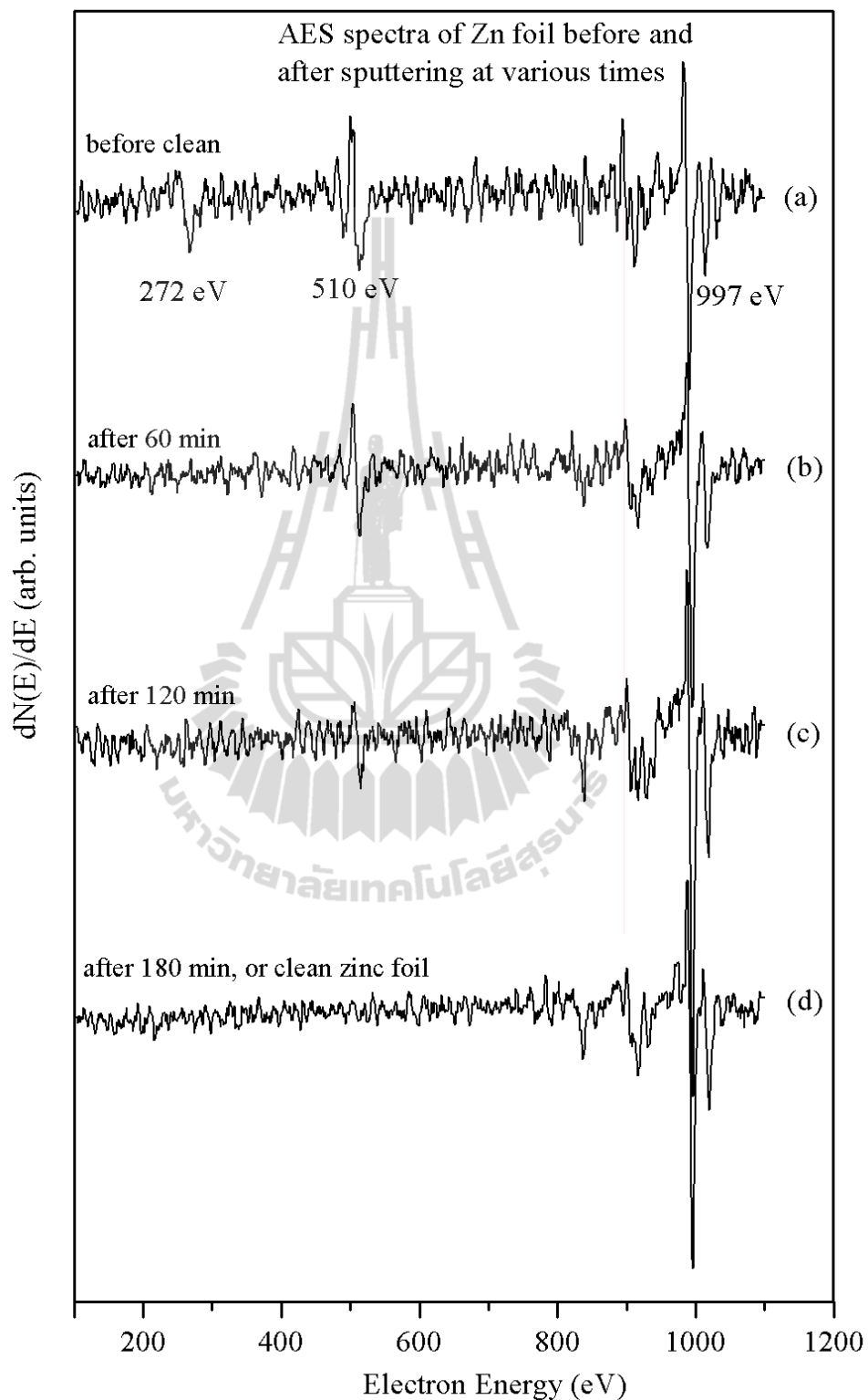


Figure 4.2 The first derivative Auger spectra of Zn foil (a) before and (b-d) after sputtering by using 500 eV Ar^+ ions.

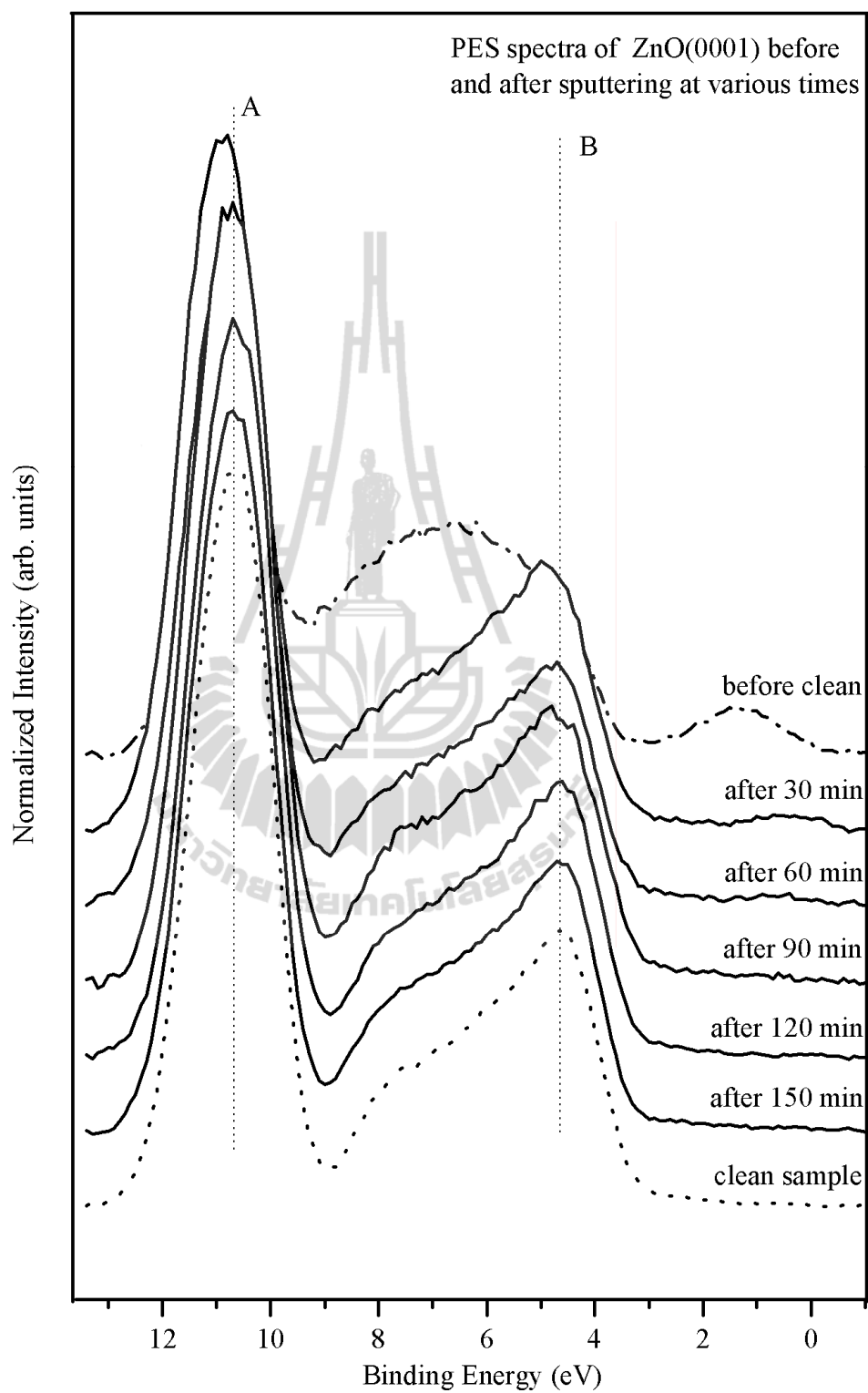


Figure 4.3 Series of photoelectron spectra of ZnO (0001) spectra before and after sputtering for various times.

Figure 4.3 shows the photoelectron spectra of a single crystal of ZnO (0001) surface before and after Ar⁺ ion sputter cleaning for different sputtering times. The series of ZnO (0001) spectra were measured with a photon energy of 51 eV and the spectra were taken at normal emission of the photoelectrons with respect to the surface of sample. The spectrum of the as-introduced sample, without cleaning, (dash-dot curve) shows the peak corresponding to Zn 3*d* at around 11 eV, the broad peak covering 4-9 eV binding energy and the small peak at ~1.5 eV. These peaks indicate that there are contaminations on the surface of the ZnO sample. After each 30-minute cycle of Ar⁺ ion sputtering, the PES spectrum was taken. It was found that the features of the valence band after sputtering deviate from those of the spectrum before sputtering. The peaks at ~1.5 eV and at ~7.5 eV reduce with the sputtering time, indicating the reduction of the surface contaminants. The surface contaminations also cause the increase of the binding energy of the Zn 4*s*. The surface contaminants could be removed to the level below the detection limit of the measurement system by sputtering repeatedly. The PES spectrum of a clean surface is represented in the bottom spectrum with a dot curve. In this spectrum, the Zn 3*d* electron peak is located at around 10.8 eV, and O 2*p* - Zn 4*s* peak is located at around 5 eV. These two peaks are labeled A and B, respectively.

The surface contaminants on the ZnO sample were identified by AES. Figure 4.4 shows the AES spectra of the single crystal ZnO (0001) from (a) before and (b-d) after Ar⁺ ion sputtering for various times. From AES measurements, the surface of the sample without surface cleaning contains impurities such as carbon and oxygen. The AES spectrum of the sample without cleaning is shown in Figure 4.4(a). The peaks at 216, 272, 510, and 997 eV correspond to Ar *LMM*, C *KLL*, O *KLL*, and Zn *LMM*

Auger signals. After sputtering for 60 and 120 minutes, carbon atoms were removed below the detection limit, as shown in Figures 4.4(b) and (c). A significant amount of argon were still observed in the sputtered sample. This residual argon gas may occur from the cleaning process. Further sputtering could remove argon from the surface as shown in Figure 4.4(d). Thus, only O *KLL* at 510 eV and Zn *LMM* at 977 eV Auger signals were detected for the sample which is referred as a clean sample in this work.

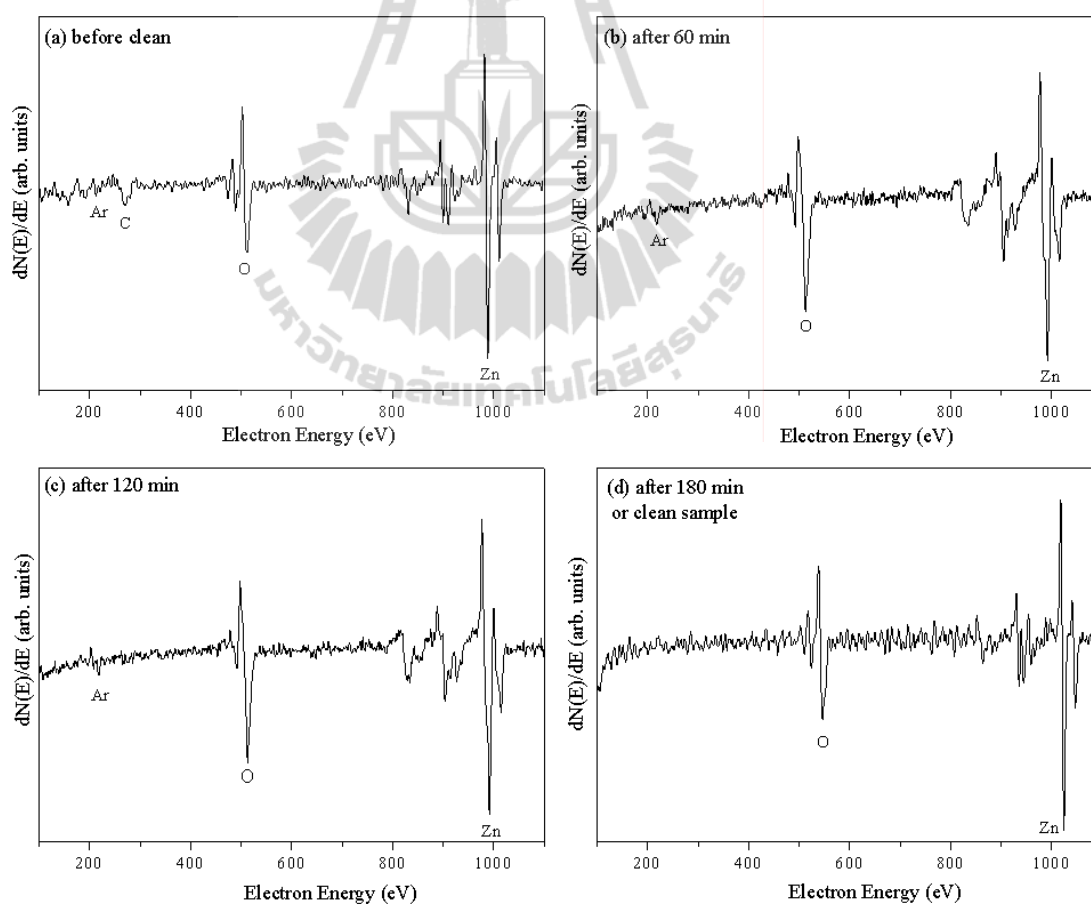


Figure 4.4 The first-order derivative of Auger spectra of a single crystal ZnO (0001) sample (a) before and (b)-(d) after sputtering with 500 eV Ar^+ ion for various times.

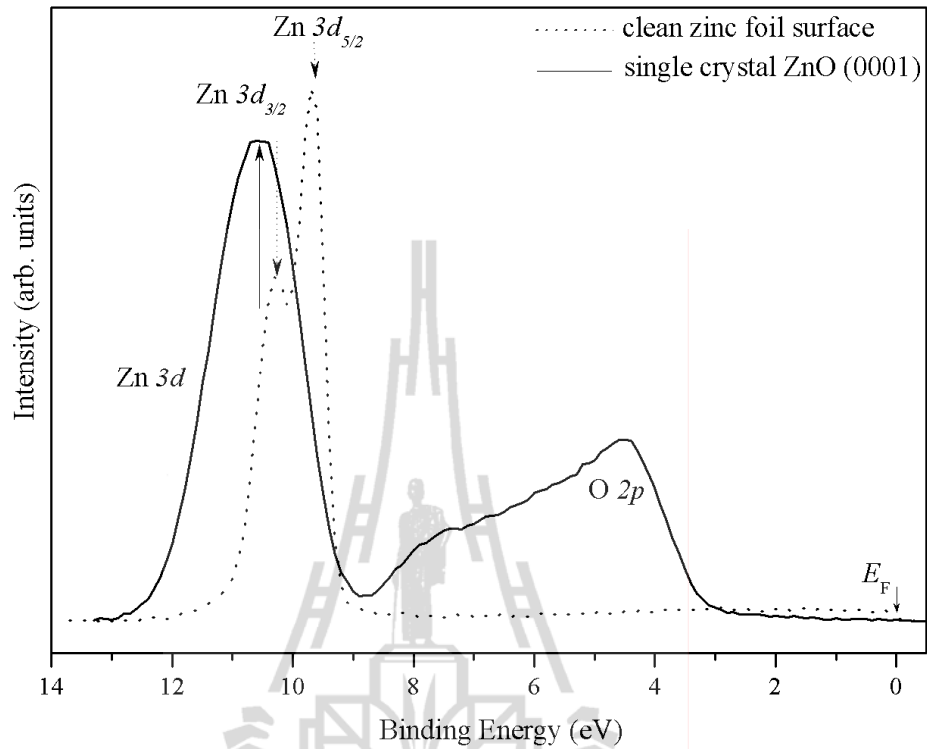


Figure 4.5 Photoemission spectra of a clean Zn foil and a clean single crystal ZnO (0001).

Figure 4.5 shows the photoelectron spectrum taken from a clean Zn foil (dot curve) in comparison with that taken from a clean single crystal ZnO (0001) (solid curve). The Zn $3d_{3/2}$ peak of the metallic Zn is located at 10.5 eV below the Fermi level while the Zn $3d$ peak of a single crystal ZnO is located at 10.8 eV. The photoemission spectra of metallic Zn and ZnO show a difference of 0.3 eV in the peak positions that shifted toward higher binding energy for the ZnO sample. The Zn $4s$ for the metallic Zn appears as a very broad band starting from the Fermi level.

For the ZnO (0001) sample, the valence band of the O $2p$ bond with Zn $4s$ could be observed from about 4-9 eV region and Zn $3d$ at higher binding energy

(Girard *et al.*, 1997). The lowest conduction band is mainly composed of $4s$ electrons while $4p$ electrons are in unoccupied levels in the conduction band (Matsunaga *et al.*, 1999). An energy difference between the maximum valence band and the lowest conduction band is an energy gap (E_g). The valence band maximum is obtained by a linear extrapolation as illustrated in Figure 4.6. In this case, the maximum valence band was found to be ~ 3.1 eV below the Fermi level.

Figure 4.7 shows the energy level diagram for the surface of ZnO (a), and an electron band diagram for n -type ZnO semiconductor (b). A schematic sketch from the PES spectrum of ZnO film is given in Figure 4.7 and can confirm that undoped ZnO film exhibit n -type nature in a way that the Fermi level is close to the conduction band minimum. The Fermi level of the n -type ZnO located at ~ 0.3 eV below the conduction band minimum was been reported by Jacobi *et al.* (1984). When the p -type ZnO is formed, the Fermi level shall be located just above the valence band maximum and thus can easily be observed from PES spectra.

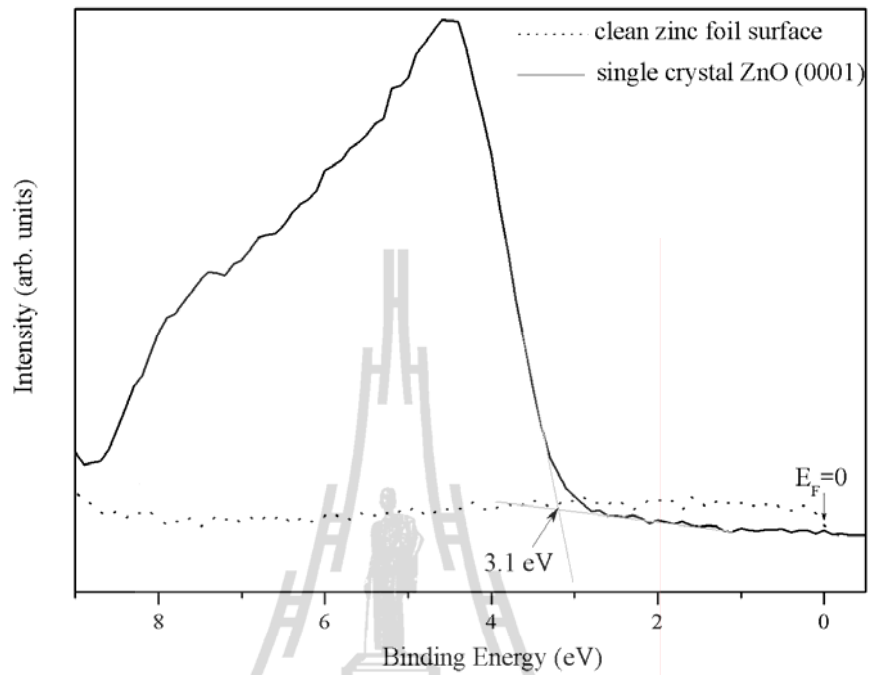


Figure 4.6 Magnified plot of figure 4.5 at the binding energy ranging from 0 to 8.5 eV, below Fermi level.

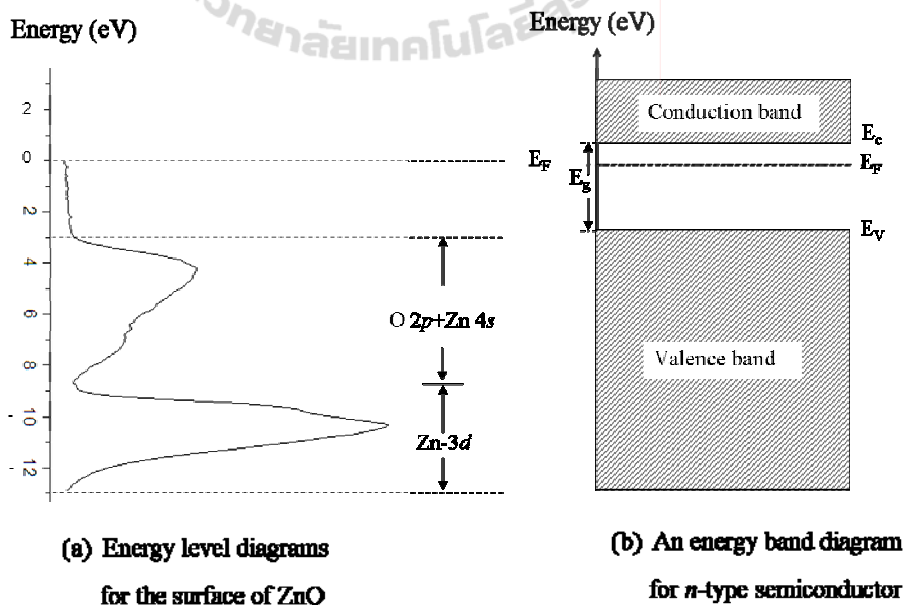
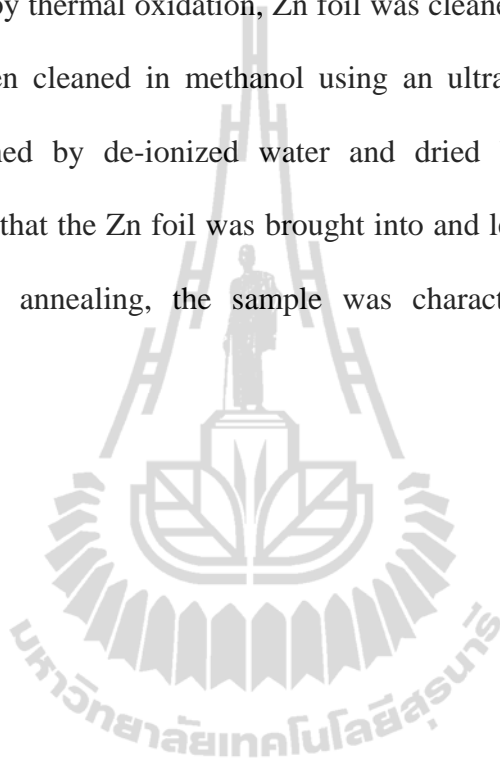


Figure 4.7 The energy level diagram for the surface of ZnO (a), and an energy band diagram for *n*-type ZnO semiconductor (b).

4.2 ZnO formed by thermal annealing at 150 °C in air

It is interesting to examine the formation of ZnO by oxidation of a Zn foil in air. This was easily done by thermal annealing a cleaned Zn foil in air. Prior to the formation of ZnO by thermal oxidation, Zn foil was cleaned by bromide 10% dilution with methanol, then cleaned in methanol using an ultrasonic bath for 10 minutes subsequently washed by de-ionized water and dried by spraying nitrogen gas, respectively. After that the Zn foil was brought into and left in an oven at 150 °C for 30 minutes. After annealing, the sample was characterized by AES and PES measurements.



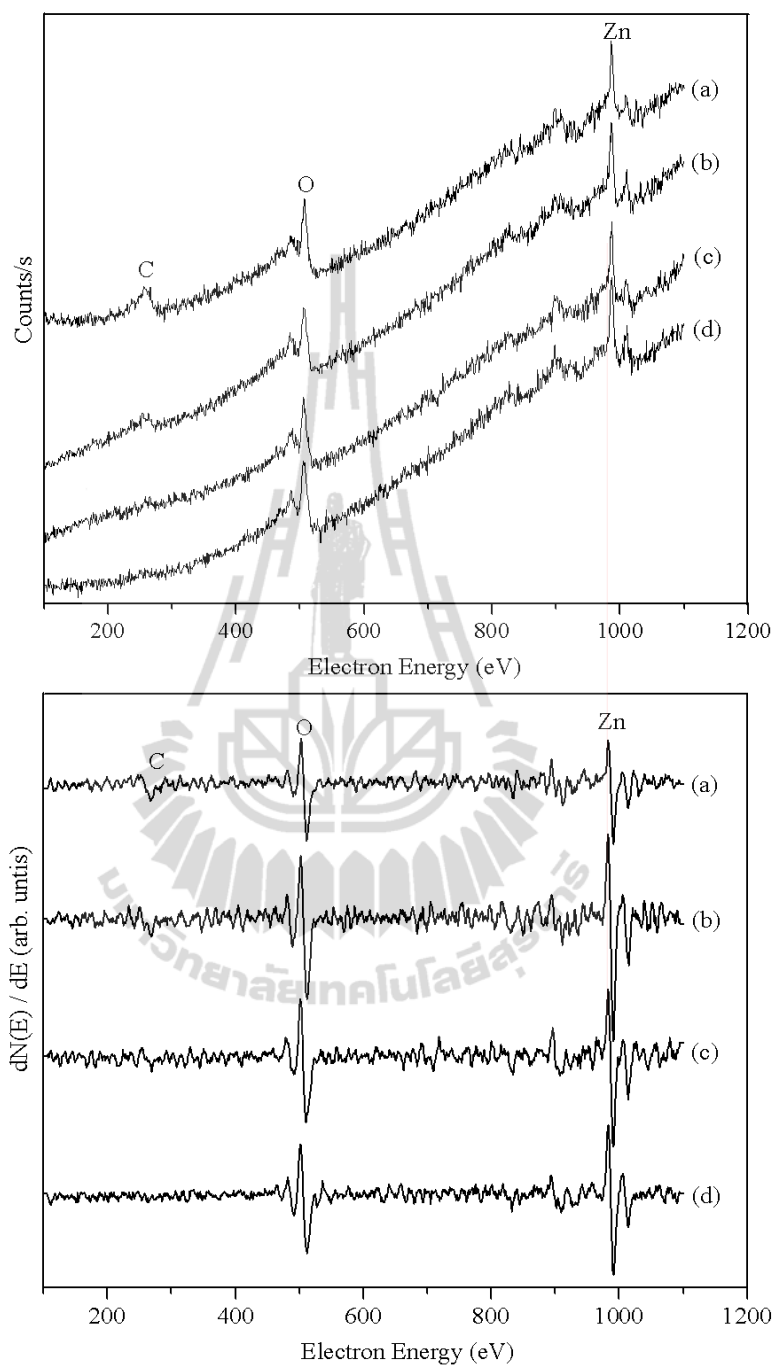


Figure 4.8 The Auger spectra of ZnO formed by thermal annealing at 150 °C in air for 30 min. The top figure shows raw AES spectra, the bottom figure shows the first derivative of AES spectra. The spectra and their derivative are shown for the sample (a) before and after cleaning by Ar⁺ ion sputtering treatments for 5, 10, and 15 minutes, curves (b) to (d), respectively.

Figure 4.8 shows the Auger spectrum of the ZnO formed by thermal annealing at 150 °C in air for 30 minutes. The top figure shows an undifferentiated form, whereas bottom figure shows differentiated form. The undifferentiated Auger spectra have very large background from secondary electron distribution, smearing out the Auger electron peaks this large background is decreased by the numerical differential highlighting the peaks processing. The derivative Auger spectra for the ZnO sample before surface cleaning are shown as the spectrum (a). The spectra (b)-(d) are for the ZnO sample taken after Ar⁺ ion sputtering for 5, 10, and 15 minutes, respectively. The spectrum of the ZnO sample without surface cleaning shows three peaks of the 272 eV C *KLL*, the 510 eV O *KLL*, and the 997 eV Zn *LMM*. The AES peaks acquired from the sample surface indicate that formation of ZnO can be easily prepared by thermal oxidation on polycrystalline metallic zinc foils. The major surface impurities were accumulated on the surface, i.e., C, CO₂, and CO. After sputtering by Ar⁺ ions, the peak to peak heights in the derivative curve of Zn and O (*KLL*, 510 eV) are increased, while the peak to peak height of the C *KLL* AES peak was diminished as shown in the Figures (b) and (c) for 5 and 10 minutes of Ar⁺ cleaning, respectively. The surface cleaning may be considered to be completed after 15 minutes Ar⁺ sputtering, and thus no carbon contamination was detected as shown as the spectrum (d).

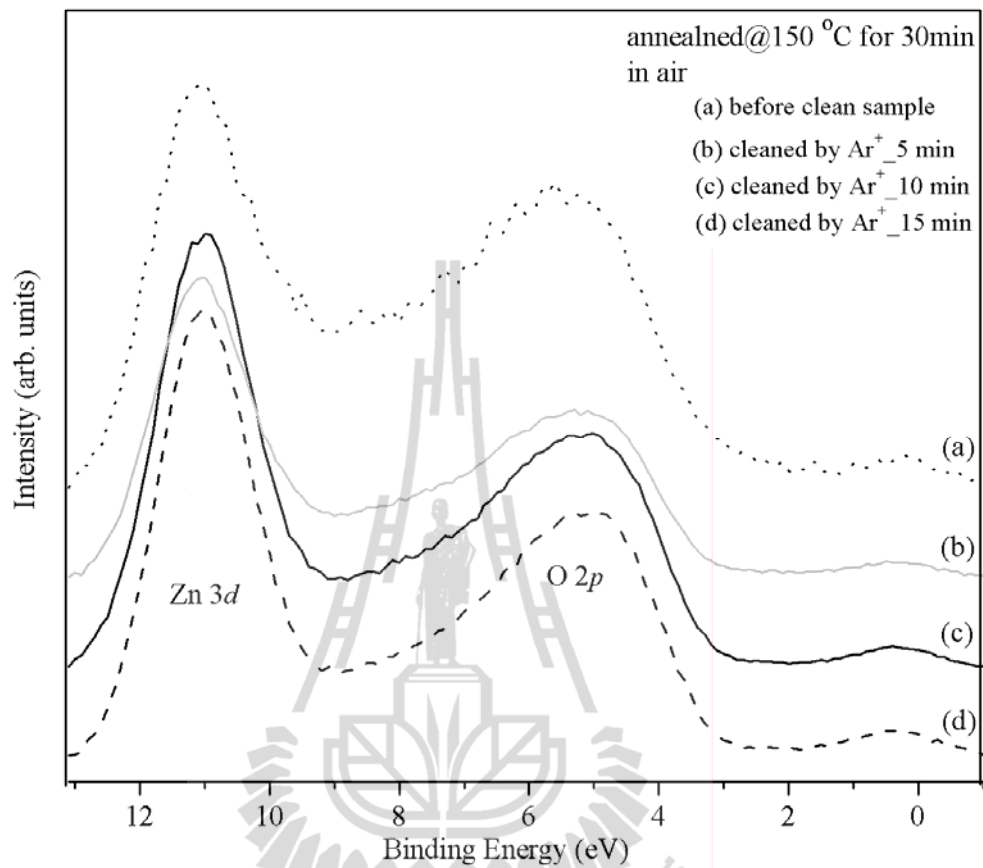


Figure 4.9 The Photoelectron spectra of ZnO formed by thermal annealing at 150 °C in air for 30 minutes. The figure (a) shows the spectra before cleaning sample, while (b) to (d) show those after sputtering, respectively.

Figure 4.9 shows the result of photoelectron spectra (PES) from ZnO prepared by thermal annealing at 150 °C in air for 30 minutes. The spectra contain three peaks. Those are the Zn 3*d* peak at the binding energy of about 11 eV, the O 2*p* peak covering the energy range of 3-9 eV, and the small peak near the Fermi level. The small peak near the Fermi level is likely from impurities. The spectrum (a) in Figure 4.9 (dot curve) shows the ZnO sample before surface cleaning. There are various features at different binding energies in the spectrum indicating that the surface of the ZnO sample is not clean, this is in agreement with AES measurement, as shown in

Figure 4.8(a). The photoelectron spectra of the same ZnO sample after cleaning by 500 eV Ar⁺ ion sputtering for 5, 10, and 15 minutes are shown in the gray solid curve (b), the solid curve (c) and dash curve (d), respectively. From AES measurement, the surface contaminations could be removed below the detection limit after sputtering cleaning for 15 minutes. Photoelectron spectrum of the clean sample shows the quite clear and sharp peak of Zn 3d.

4.3 ZnO formed by sputtering in Ar/O₂ mixed and O₂ ambient at room temperature

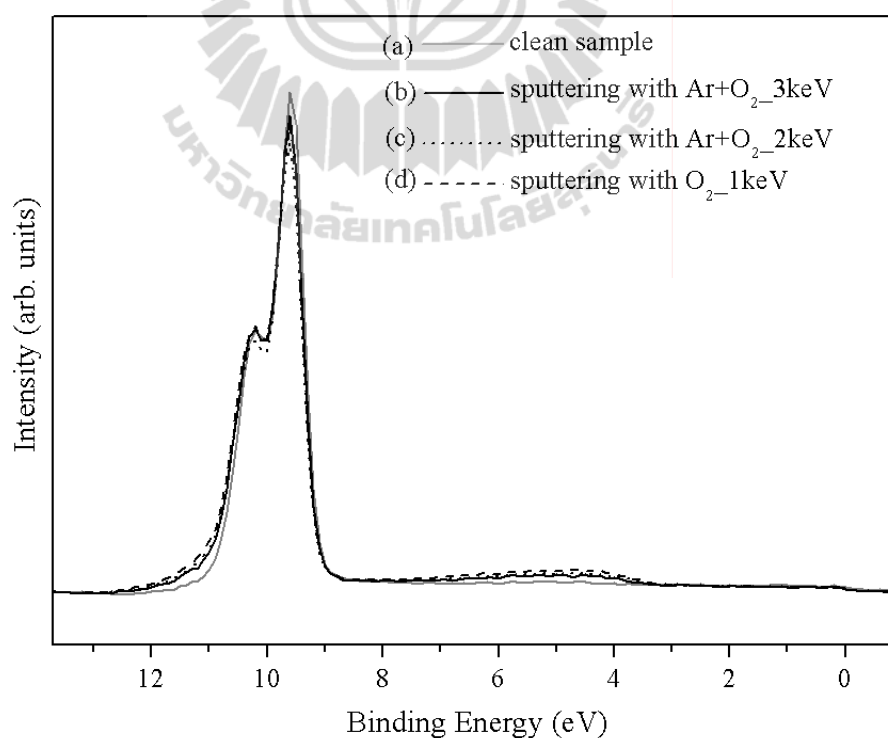


Figure 4.10 PES spectra taken from a clean Zn foil before (a) and after sputtering by 3 keV Ar⁺ ion in an ambient of O₂ at 5×10^{-7} Torr (b), 2 keV Ar⁺ ion in an ambient of O₂ at 5×10^{-7} Torr (c), and 1 keV O⁺ at pressure 1×10^{-8} Torr O₂ (d).

The possibility of form ZnO at vary O_2 pressures, $< 5 \times 10^{-7}$ Torr, has been examined, it's found that ZnO can be grown at pressure $< 10^{-7}$ Torr with assistance of ion beam sputtering. Figure 4.10 shows the PES spectra of Zn foil after sputtering with different ion energies for 5 minutes. The gray solid curve represents a clean zinc foil sample, solid and dot curves sputtering with Ar/ O_2 mixed gases for 3 and 2 keV, respectively. In this case, the argon gas was let into the analysis chamber from a base pressure 1.0×10^{-9} to 1.0×10^{-7} Torr, and then oxygen gas is increased up to 5.0×10^{-7} Torr, for 5 minutes. A dash curve is a sputtering with O_2 for 1 keV, the base pressure is 1.0×10^{-9} Torr and then O_2 pressure is increased up to 1.0×10^{-8} Torr for 5 minutes. The edge region of Zn the $3d$ peak at around 11.3 eV in solid and dot curves are slightly shifted towards higher binding energies, while a dash curve is shifted higher than those peaks for sputtering with Ar/ O_2 mixed gases. It is clearly seen in the binding energy range of 0 to 9 eV, this region is covering the valence band of ZnO (see Figure 4.11), the dash curve increases higher than the dot and solid curves in the this region. While near the Fermi level in the binding energies (0 to 3.0 eV), the dash curve is lower than gray solid curve. It means that interaction between O and Zn to form ZnO in case of sputtering with only O_2 is faster than the sputtering with Ar⁺/ O_2 mixed gases even though the partial pressure of O_2 is lower. It may be conclude that the formation of ZnO could be enhanced by direct bombardment of energetic oxygen ions.

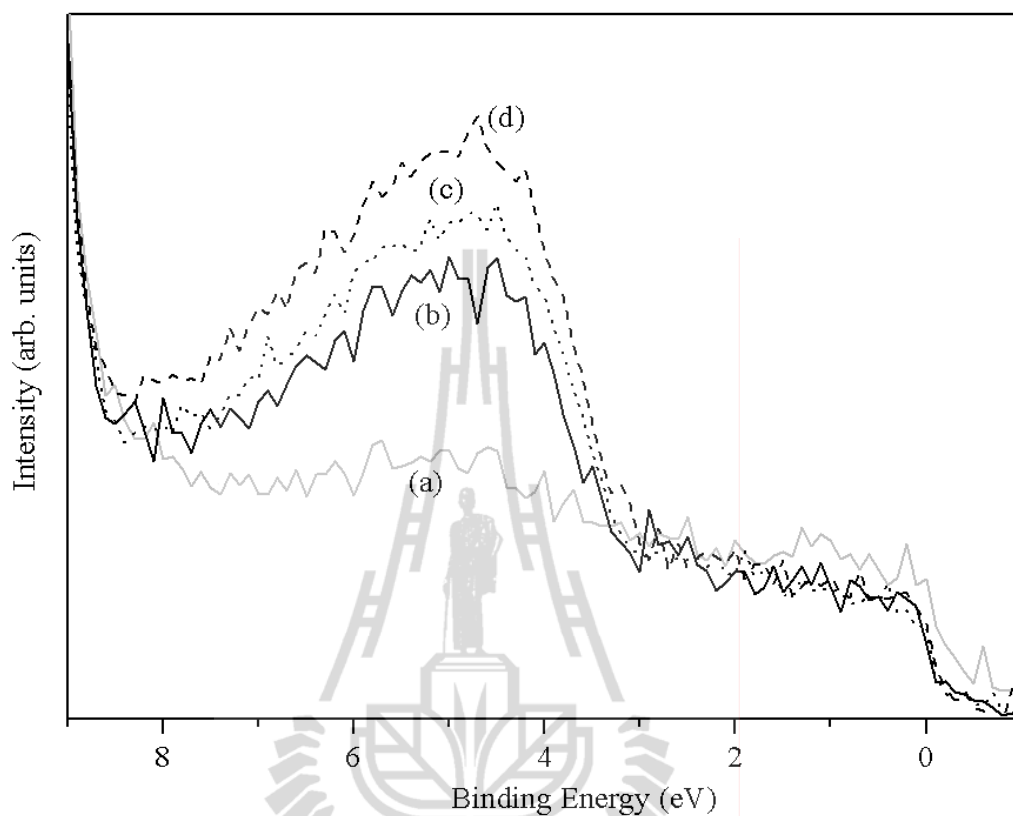


Figure 4.11 Valence band region of the PES spectra taken from a clean Zn foil before (a) and after sputtering by 3-keV Ar^+ ion in an ambient of O_2 at 5×10^{-7} Torr (b), 2 keV Ar^+ ion in an ambient of O_2 at 5×10^{-7} Torr (c), and 1 keV O^+ at pressure 1×10^{-8} Torr O_2 (d).

4.4 ZnO formed by O₂ exposure in UHV environment at room temperature

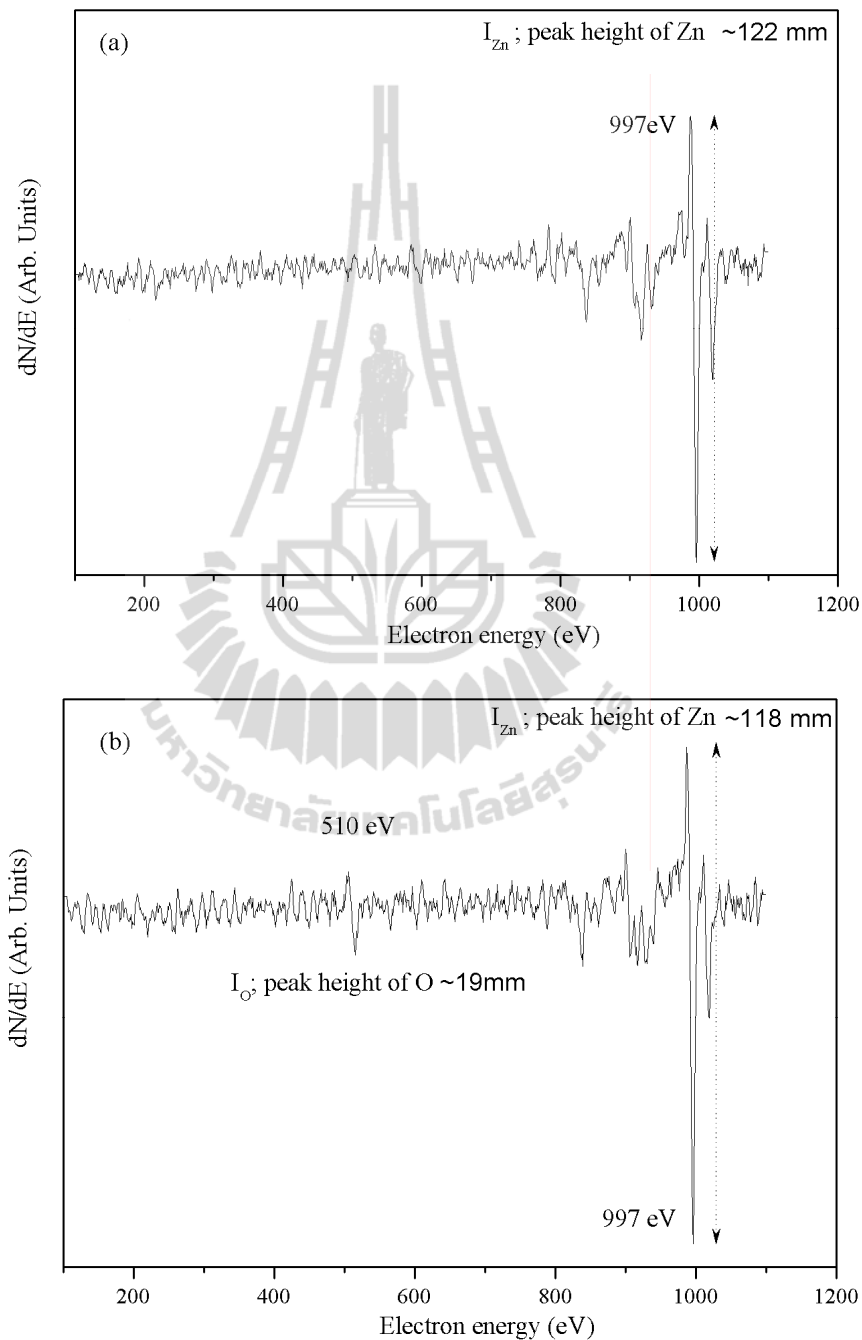


Figure 4.12 The derivative Auger spectra of a clean zinc foil before (a) and after exposure to oxygen with different time exposures varying from 5 to 15 minutes, (b) to (d).

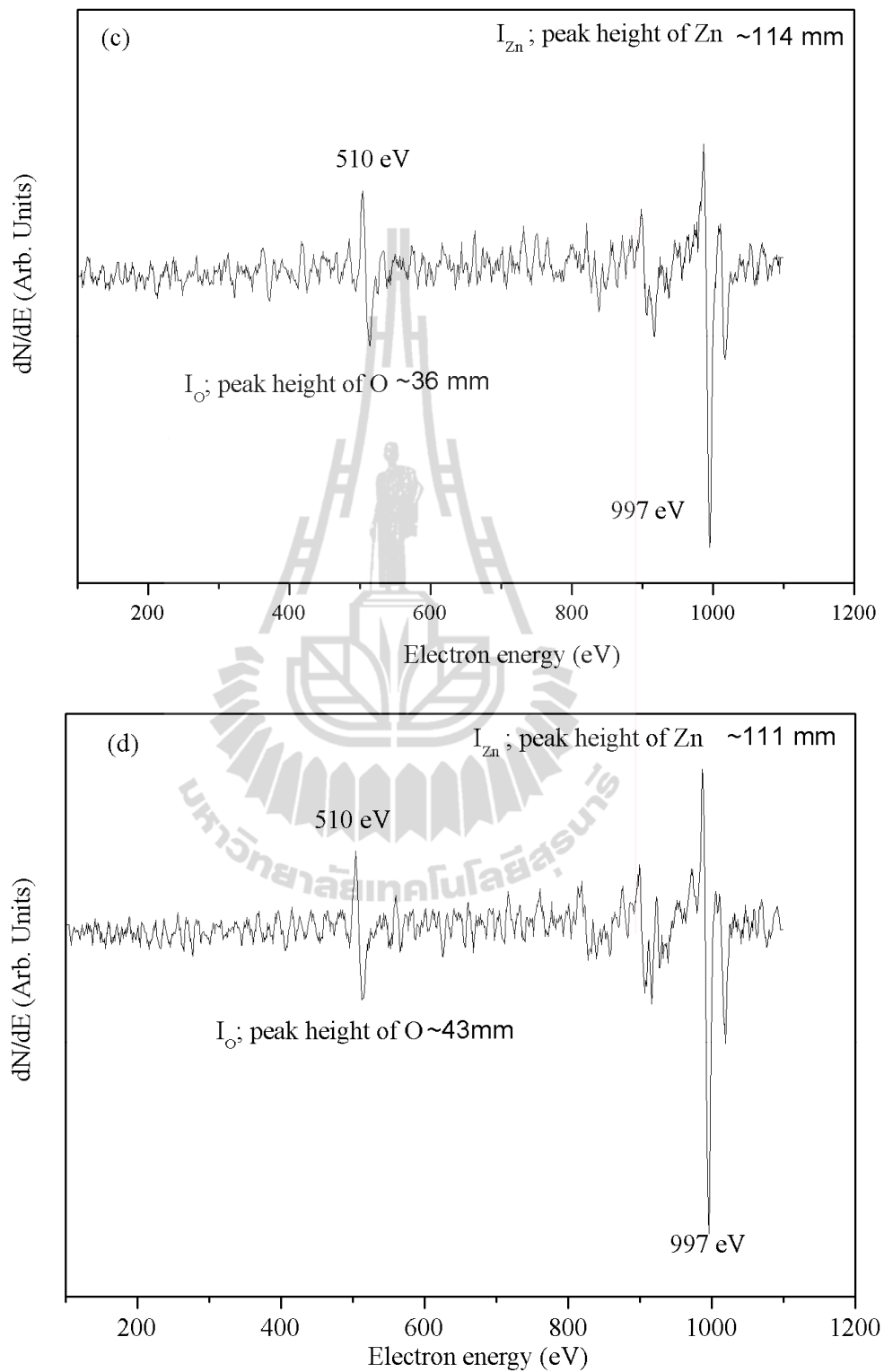


Figure 4.12 (Continued) the derivative Auger spectra of a clean zinc foil before (a) and after exposure to oxygen with different time exposures varying from 5 to 15 minutes, (b) to (d).

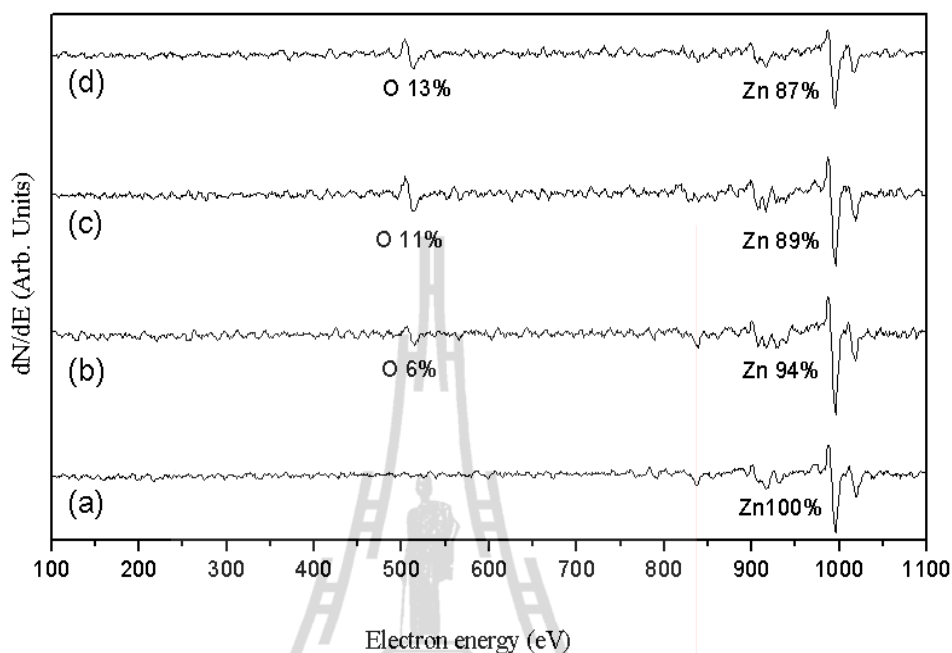


Figure 4.13 The derivative AES spectra and corresponding concentration of oxygen atom on the surface of the zinc foil; (a) clean surface, (b) after exposure to oxygen for 5 minutes, (c) for 10 minutes, and (d) for 15 minutes.

Figure 4.12 is the first derivative AES spectra taken from a clean surface of Zn foil (Figure 4.13(a)), and from the Zn foil exposed to oxygen for various times varying from 5 to 15 minutes (Figures 4.13(b) to 4.13(d), respectively.) For the clean Zn sample, only Zn Auger signals are observed in the spectrum. After exposing the clean surface of Zn foil to oxygen at room temperature at an oxygen pressure of 5×10^{-7} Torr with different exposure times, the spectra show two Auger signals, i.e., at the 510 eV (O *KLL*) and the 997 eV (Zn *LMM*). The peak to peak amplitudes of 510 eV O *KLL* Auger signals increase with increasing the exposure time, while the peak to peak amplitudes of the 997 eV Zn *LMM* decrease with increasing the exposure time. From derivative Auger spectra in samples shown in Figure 4.12, it can

be used to estimate the amount of oxygen on the surface. Concentration of oxygen atoms can be estimated from the peak intensity by using this equation.

$$C_o = [(I_o/S_o)/\{(I_o/S_o)+(I_{Zn}/S_{Zn})\}] \times 100\%, \quad (4.1)$$

where, C_o is the concentration of oxygen, I_o is the intensity of O *KLL* peak or peak to peak amplitudes, S_o is the relative sensitivity of O *KLL* at 510 eV, I_o^H and I_{Ag}^H are the peak to peak heights of oxygen and silver from the standard Auger spectra, and K_o is the relative scale factor given on the spectrum for oxygen from the standard Auger spectra. The values of S_o and S_{Zn} are 0.486 and of 0.184, respectively. I_{Zn} is measured in the derivative peak height of zinc *LMM*. According to the calculation on the concentration of oxygen atoms, it indicates that the atomic concentration of oxygen on the surface of zinc foils after exposure times for 5, 10, and 15 minutes increases from 6% to 11% and 13%, respectively, as shown in Figure 4.13(a) to (d). When the exposure times increases from 10 to 15 minutes, the amount of oxygen increases up to only a few percentages. This indicates the oxidation rate reduces at extended period of exposure time.

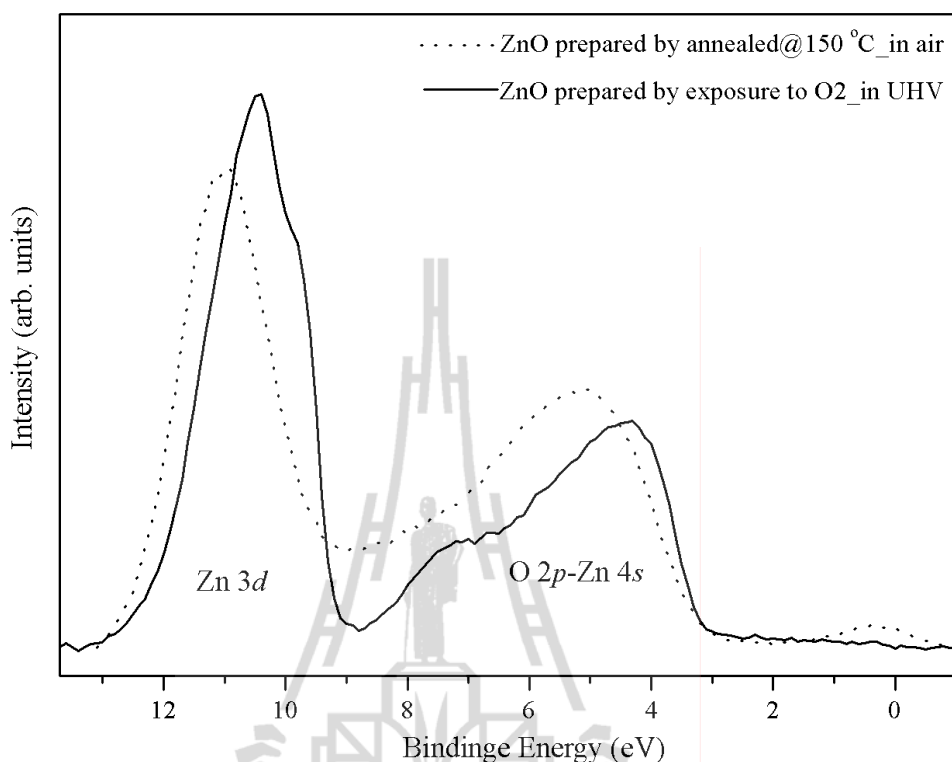


Figure 4.14 PES spectra of ZnO prepared by different methods: The dot curve is for the ZnO formed by thermal annealing at 150 °C in air for 30 minutes, the solid curve is for the ZnO prepared by oxygen exposure in UHV.

Figure 4.14 shows the spectra of ZnO samples prepared by thermal annealing at 150 °C in air for 30 minutes (dot curve) and by oxygen exposure in a UHV chamber for 45 minutes (solid curve). PES measurements were carried out at room temperature with a photon energy of 51 eV in normal emission. For the sample annealed in air, the Zn 3*d* and O 2*p* - Zn 4*s* peaks, located at about 11.0 and 5.0 eV, respectively. For the sample prepared in a UHV environment, the Zn 3*d* and O 2*p* - Zn 4*s* peaks are located at about 10.5 and 4.5 eV. This indicates the Fermi level of ZnO prepared by thermal annealing in air is located about 0.5 eV lower than that of the sample prepared by exposing a clean Zn foil to oxygen in a UHV environment.

This is caused by the differences in the doping or impurity concentration in the two samples.

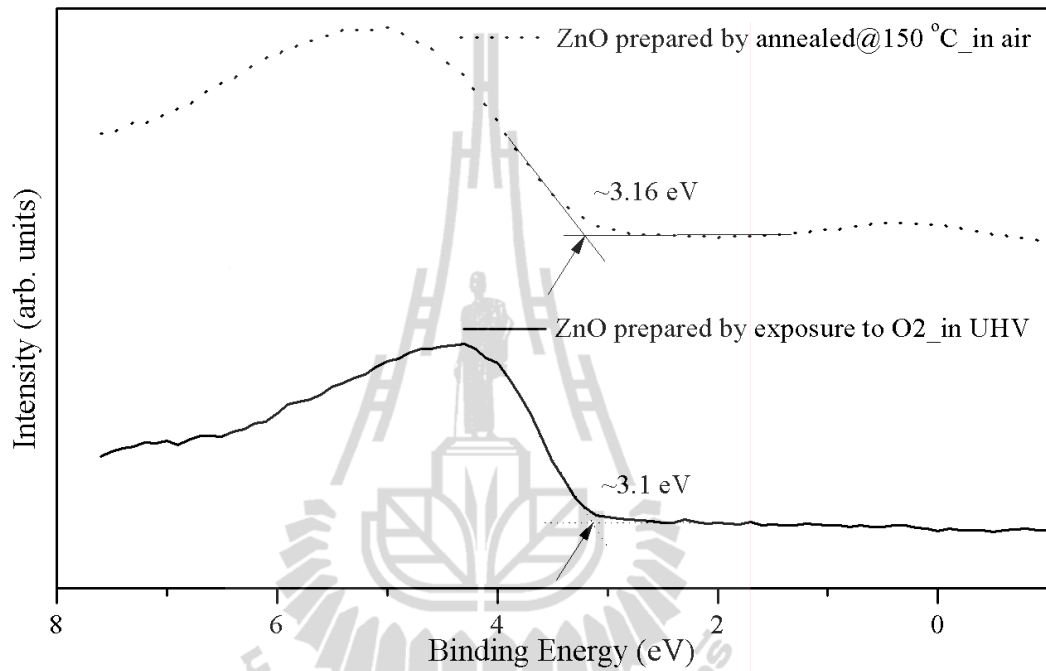


Figure 4.15 Zoomed figure 4.14 for ZnO films prepared in air and in UHV environment in the binding energy range of -1 to 8 eV.

The zoom-up of the PES in Figure 4.14 is shown in Figure 4.15 in order to illustrate how to determine the position of the valence band maximum. The valence band maximum is determined by a linear extrapolation as illustrated in Figure 4.15. The maximum valence band maximum was found to be ~ 3.16 and ~ 3.10 eV below the Fermi level ($E_F=0$) for the sample prepared by thermal annealing in air and by exposure to oxygen in UHV, respectively.

The oxidation of Zn under exposure to oxygen was studied in the ARPES system of the beamline 4 at the Siam Photon Laboratory. The experimental set-up is

shown in the Figure 3.18. The base pressure of the system is about 2×10^{-10} Torr . This UHV condition is necessary for the study of the initial state of the ZnO formation. A Zn foil was chemically cleaned before introducing into the load-lock chamber of the ARPES system. The sample then transferred and loaded to the ARPES system by the sample transfer system with breaking the UHV condition of the ARPES system. The surface of the Zn foil was further cleaned to remove surface contaminations by ion sputtering. Then, O₂ gas was let into the ARPES raising the vacuum pressure in the system from the base pressure to 5×10^{-7} Torr . The surface Zn foil was exposed to O₂ gas at room temperature for various times. After each exposure, the spectra of photoelectron spectra excited by 51 eV photons were taken at normal emission direction. Figure 4.16 shows normalized photoelectron spectra of a clean surface of zinc foils exposed to oxygen in the UHV environment at a pressure of 5×10^{-7} Torr for different exposures varying from 5 to 180 min. The top spectrum was taken from the clean Zn foil. Two peaks are found at 9.9 and 10.5 eV below the Fermi level, labeled A and B, respectively. The spectrum has almost no other feature expect a relatively much smaller shoulder near the Fermi level ($E_F=0$) which will be discussed below. Upon exposing the clean surface of zinc foils to oxygen at room temperature, difference spectra show the modification in the shape of zinc and oxygen structure at in creasing exposure times the series of the spectra clearly show the effect of oxygen exposure. The shape and magnitude of the peaks associated with Zn 3d are varied. The variation is accompanied by another change of the spectra in the valence bands region. It is obvious that oxygen induces a shift of peak B towards higher binding energy whereas the strength of peak A is reduced and a broad lump in the lower region of the binding energy (3-9 eV) appeared. In ZnO, the lump in this low

energy region has been assigned to the valence band states composed mainly of O 2*p* and Zn 4*s*. Therefore, the appearance of the lump in the valence band region indicates the incorporation of the O atoms in the form of Zn-O bonding. The overall progressive variation of the spectra with the exposure time can be viewed as the switching of Zn atom from the metal form to ZnO semiconductor. Then after exposure time is 60 to 180 minutes, it is clearly seen that there are similar curve, both of Zn 3*d* and O 2*p* curve are observed to increase slightly with the increasing exposure time. Evidence indicating that, in the case of the photoelectron peak intensity does not change or constant during the oxidation leads to a critical thickness condition. In the bottom curve is resulted from a single crystal ZnO (0001) taken at 51 eV photon energy by Guziewicz *et al.* (2005). In order to compare the measured spectra, it found that the Zn 3*d* spectrum was slightly shifted in the binding energy of about 0.3 eV, due to different Fermi levels, is applied. From figure 4.16, it is interesting to point out that the intensity of the Zn 3*d* electrons greatly reduces by more than half when the exposure time is increased from 15 to 30 minutes while there is only minimal increase of the intensity in the lower binding energy region. The explanation for the reduction of Zn 3*d* when increasing the exposure time from 15 to 30 minutes is illustrated in Figure 4.17.

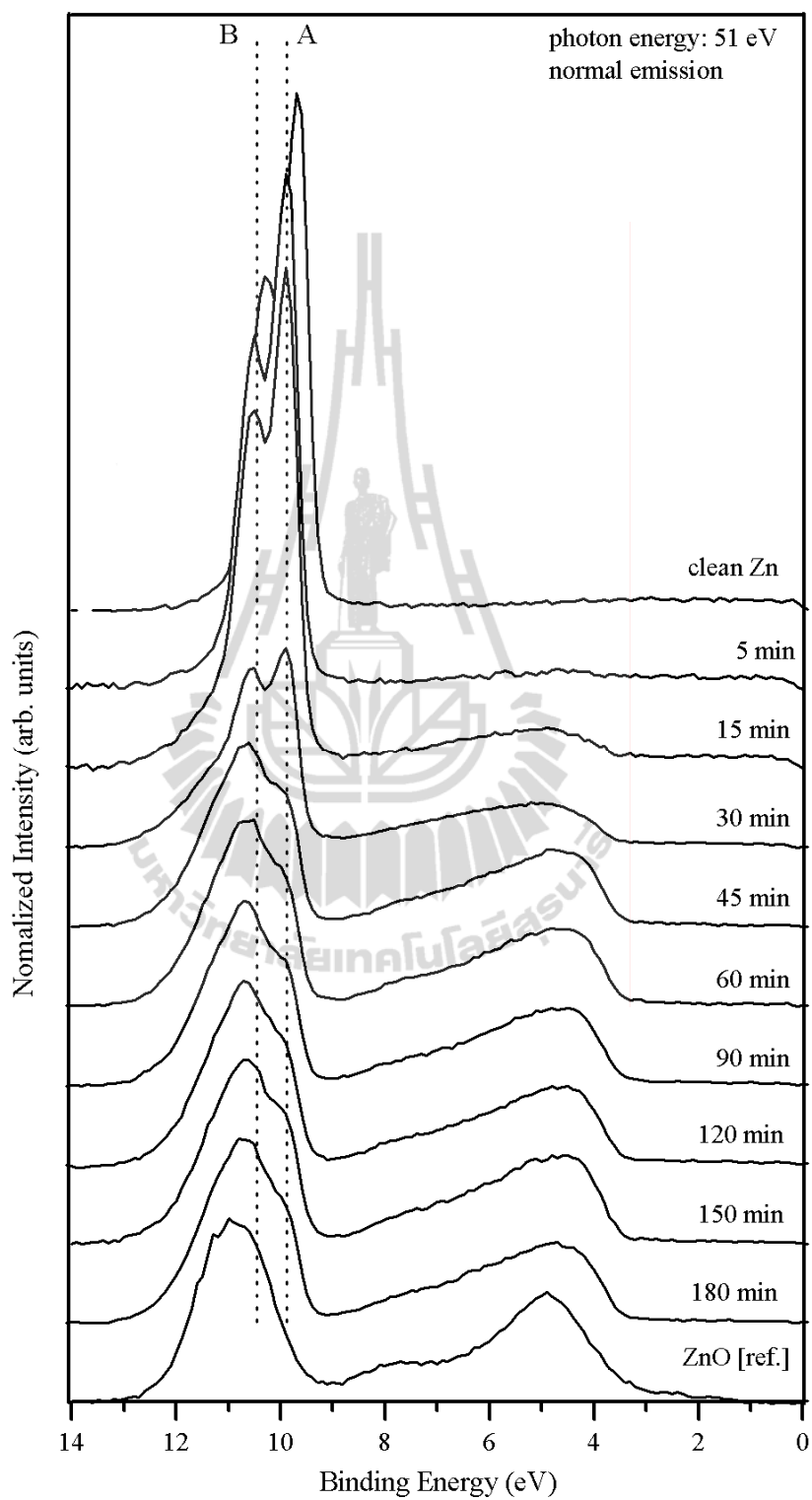


Figure 4.16 Normalized photoemission spectra of clean surface of Zn foils exposed to oxygen in UHV environment at pressure 5×10^{-7} Torr for various exposure times.

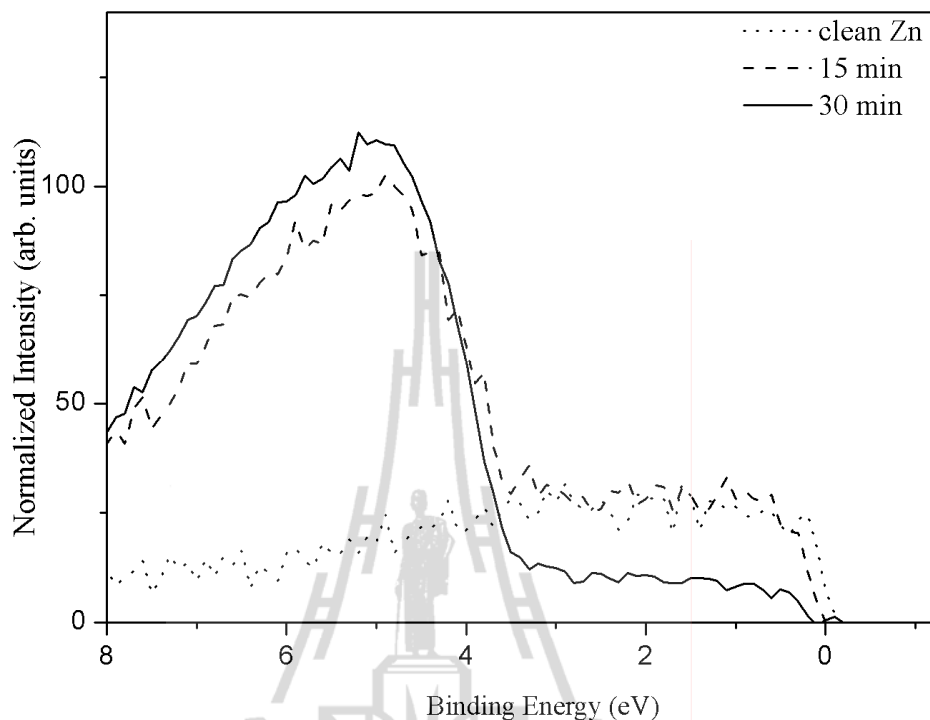


Figure 4.17 Photoelectron spectra in the valence band region for the clean Zn surfaces without and with oxygen exposure for 15 and 30 min, respectively.

Figure 4.17 shows the zoom-up photoelectron spectra observed in the valence band region in the binding energy range 0 to 8 eV below the Fermi level for the clean Zn surfaces without and with oxygen exposures for 15 and 30 minutes, respectively. For the clean Zn sample as shown in the dot curve found that the spectrum has a clear shoulder near the Fermi level which is a typical feature of metal valence electron states (Zn 4s). Consideration at the sample exposed for 15 minutes (see in dash curve) it shows that the intensity of Zn valence electrons near the Fermi level remains virtually the same as those of the clean Zn. This indicates that, in the sample exposed for 15 minutes, only a very small amount of Zn surface atoms is chemically interacted with oxygen. Majority of Zn atoms still remain in the metallic phase with oxygen covering. After increasing the exposure time to 30 minutes as shown in the solid

curve it found that the intensity of the observed Zn valence electrons near the Fermi level was reduced more than a factor of 2 indicating that interaction between the Zn atoms and O atoms are started to form the ZnO by exposure of a clean surface to oxygen. Although, some amount of Zn valence electrons was still observed, these remaining Zn 4s signals come mostly from the underlying metallic Zn as shown the schematic illustrations in the Figure 4.18.

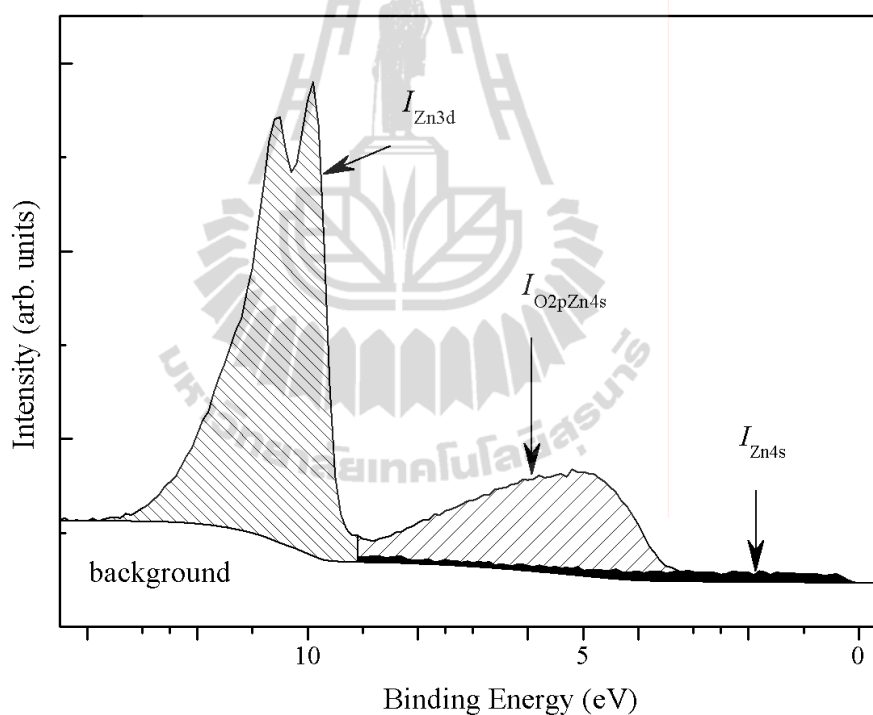


Figure 4.18 Schematic illustration showing the contributions of a photoelectron spectrum taken from a clean Zn after oxygen exposure. Three major photoelectrons are indicated by three different regions, i.e., I_{Zn3d} , $I_{O2pZn4s}$, and I_{Zn4s} .

Figure 4.18 shows Schematic illustration showing the contributions of a photoelectron spectrum taken from a clean Zn after oxygen exposure. Three major photoelectrons are indicated by three different regions, i.e., Zn 3d electrons,

O 2p - Zn 4s electrons and Zn 4s electrons. $I_{Zn\ 3d}$, $I_{O\ 2p\ Zn\ 4s}$, and $I_{Zn\ 4s}$ in the figure represent the amount or intensity of Zn 3d electrons, O 2p - Zn 4s electrons and Zn 4s electrons, respectively. Zn 3d electrons can emit from an overlayer of ZnO and from the Zn substrate. Zn 4s electrons are considered to be emitted from the under-lying Zn substrate. The intensity of Zn 4s is expected to decrease when the thickness of the oxide layer increases. Upon the oxidation, Zn 4s electron bond with O 2p electron and thus the peak area of O 2p - Zn 4s increases with increasing oxide thickness. The thickness of the oxide layer may be deduced from the photoelectron spectra as explained below.

4.4.1 Quantitative analysis of PES spectra

The peak intensity in PES spectra is proportional to the number of atoms presenting in the detected region. The peak intensity is the area under the peak after background subtraction. The Shirley method (Shirley, 1972) of background subtraction is very often employed. This Shirley method was also used in the spectral analysis in this work. It is noted that the background intensity may be considered to be photoelectrons that suffered from scattering and thus is proportional to the intensity of the emission peak. The measured intensity is directly proportional to the intensity of the primary radiation and the number of the atom. To quantify the amount of detecting atoms, the mean free path of the emitted electron (λ) and the angle of the collection of the photoelectrons relative to the surface normal must also be considered. It is therefore possible to estimate the intensity of a photoelectron of an element which coming from an oxide layer on substrate.

The signal intensity of photoelectron depends on the take off angle. By varying the collection angle θ , the sensitivity to the surface will change. At very low

take off angles ($90^\circ - \theta$), most of the collected electrons are emitted from atoms near the surface. While at higher take off angles more electrons will be collected from atoms deeper in the sample. At normal emission ($\theta = 0^\circ$), the escape depth is equal to the attenuation length λ . At other take off angles, the escape depth is $\lambda \cos \theta$, which is less than the attenuation length. In principle, PES is a surface sensitive technique with capability to investigate material from the surface to the depth about 3-5 nanometers, depending types of materials and excitation energy. Figure 4.19 shows the set up for the variation of sampling depth as a function of take off angles in photoemission experiments.

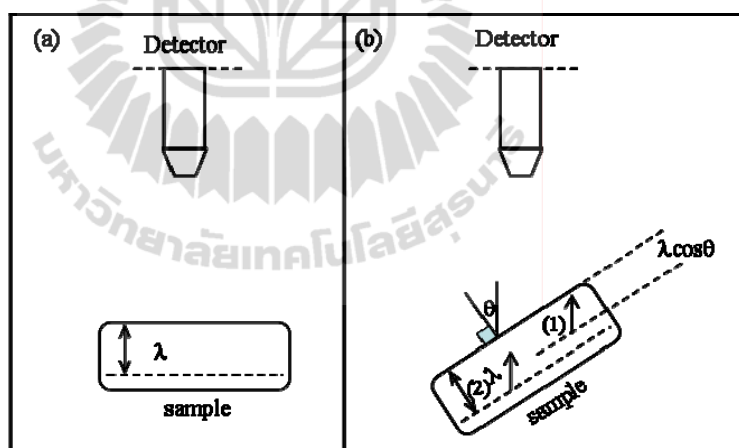


Figure 4.19 Schematic drawing showing the variation of sampling depth as a function of take off angle in photoemission experiments; (a) normal emission ($\theta = 0^\circ$) for greatest depth detection and (b) at shallow take off angles ($\theta > 0^\circ$) to increase surface sensitivity.

4.4.2 The thickness of oxide film

The thickness of very thin film of some materials can be determined from photoemission spectra. In the case of ZnO film on Zn underlying substrate studied in this work, the oxide thickness can easily be deduced from photoelectron spectra since thickness is in the same magnitude as the escape length of electrons in Zn and ZnO. As shown in Figure 4.18, the photoelectron spectrum in the valence band region of a very thin ZnO formed on Zn substrate may be considered to be compositions of Zn 3d electrons, O 2p - Zn 4s electron, Zn 4s electron and secondary electron as the background. The oxide thickness was deduced from the amount of ZnO formed on clean Zn foils.

In principle, the oxygen coverage and the amount of ZnO formed on clean Zn foils for various oxygen exposures times can be estimated from the ratio of the Zn 3d electrons emitted from ZnO and the total emitted Zn 3d electrons. Photoelectron spectra of ultra-thin films of ZnO on Zn metal are collective of photoelectrons emitting from both the oxide overlayer and the underlying Zn metal. The ratio of the intensity of Zn 3d electrons emitting from a ZnO layer ($I_{Zn\ 3d_ZnO}$) to the total intensity of Zn 3d metal ($I_{Zn\ 3d_total}$) may be estimated from the inelastic mean free path in ZnO (λ_{ZnO}) and Zn (λ_{Zn}) as shown in the equation (4.2). The mean free path of the electrons, λ , for ZnO and Zn are important parameters. The mean free path used in these work were obtained from calculations given by Seah and Dench (1979).

$$\frac{I_{Zn3d_ZnO}}{I_{Zn3d_total}} = \frac{\rho_{ZnO} \times \sum_{i=0}^n \exp((-i \times d_{ZnO}) / (\lambda_{ZnO}))}{\rho_{ZnO} \times \sum_{i=0}^n \exp((-i \times d_{ZnO}) / (\lambda_{ZnO})) + \rho_{Zn} \sum_{j=0}^{\infty} \exp((-j \times d_{Zn}) / (\lambda_{Zn}) + (-n \times d_{ZnO}) / (\lambda_{ZnO}))}, \quad (4.2)$$

where, ρ_{ZnO} and ρ_{Zn} are the densities of Zn atom in ZnO and in Zn respectively.

λ_{ZnO} and λ_{Zn} are the mean free paths, with n is monolayer,

d_{ZnO} and d_{Zn} are the d-spacing of ZnO and Zn,

$I_{\text{Zn3d}_{\text{ZnO}}}$ is intensity of Zn 3d electron emitting from a ZnO layer,

$I_{\text{Zn3d}_{\text{total}}}$ is intensity of Zn 3d electron emitting from the ZnO and the underlying Zn metal.

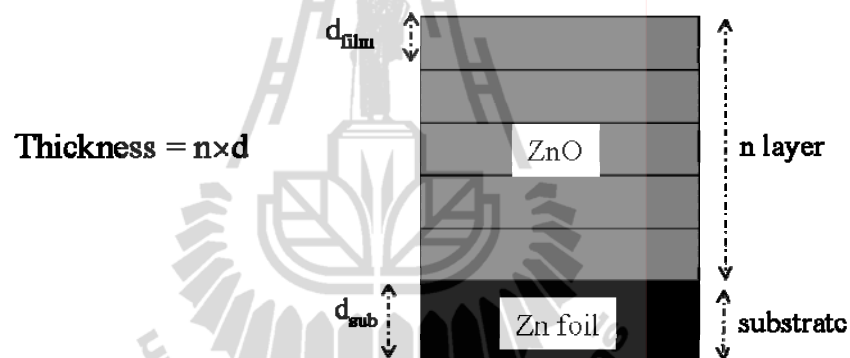


Figure 4.20 The model used in the calculations of the thickness of oxide film. The thickness of oxide surface was obtained by $n \times d$ in units of Ångstrom.

For electron with kinetic energy of about 40 eV, the electron mean free paths have been found that in oxide (ZnO) and in metal (Zn) are 4.8 Å and 4.1 Å, respectively (Seah and Dench, 1979). For simplicity, ZnO is assumed to be a single crystal with n monolayers and wurtzite ZnO with $d_{\text{ZnO}} = c/2 = 2.60$ Å. Zn is also considered to be in *hcp* structure with $d_{\text{Zn}} = 2.66$ Å. The calculated intensity ratio of the Zn 3d electron in ZnO ($I_{\text{Zn3d}_{\text{ZnO}}}$) to the total intensity of Zn 3d electrons ($I_{\text{Zn3d}_{\text{total}}}$) as a function of ZnO thickness is shown in Figure 4.21. It should be noted

that the actual Zn samples used in this work are polycrystalline Zn foils. Thus, the thickness referred in this work is an average or equivalent thickness. In the measurements, the normal emission ($\theta = 0^\circ$) spectra with respect to the surface normal were used so that the distances used in equation (4.2) is consistent with the actual path the electrons traveled. The curve in Figure 4.21 is used to convert the measured $I_{\text{Zn}3d_{\text{ZnO}}}/I_{\text{Zn}3d_{\text{total}}}$ ratio to the thickness of the ZnO layer.

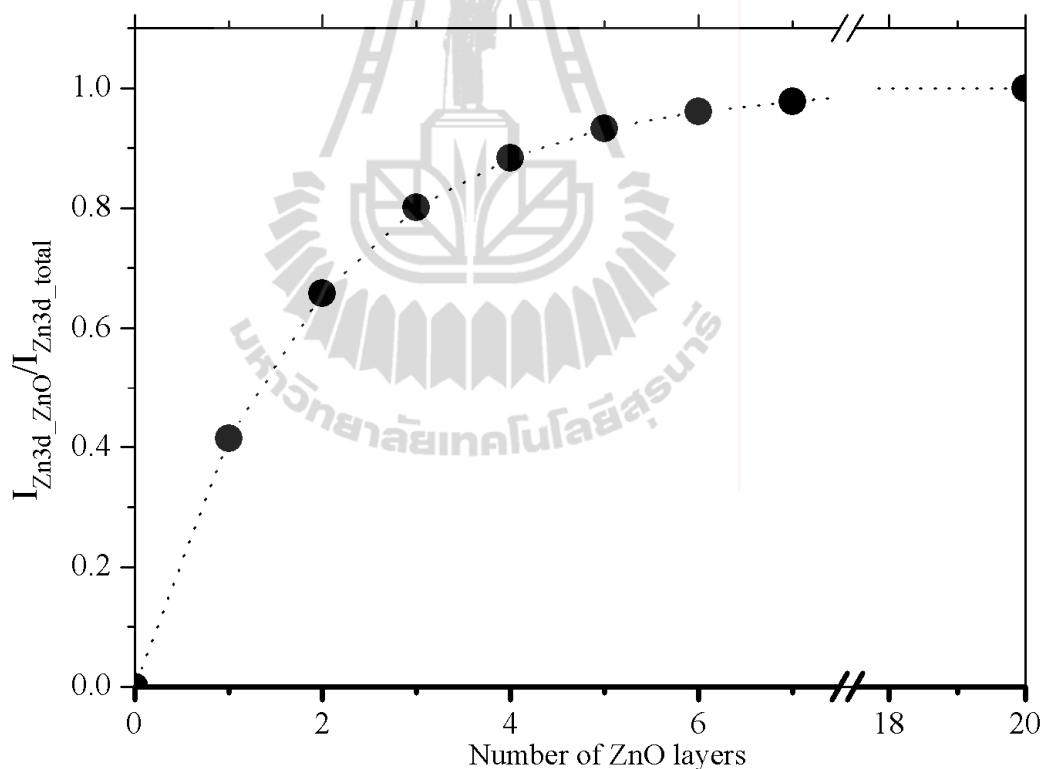


Figure 4.21 Calculated ratio of the intensity of Zn 3d photoelectrons emitted from ZnO ($I_{\text{Zn}3d_{\text{ZnO}}}$) to the intensity of all Zn 3d electrons ($I_{\text{Zn}3d_{\text{total}}}$) as a function of ZnO thickness on thick pure Zn metal.

In the previous paragraph, the method to obtain the standard curve relating the ratio of intensities (between ZnO 3d electrons to all Zn 3d electrons) to the thickness of ZnO layers was explained. In practice, the binding energy of the 3d electrons from ZnO and Zn metal are overlapped and difficult to separate. However, photoelectrons of Zn metal have a distinctive feature from those of ZnO in the region near the Fermi level (0-2.5 eV) as shown in Figure 4.17. Therefore, from the intensity of the valence electrons in the region near the Fermi level can determine the amount of intensity contributed from the underlying Zn metal. This approach should be reasonably accurate because the ZnO layers contribute only little amount of intensity in this region. The measured spectrum from the clean Zn foil sample is used to represent the spectrum of Zn metal.

Figure 4.22 shows photoelectron spectra of the samples exposed to oxygen for the exposure times from 5 to 180 minutes (solid curves). For each graph show three difference spectra. There are normalized clean Zn (dash curves), O₂ exposed Zn or the oxidized surfaces (solid curves) and difference spectrum (exposed-clean Zn) as shown in dot curves. The dash curves shown the contribution from the Zn metal underneath is determined by scaling the spectrum from the clean Zn foil to fit the region near the Fermi level. The subtracting between the solid and dash curves, the remaining spectrum (dot curve) may be considered to be the intensity of the electrons emitting from ZnO. The spectra of the clean Zn samples exposed to oxygen for 60, 90, 120, and 150 minutes are present in the Figure 4.22(e) to (h), respectively, they are shown very similar to those of the samples exposed for 45 and 180 minutes.

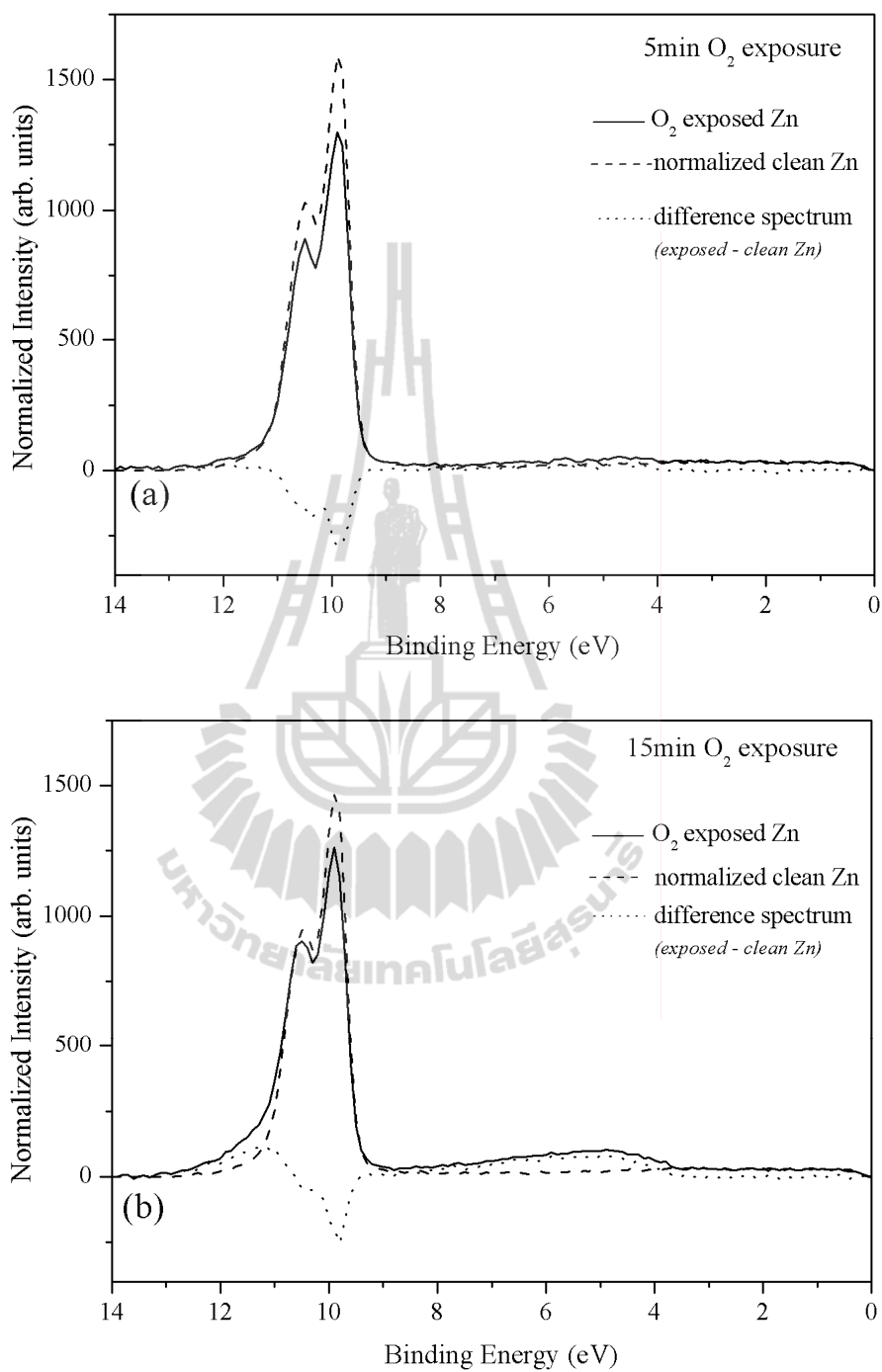


Figure 4.22 The photoelectron spectra (solid curve) of the samples exposed to oxygen for the exposure times from 5 to 180 minutes, the estimated contribution from Zn metal (dash curve), and the estimated contribution from the ZnO layer (dot curve).

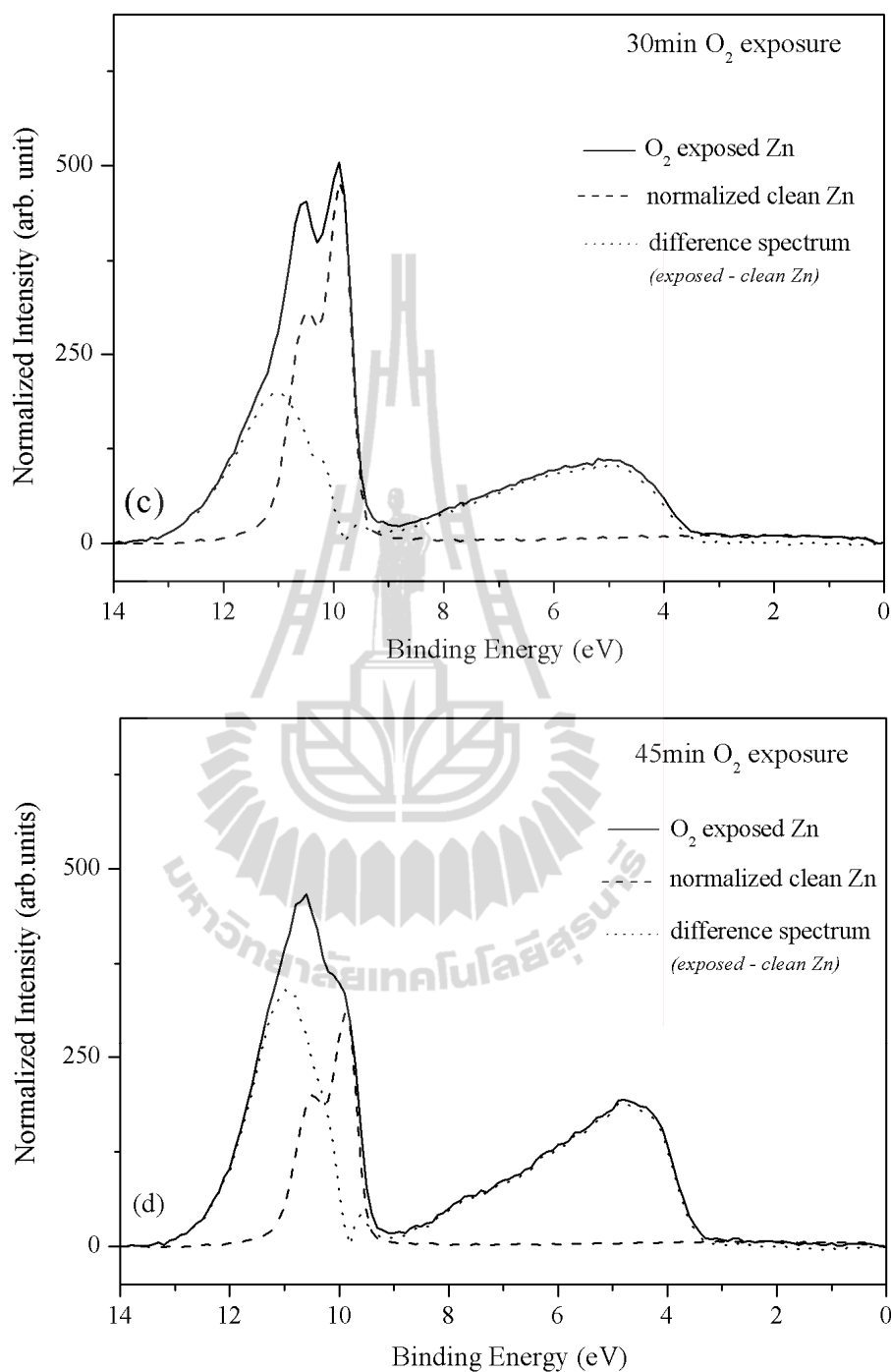


Figure 4.22 (Continued) the photoelectron spectra (solid curve) of the samples exposed to oxygen for the exposure times from 5 to 180 minutes, the estimated contribution from Zn metal (dash curve), and the estimated contribution from the ZnO layer (dot curve).

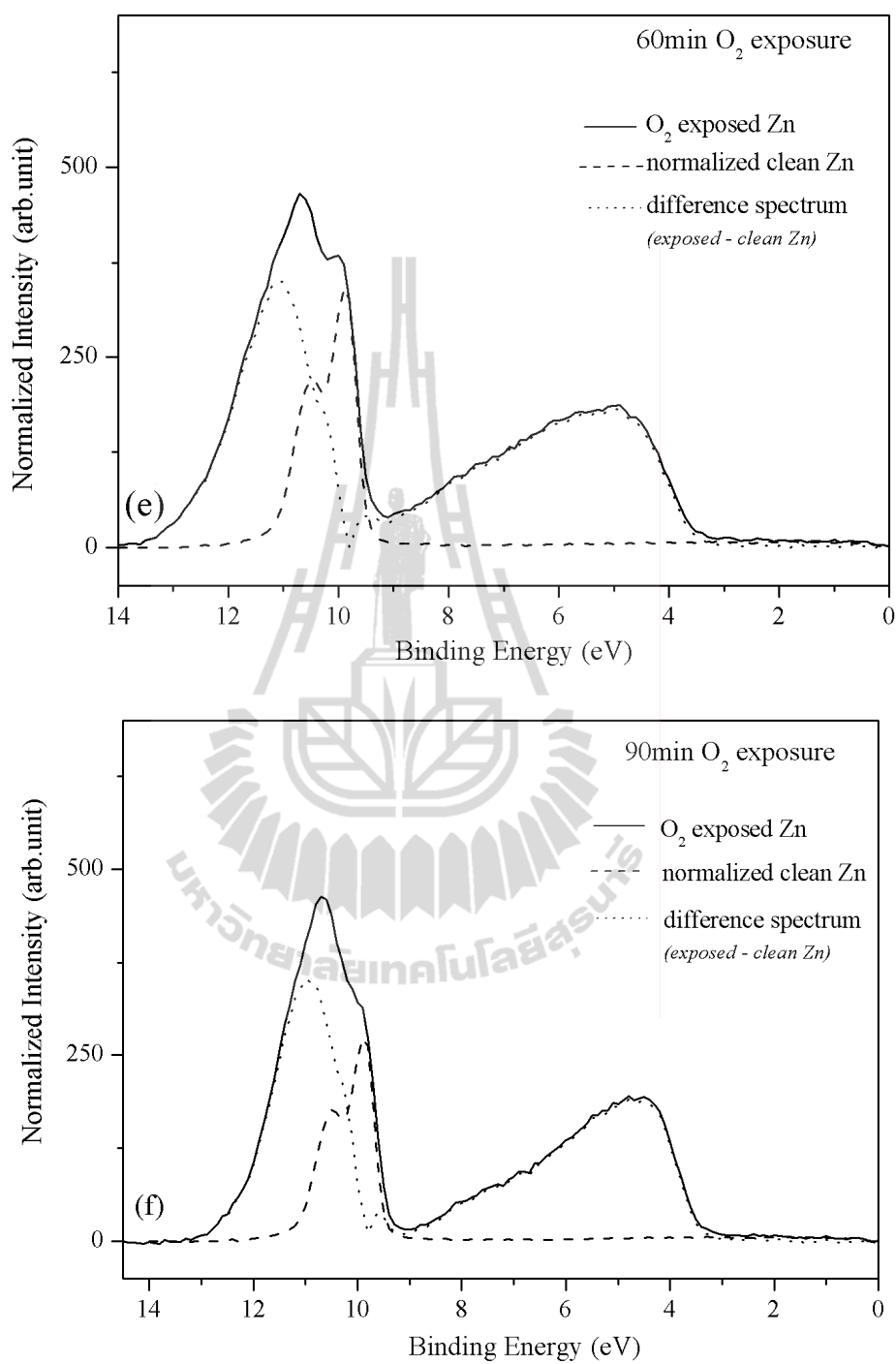


Figure 4.22 (Continued) the photoelectron spectra (solid curve) of the samples exposed to oxygen for the exposure times from 5 to 180 minutes, the estimated contribution from Zn metal (dash curve), and the estimated contribution from the ZnO layer (dot curve).

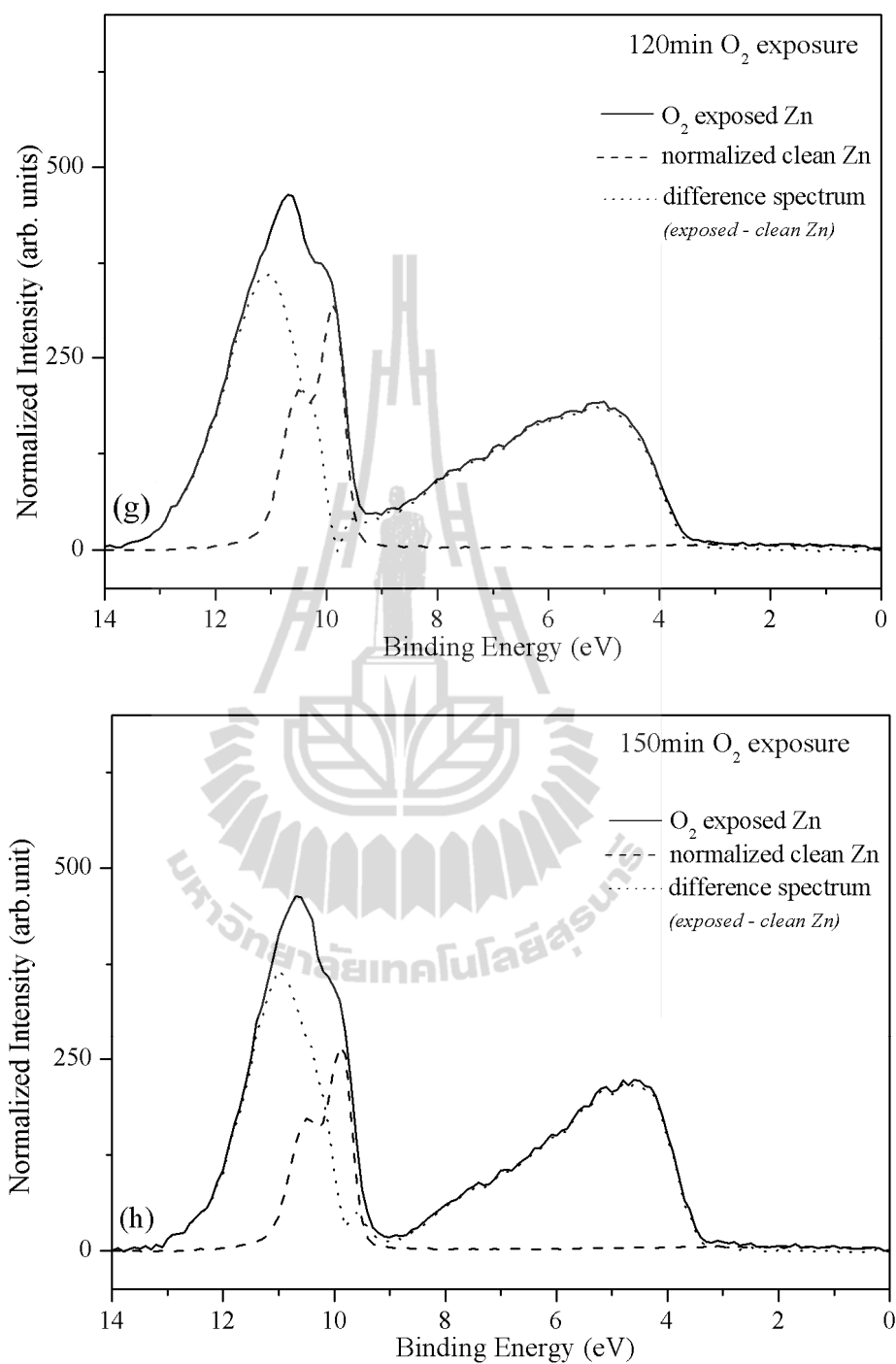


Figure 4.22 (Continued) the photoelectron spectra (solid curve) of the samples exposed to oxygen for the exposure times from 5 to 180 minutes, the estimated contribution from Zn metal (dash curve), and the estimated contribution from the ZnO layer (dot curve).

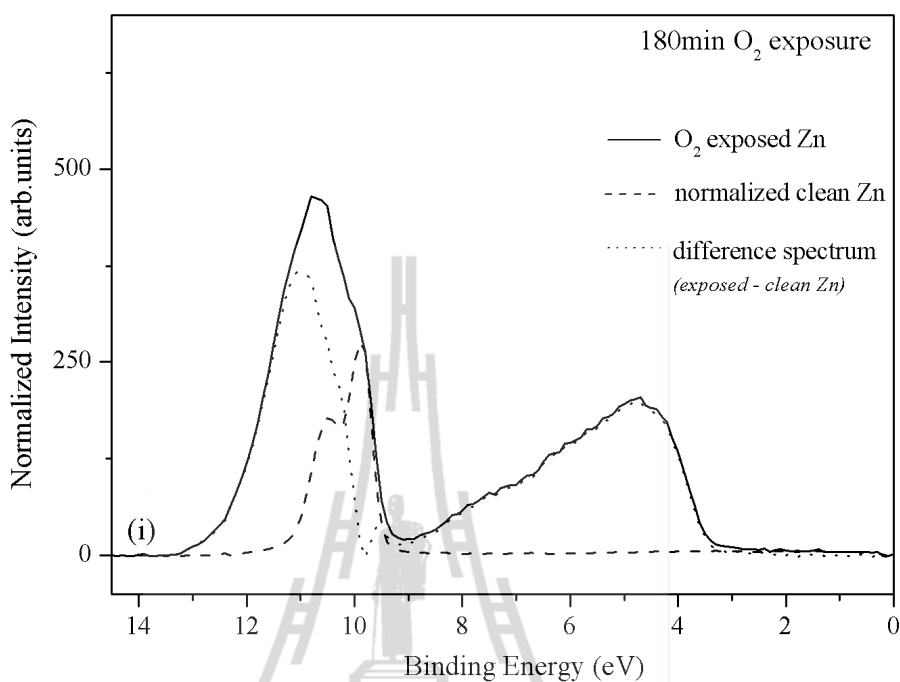


Figure 4.22 (Continued) the photoelectron spectra (solid curve) of the samples exposed to oxygen for the exposure times from 5 to 180 minutes, the estimated contribution from Zn metal (dash curve), and the estimated contribution from the ZnO layer (dot curve).

At the exposure time of 5 minutes, as shown in Figure 4.22(a), the difference spectrum (dot curve) has a small broad lump in the O $2p$ energy region and small negative intensity in the Zn $3d$ region. The intensity in the O $2p$ region indicates that there is a small amount of oxygen coverage on the sample. This small amount of oxygen, however, contributes additional electron intensity in the 0-2.5 eV region. Because the intensity in that region is used to determine the Zn metal contribution, the calculated contribution from Zn metal (dash curve) becomes slightly too big. As a result, the difference spectrum (dot curve), which should normally be the contribution from the ZnO layer, become fictitiously negative.

For the sample with 15 minutes exposure times as shown in Figure 4.22(b), found that the difference spectrum (dot curve) shows the signature chemical bonding between Zn and O atoms. There appears the intensity of Zn 3*d* electrons with energy shifted towards higher binding energy. However, the small negative is still observed for the same reason explained above. When the exposure times increases to 30 minutes as shown in the Figure 4.22(c), the difference spectrum shows higher intensity of Zn 3*d* electrons with binding energy shifted towards higher values. The spectrum now contains both the peak in the Zn 3*d* region and the lump in the lower energy region. It clearly represents the electrons emitting from ZnO. Consideration at the exposure times for 45 minutes of oxygen exposure found that the intensity of the difference spectrum increases indication the increasing amount of ZnO formed on the metallic Zn. If consideration at the exposure times increases from 45 to 180 minutes (see in the Figure 4.22(d) and (i)) found that peak intensity of ZnO only increases very slightly. This indicates that the saturation of the ZnO layer formation.

To get a clearer picture of ZnO formation rate, the intensity ratio of the Zn 3*d* electrons from ZnO to the total Zn 3*d* electrons is calculated. To be specific, the area under the dot curve (in the binding energy range of 9-13 eV) is used for $I_{\text{Zn } 3d_{\text{ZnO}}}$ and the area under the solid curve is used for $I_{\text{Zn } 3d_{\text{total}}}$. After the ratio is obtained, the average thickness of ZnO layer can be read from the reference curve in Figure 4.21.

The average thickness of ZnO formed on the surface of clean Zn foils as a function of O₂ exposure time is shown in Figure 4.23. The average oxide thickness increases linearly with increasing the exposure time or oxygen dose from 5 to 45 minutes at pressures 5×10^{-7} Torr, until the thickness reaches ~2 monolayers (or ~5Å) of ZnO. After the exposure time is increased from 45 to 180 minutes found

that the growth rate was kept constant at ~ 2 monolayers. It indicates that at this critical thickness the growth rate of ZnO reduces to nearly zero. It is interesting to point out that when the exposure time was 30 minutes, the Zn 4s electrons chemically interact with O 2p to produce ZnO with an average coverage of ~ 1 monolayer (or $\sim 3\text{\AA}$), resulting in the reduction of the Zn 4s electrons near the Fermi edge as shown in Figure 4.17. This indicates that the metallic phase of Zn surface has changed to the semiconductor phase.

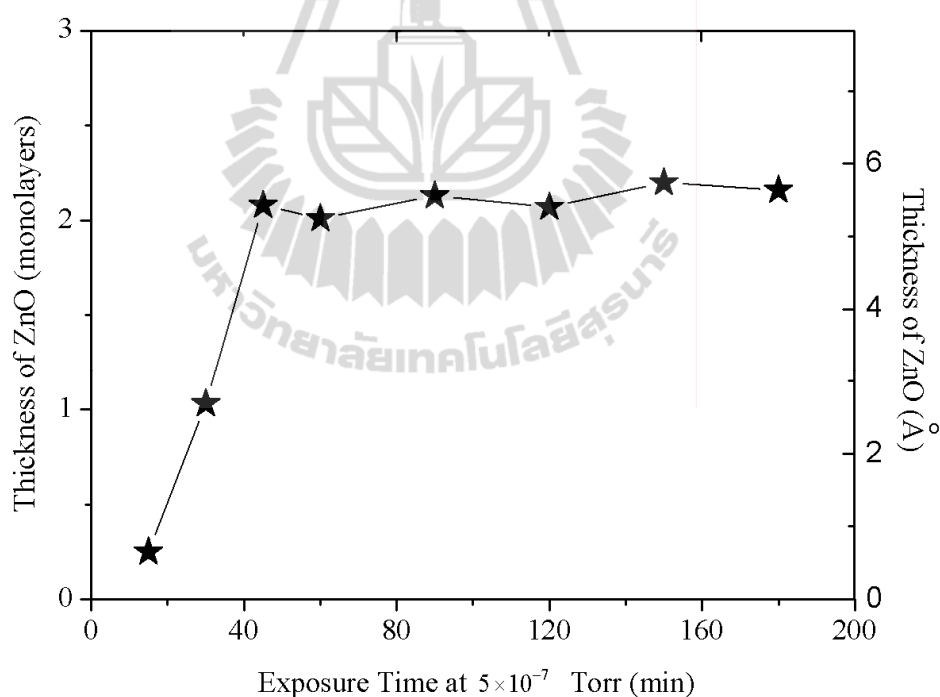


Figure 4.23 The average thickness of ZnO formed on a clean Zn surface as a function of oxygen exposure time.

4.5 ZnO formed by O₂ exposure in UHV environment at elevated temperatures

This part of the thesis work was performed at the photoemission spectroscopy (PES) beamline, BL3.2a, of the Synchrotron Light Research Institute of Thailand. The PES system is equipped with a Thermo VG Scientific CLAM2 electron spectrometer. Zn foils with 99.99% purity and 0.05 mm thick were used in this work. The Zn foils were cleaned with alcohol and de-ionized water, respectively, in an ultrasonic bath before loading into the PES system. To obtain a good reference photoelectron spectrum of a clean Zn surface, the measurements were performed at the base pressure of $\sim 2 \times 10^{-10}$ Torr. Thus one of the samples was introduced into the analysis chamber through a load-lock system to prevent breaking of the UHV condition. The clean surface was obtained by 0.5 keV Ar⁺ ion sputtering in the analysis chamber.

Oxidation of Zn was done by exposure of the Zn foils with a “pre-oxidized overlayer” to oxygen in the analysis chamber of the PES system. In order to assure good contact between the thermocouple and the samples to obtain a reliable oxidation temperature, a chemically cleaned Zn foil was mounted on the sample holder in air and thus the breaking the UHV condition of the PES system was necessary. After that, baking-out the PES system was carried out at 130 °C for 24 hours. The unavoidable oxide layer which formed on the Zn sample during baking was later removed by Ar⁺ ion sputtering. The base pressure of the analysis chamber for the measurements of the oxidized sample was $\sim 3 \times 10^{-9}$ Torr. Oxidation of the Zn foil was performed at room temperature, 50 °C, 70 °C, 90 °C, and 110 °C. Oxygen gas was let into the analysis chamber of the PES system to increase the vacuum pressure from the base pressure to

5×10^{-7} Torr. The exposure time was varied from 5 to 90 minutes. The thickness of the oxide layer was measured *in-situ* by the PES technique using synchrotron light with photon energy of 57 eV from the beamline BL3.2a. Photoelectrons were detected at an emission angle of 50° with respect to the surface normal. After the sample was analyzed, the oxide layer was removed by Ar^+ sputtering to provide a fresh surface of Zn, or a “pre-oxidized sample”, for new oxidation.

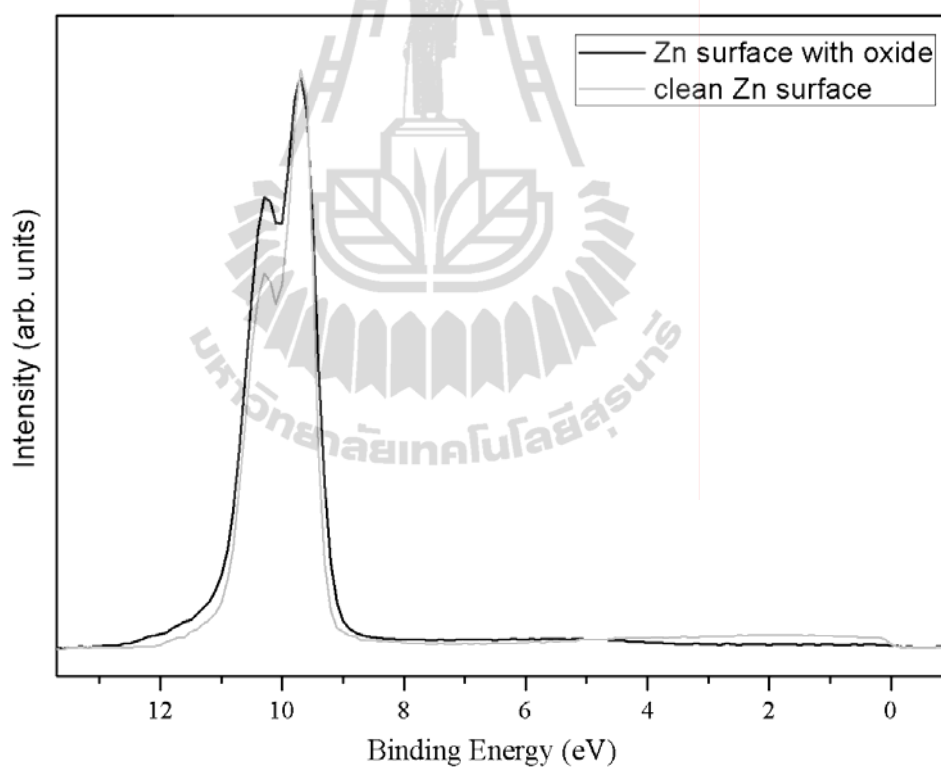


Figure 4.24 Photoelectron spectra of a clean Zn surface and a Zn surface with a pre-oxidized layer.

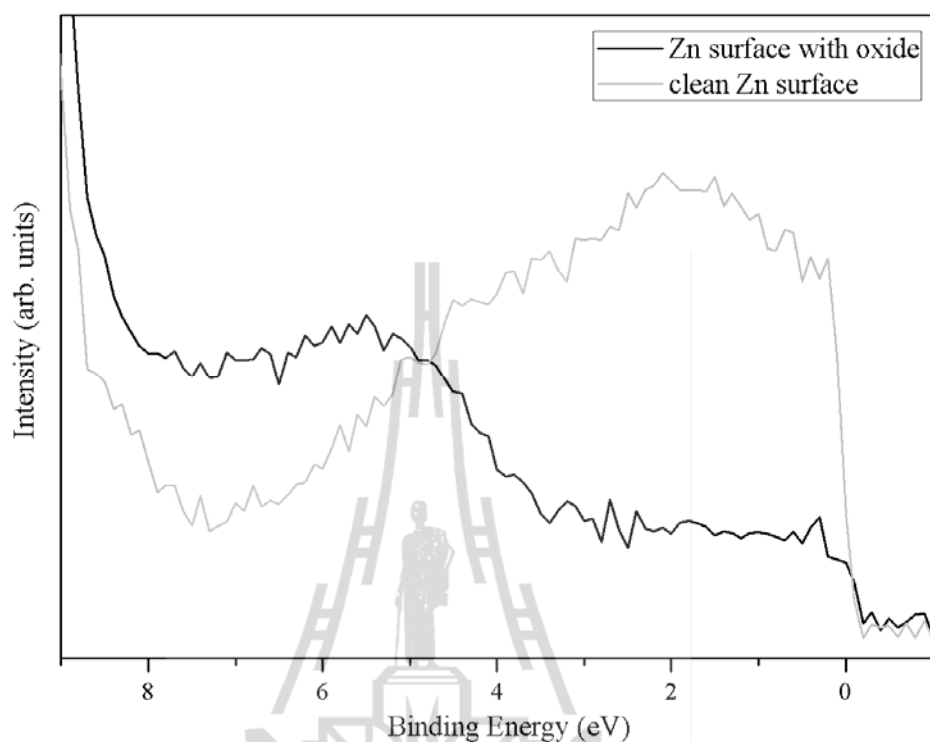


Figure 4.25 Photoelectron spectra showing the intensities of the photoelectrons near the Fermi level associated with Zn 4s and Zn 4s - O 2p (zoom-up of figure 4.24).

Figure 4.24 shows the photoelectron spectra obtained from two Zn samples prepared under two different conditions, referred to as a “clean sample” and a “pre-oxidized sample”. The “clean sample” refers to the Zn sample that was chemically cleaned *ex situ*, loaded into the analysis chamber through the load-lock system and sputtered by 0.5 keV Ar⁺ ions to remove surface contaminations. The measurement of the photoelectron spectrum of the clean sample was performed at vacuum pressure of $\sim 2 \times 10^{-10}$ Torr. The spectrum of this clean metallic Zn sample shows the density of state (DOS) of valence electrons. The two overlapping peaks at 9.9 eV and 10.5 eV covering the energy region from 9.3 eV to 11.3 eV are associated with Zn 3d electrons. Zn 4s electrons are also observed in the valence band up to the Fermi level.

The photoelectron spectrum of the “pre-oxidized sample” is a typical spectrum obtained from the Zn sample originally covered by the thermally-grown ZnO layer and later cleaned by successive 3.0 keV and 0.5 keV Ar⁺ ion sputtering. The photoelectron spectrum of the pre-oxidized sample deviates from that of the clean sample, indicating different surface compositions as shown in Figure 4.25. The reduction of DOS near the Fermi level and the increase of DOS in the region between ~4 eV and 9 eV results from the hybridization of Zn 4*s* electrons and O 2*p* electrons to form ZnO. The formation of ZnO also gives rise to the high binding-energy shift of Zn 3*d* electrons. The amount of the ZnO coverage for the pre-oxidized sample was estimated to be ~1.2 monolayers. Thus, it should be noted that the surface of the sample before exposing to oxygen was already covered by a thin oxide layer.

Figure 4.26 shows the normalized photoelectron spectra of the pre-oxidized Zn sample before and after exposing to oxygen at 5×10^{-7} Torr for various exposure times at the sample temperature of 50 °C. The effect of oxygen exposure can clearly be observed from a series of the spectra in Figure 4.26. There are the variations of the shape and magnitude of the peaks associated with Zn 3*d* and of the valence band spectra below ~9 eV binding energy. With an increasing exposure time, there are the high binding-energy shifts together with the decrease in magnitude of the 10.5 and 9.9 eV Zn 3*d* associated peaks, respectively. In addition, there are the increase of a broad lump in the 3 eV to 9 eV binding energy region and the reduction of the Zn 4*s* DOS near the Fermi level. Those changes indicate that metallic Zn atoms react with oxygen and transform to ZnO upon oxygen exposure.

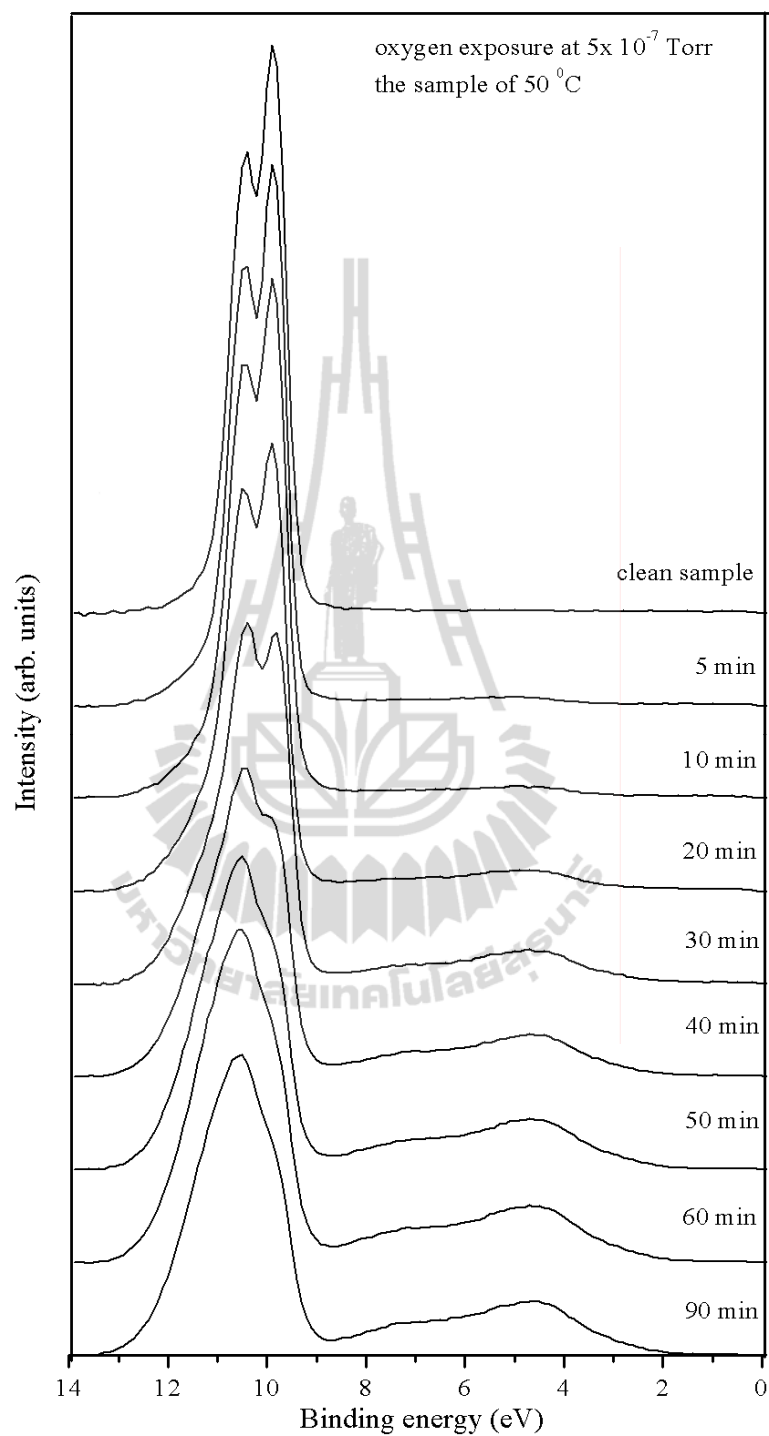


Figure 4.26 Photoelectron spectra taken from a Zn foil before and after exposed to oxygen at pressures 5×10^{-7} Torr at the sample temperature of 50°C for various exposure times.

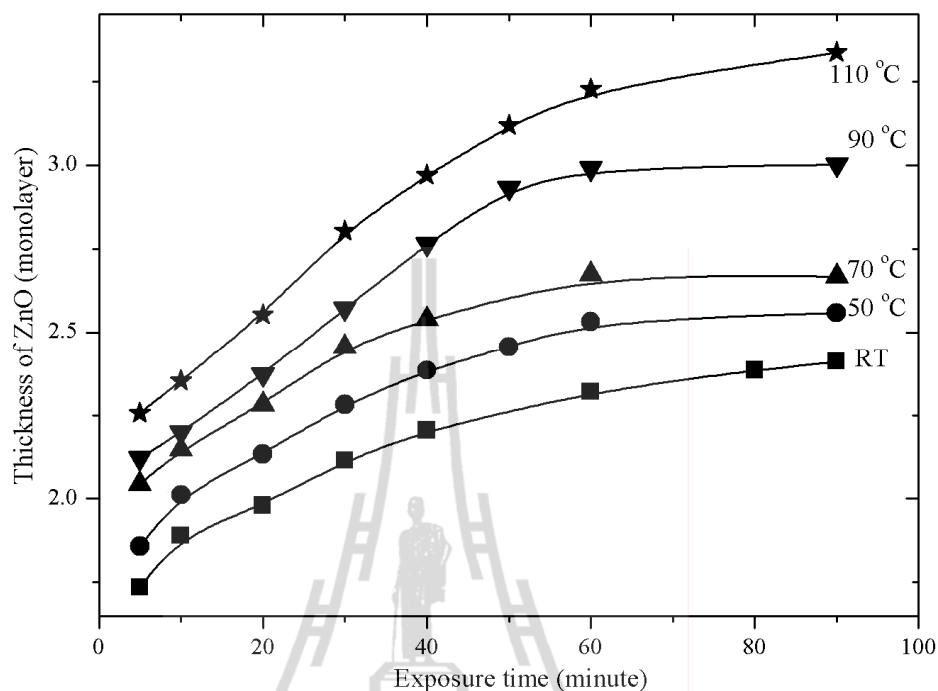


Figure 4.27 Thickness of the ZnO overlayer after exposing a Zn foil to oxygen at pressures 5×10^{-7} Torr for various exposure times.

Figure 4.27 shows the amount, or equivalent thickness, of ZnO formed on the Zn foil for various oxygen exposures and different sample temperatures that was estimated from the ratio of the Zn 3d electrons emitted from ZnO and the total emitted Zn 3d electrons. The detailed description of the calculations was reported elsewhere (Noothongkaew *et al.*, 2009). The calculation is based on the fact that a photoelectron spectrum of ultra-thin films of ZnO on Zn metal is collective of photoelectrons emitting from both the oxide overlayer and the underlying Zn metal. From the inelastic mean free path of an electron in ZnO and Zn, one can estimate the ratio of the intensity of Zn 3d electrons emitting from a ZnO layer to the total intensity of a Zn 3d electron emitting from the ZnO with a given thickness and the underlying Zn metal. At oxidation temperatures below 110 °C, the thickness of ZnO increases

quickly with the exposure time in the beginning and trends to saturate after a certain amount of ZnO has formed. At room temperature, the oxide thickness trends to saturate at ~ 2.4 monolayers, which is close to the thickness of ~ 2.2 monolayers of the ZnO formed from a clean Zn surface without the pre-oxide overlayer reported in the previous section. The saturated thickness appears to increase with the oxidation temperature. The results of this work were found to be consistent with the theory of the oxidation of metals, which was reported by Cabrera and Mott (1949). They found that several metals show very similar behaviour. Upon exposure of metal surface to oxygen at a sufficiently low temperature, the oxidation rate was initially extremely rapid. Subsequently, after a few minutes or hours, the oxidation rate decreases to very low or negligible values.

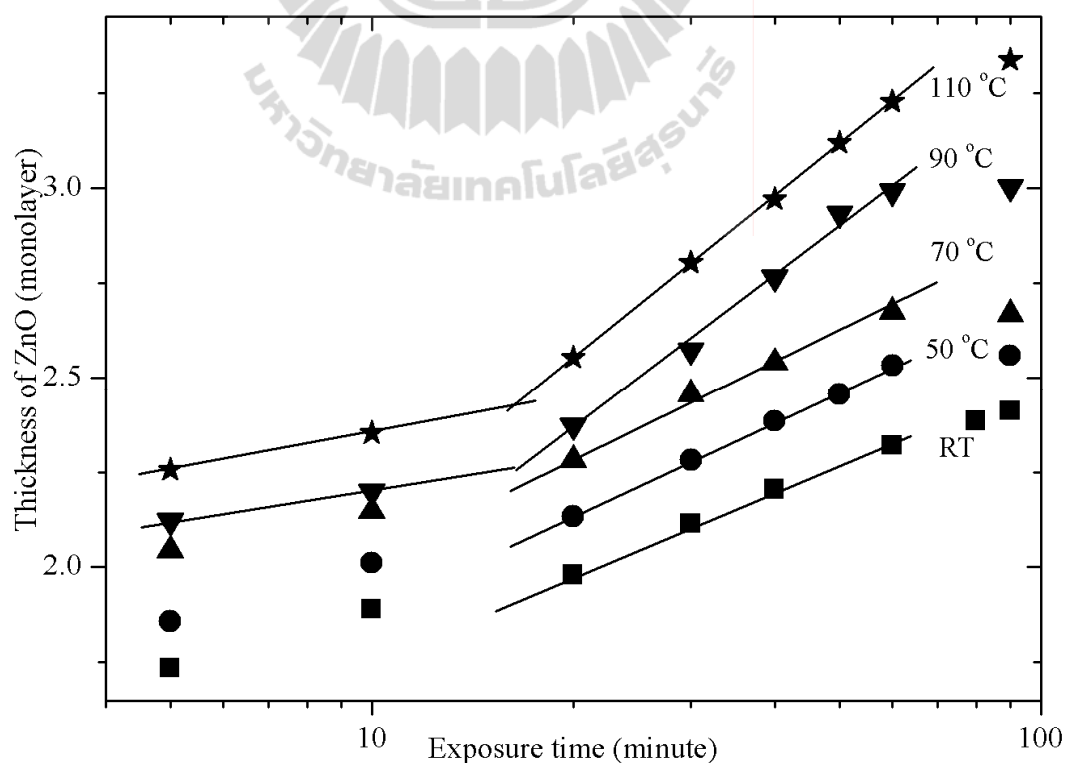


Figure 4.28 Thickness of the ZnO overlayer after exposing a Zn foil to oxygen at 5×10^{-7} Torr for various time plotted with logarithm of time.

Figure 4.28 shows the ZnO thickness plotted with the logarithm of time. Below the saturated thickness, the oxidation rate conforms to a two-stage logarithmic equation. For the oxidation at 90 °C and above, the oxidation rate for the second stage is much higher than that for the first stage. For lower oxidation temperatures, this rate decreases. The results show that oxidation of Zn at very low partial pressure and at low temperature still has a similar two-stage logarithmic oxidation behavior as oxidation of Zn and other metals at the atmospheric pressure, as reported by Vernon *et al.* (1939) and Uhlig (1956). This implies that the initial oxidation of Zn at very low partial pressure and at low temperature may be explained with a similar assumption that the oxidation process is governed by two kinds of space charge presumably formed in the thin oxide overlayer. This explanation is normally used for the oxidation of metals at the atmospheric pressure

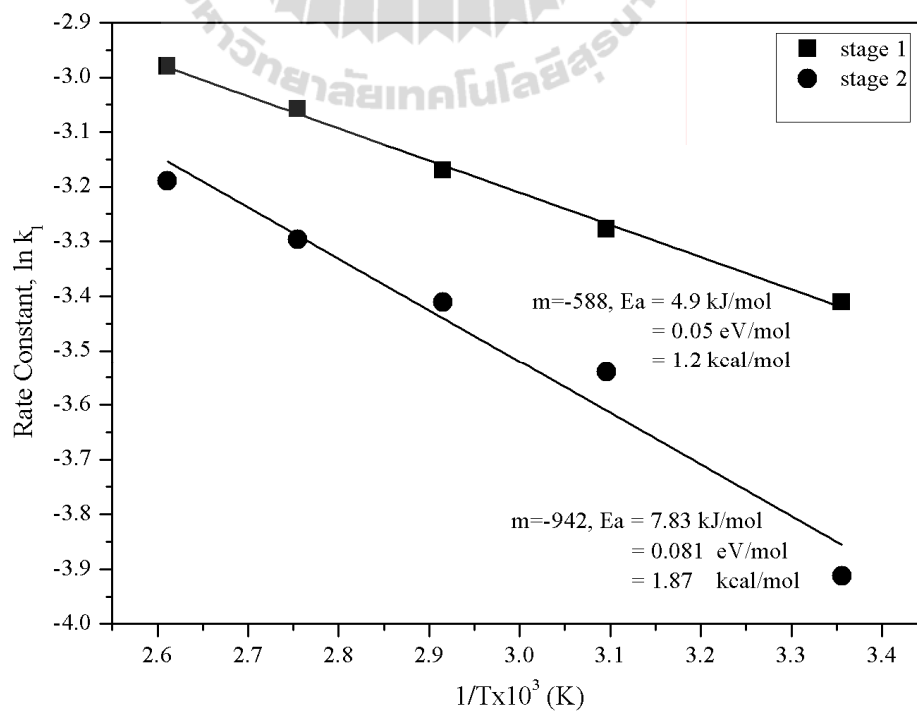


Figure 4.29 The oxidation rate constant of Zn in O₂ as a function of the inverse of the temperature (K).

The kinetics of the oxidation is governed by the activation energy, which is the energy equivalent to the energy necessary for the transfer of an electron from metal to oxide to oxygen adsorbed on the oxide. Figure 4.29 shows relation between the oxidation rate constant as a function of the inverse of oxidation temperature. The activation energy for oxidation of zinc at low partial pressure and low temperature can be estimated to follow the Arrhenius equation (Arrhenius, 1889; Rackauskas *et al.*, 2009),

$$k_l = Ce^{-E_a/RT}, \quad (4.3)$$

by rearranging this equation, it can be given as,

$$\ln k_l = -\frac{E_a}{R} \left[\frac{1}{T} \right] + \ln C \quad (4.4)$$

This equation is in form; $y = mA + B$, where $\ln k_l$ is the oxidation rate constant, E_a is the activation energy of a reaction, R is a constant equal to 8.314 J/mol-K. $1/T$ is the inverse of the temperature (kelvin, K), and $k_l = dx/dt$, x is thickness of oxide film in Angstrom units, t is the oxidation time in minutes. Thus, E_a ($E_a = -mR$) is determined from the slope of the fitted linear function between $\ln k_l$ and $1/T(K)$, as shown in Figure 4.29. The results obtained from the figure show that the oxidation rate constant (k_l) decreased linearly with the inverse of the temperature (K) and the E_a at the first and second stage are 0.05 and 0.081 eV/mol, respectively. These values are comparable to the energy reported in a previous study of ZnO nanowire arrays as the temperature was varied from 4.5 to 300 K (Lori *et al.*, 2003). They found that the activation energy $E_a = 0.071$ eV/mol. Vincent and Uhlig (1965) also reported that the activation energy for first and second stage oxidation rate of ZnO at O_2 pressure in the

temperatures range 125 °C-206 °C are 0.34 and 0.35 eV/mol. To my knowledge, there were a few studies on the kinetics of the oxidation of Zn at low temperature while there are many reports on the oxidation of Zn at high process temperature. At high temperature, the activation energy for the oxidation of Zn was reported by many groups. The reported values of E_a are 1.8 eV/mol at the temperatures between 756 °C-1267 °C (Bernhardt and Harry, 1994), 3.86 eV/mol at temperatures between 850 °C-1020 °C (Gregory *et al.*, 2000), $E_a=0.87$ eV/mol at the temperatures between 400 °C-530 °C (Rackauskas *et al.*, 2009), and 2.43 eV/mol at the temperatures between 785 °C and 820 °C (Yang and Yang, 2010). It is noted that there is a big discrepancy in the experimental values, probably due to the variations in the experimental conditions.



CHAPTER V

CONCLUSIONS

In this thesis work, the oxidation of Zn foils was systematically investigated using *in situ* electron spectroscopic techniques, namely synchrotron photoemission spectroscopy and Auger electron spectroscopy. This thesis focuses on the formation of very thin oxide layers by exposing clean Zn surface to oxygen in a UHV condition at temperatures between room temperature and 110 °C. The oxidation of Zn by thermal annealing in air was also examined for comparison. In addition, oxidation induced by ion-beam bombardment was also observed in this work.

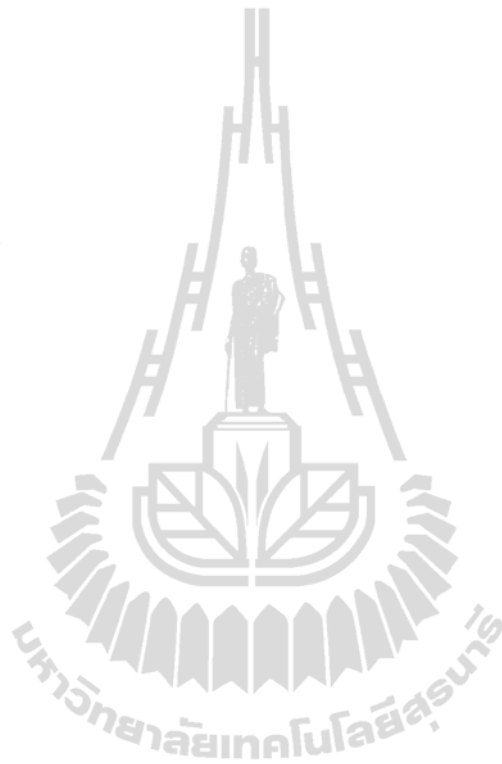
Polycrystalline Zn foils were used as the substrates. The foils were chemically clean and brought into the preparation of the photoemission spectroscopy. Ar⁺ ion sputtering technique was used to remove surface contaminations. Surface contaminations were kept below the detection limit of Auger electron spectroscopy. The samples with clean surface were exposed to O₂ at pressure of 5×10^{-7} Torr at various temperatures, i.e., room temperature, 50, 70, 90, and 110 °C for different durations. Photoelectron spectra were taken to follow the oxidation process before and after the exposure to O₂. It was found that the density of state of the valence band of the progressively changes with the oxygen exposure time. Upon exposing the clean surface of zinc foils to oxygen, the photoelectron spectra show the modification in the shape and magnitude of density of states associated with Zn 3*d* and O 2*p* - Zn 4*s* at increasing exposure times the series of the spectra clearly showing the effect of

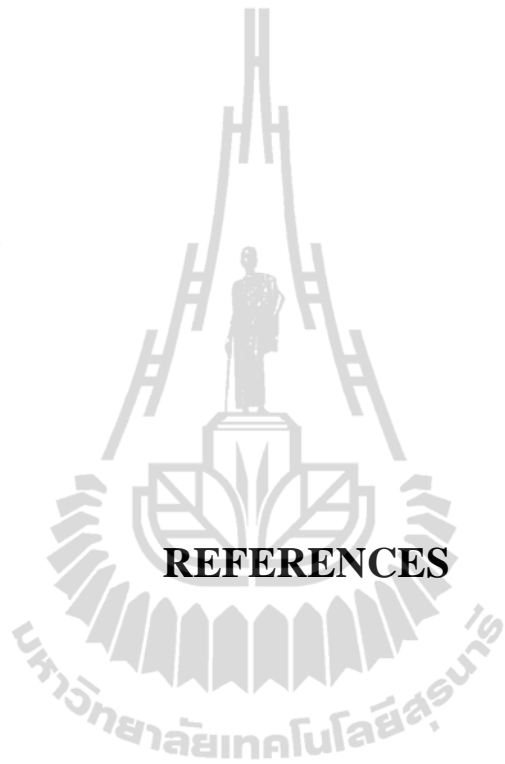
oxygen exposure. The analysis of the spectra allows the determination of ZnO formation. It was found that the oxidation process takes place until reaching the critical thickness, at which the oxidation rate reduces greatly to nearly zero. At the initial oxidation, the oxidation rate follows a two-stage logarithmic equation and later trends to saturate at a certain thickness depending on oxidation temperature. The saturated thickness was determined to be about 2 monolayers or 5 Å for oxidation at room temperature. The saturated thickness was found to increase with oxidation temperature. The two-stage oxidation process may be governed by two kinds of space charge presumably formed in the thin oxide overlayer. The activation energy for the oxidation of Zn at temperatures between room temperature and 110 °C was found to be 0.05 and 0.081 eV/mol. for the first and second stages, respectively.

It is interesting to point out also that oxidation of clean Zn surface could also be induced by low-energy ion beam bombardment. In this work, it was found that Ar⁺ ion sputtering of Zn surface could also induce the formation of ZnO if there is oxygen gas existing in the sputtering system. The partial pressure of oxygen used in this work was about 5×10^{-7} Torr. The ion energy of Ar was varied from 1 to 3 keV. The amount of the oxide was found to increase with the ion energy. The formation of ZnO was also found at even low partial pressure of oxygen at about 1×10^{-8} Torr when O⁺ ions were used for ion bombardment/sputtering.

This work also demonstrated the capability for the photoemission spectroscopy to determine the position of the valence band maximum of semiconductors such as ZnO. From photoelectron spectra, the position of the valence band maximum of the ZnO prepared by thermal annealing in air is located at different position of that prepared by exposing a clean Zn to oxygen in a UHV condition. This

indicates the different position of the Fermi level of the two samples. This opens the possibility for further investigations of formation of *p*-type ZnO by thermal annealing combining with *in-situ* observation by photoemission technique.





REFERENCES

REFERENCES

- Abbati, I., Braicovich, L. and Powell, R. A. (1979). "UV photoemission of the zinc/oxygen system : time evolution of oxygen derived structure". **Surf. Sci.** 87 : L243-L246.
- Alivov, Y. I., Chernykh, A. V., Chukichev, M. V. and Korotkov, R. Y. (2005). "Thin polycrystalline zinc oxide films obtained by oxidation of metallic zinc films". **Thin Solid Films** 473 : 241-246.
- Aoumeur, F. Z., Benkabou, Kh. and Belgoum, B. (2003). "Structural and dynamical properties of ZnO in zinc-blende and rocksalt phases". **Physica B** 337 : 292-297.
- Arrhenius, A. S. (1889). "Kinetic : Activation Energy". [On-line] : <http://www.chem.tamu.edu/class/majors/tutorialnotefiles/activation.htm>.
- Bangham, D. H. and Stafford, J. (1925). "The Velocity of Oxidation of the Metals and the Structure of Coloured Oxide Films." **The nature** 115 : 83-84.
- Barr, T. L. (1994). "Modern ESCA, The principles and Practice of X-Ray Photoelectron Spectroscopy". Florida.
- Berglund, C. N. and Spicer, W. E. (1964). "Photoemission studies of copper and silver". **Phys. Rev.** 136 : 1030-1044.
- Bernhardt, J. W. and Harry, L. T. (1994). "Lattice and Diffusion, grain boundary diffusion and defect structure of ZnO". **J. Phys. Chem. Solids.** 55 : 975-984.

- Bhavani, K. and Vaidyan, V. K. (1981). "Oxidation of Ion and Influence of an Electric Field at Room Temperature". **Oxidation of Metals** 15 : 137-145.
- Briggs, D. (1975). "Electron Spectroscopic Studies of the Initial Oxidation of Zinc". **Faraday Discuss. Chem. Soc.** 60 : 81-88.
- Bunn, C. W. (1935). "The lattice dimensions of zinc oxide". **Proc. Phys. Soc.** 47 : 835-842.
- Cao, P., Zhao, D. X., Zhang, J. Y., Shen, D. Z., Lu, Y. M., Yao, B., Li, B. H., Bai, Y. and Fan, X. W. (2008). "Optical and electrical properties of p-type ZnO fabricated by NH₃ plasma post-treated ZnO thin films". **Appl. Surf. Sci.** 254 : 2900-2904.
- Carlson, A. T. (1975). "AES Theory : Auger Electron Energies". [On-line]:
- Chang, J. F., Shen, C. C. and Hon, M. H. (2003). "Growth characteristics and residual stress of RF magnetron sputtered ZnO:Al films". **Ceramics International** 29 : 245-250.
- Cho, S., Ma, J., Kim, Y., Sun, Y., Wong, G. K. L. and Kettersonb, J. B. (1999). "Photoluminescence and ultraviolet lasing of polycrystalline ZnO thin films prepared by the oxidation of the metallic Zn". **Appl. Phys. Lett.** 75 : 2761-2763.
- Chourasia, A. R. and Chopra, D. R. (1997). "Auger Electron Spectroscopy". Handbook of Analytical Chemistry, Prentice Hall.
- Coskun, C. and Look, D. C. (2004). "Radiation hardness of ZnO at low temperatures". **Semicond. Sci. Technol** 19 : 752-754.

- Demian, S. E. (1940). "Optical and electrical properties of transparent conducting ZnO films prepared by spray pyrolysis". **J. Mater. Sci. Mater. Electron** 5 : 360-363.
- Djurisic, A. B., Chan, Y. and Li, E. H. (2002). "Progress in the room-temperature optical function of semiconductors". **Mater Sci. Eng.** R38 : 237-293.
- Ellmer, K. (2001). "Resistivity of polycrystalline zinc oxide films : current status and physical limit". **J. Phys. D: Appl. Phys.** 34 : 3097-3108.
- Ellmer, K. and Klein, A. (2008). "ZnO and Its Applications". **Springer Series in Materials Science.** 104 : 1-33.
- Fehlner, F. P. and Mott, N. F. (1970, 1971). "Oxidation of Metals, Oxidation of Metals and Alloys". **Oxidation Metals** 2 : 37, 59-66.
- Florescu, D. I., Mourokh, L. G. and Pollak, F. H. (2002). "High spatial resolution thermal conductivity of bulk ZnO (0001)". **J. Appl. Phys.** 91 : 890-892.
- Futsuhara, M., Yoshioka, K. and Takai, O. (1998). "Optical properties of zinc oxynitride thin films". **Thin Solid Films** 317 : 322-325.
- Gaineyt, T. C. and Hopkins, B. J. (1981). "Oxidation of the Zn(0001) surface". **J. Phys. C: Solid State Phys.** 14 : 5763-5768.
- Girard, R. T., Tjernberg, O., Chiaia, G., Soderholm, S., Karlsson, U. O., Wigren, C., Nylen, H. and Lindau, I. (1997). "Electronic structure of ZnO(0001) studied by angle-resolved photoelectron spectroscopy". **Surf. Sci.** 373 : 409-417.
- Gopel, W., Pollmann, J., Ivanov, I. and Reihl, B. (1982). "Angle-resolved photoemission from polar and nonpolar zinc oxide surfaces". **Phys. Rev. B** 26 : 3144-3150.

- Gregory, W. T., Jules, L. R. and Thomas, O. (2000). "Zinc self-diffusion, electrical properties, and defect structure of undoped, single crystal zinc oxide". **J. Appl. Phys.** 87 : 117-123.
- Gruzintsev, A. N and Red, A. N. (2006). "Luminescence of CVD ZnO Nanocrystals of Different Shapes". **Inorganic Materials** 42 : 508-514.
- Guan, H., Xia, X., Zhang, Y., Gao, F., Li, W., Wu, G., Li, X. and Du, G. (2008). "Study of arsenic doping ZnO thin films grown by metal-organic chemical vapor deposition via x-ray photoelectron spectroscopy". **J. Phys. Condens. Matter.** 20 : 292202-6.
- Guziewicz, E., Kopalko, K., Sadowski, J., Guziewicz, M., Golacki, Z., Kanski, J. and Ilver, L. (2005). "Mn on the Surface of ZnO(0001)-a Resonant Photoemission Study". **Physica Scripta T115** : 541-544.
- Hallwachs, W. (1916). "Die Lichtelektrizitat Handbuch der Radiologie". Leipzig : Akad. Verlagsges, Leipzig.
- Han, M. Y. and Jou, J. H. (1995). "Determination of the mechanical properties of r.f.-magnetron-sputtered zinc oxide thin films on substrates". **Thin Solid Films** 260 : 58-64.
- Hauffe, K. (1965). "Oxidation of Metals". New York: Plenum Press.
- Hickernell, F. S. (1976). "Zinc-Oxide ThinFilm Surface-Wave Transducers". **Proc. IEEE** 64 : 631-635.
- [http:// www.eaglabs.com/training/tutorials/aes_theory_tutorial/electron.php](http://www.eaglabs.com/training/tutorials/aes_theory_tutorial/electron.php).
- Hufner, S. (2003). "Photoelectron Spectroscopy". Principles and Applications, Springer-Verlag Berlin Heidelberg.

- Hutson, A. R. (1960). "Piezoelectricity and Conductivity in ZnO and CdS". **Phys. Rev. Lett.** 4 : 505-507.
- Isa, S. A. and Saleh, J. M. (1971). "Oxidation of Metal Films by Nitrous Oxide". **Physical Chemistry** 76 : 2530-2535.
- Jacobi, K., Zwicker, G. and Gutmann, A. (1984). "Work function, Electron affinity and band bending of zinc oxide surfaces". **Surface Sci.** 141 : 109-125.
- Jaffe, J. E., Snyder, J. A., Lin, Z. and Hess, A. C. (2000). "LDA and GGA calculations for high-pressure phase transitions in ZnO and MgO". **Phys. Rev. B** 62 : 1660-1665.
- Jeffrey, R. S. and David, A. C. (1999). "Recent Advances in XPS Characterization of Ultra-thin Oxides".
- Joseph, M., Tabata, H. and Kawai, T. (1999). "p-Type Electrical Conduction in ZnO Thin Films by Ga and N Codoping". **Jpn. J. Appl. Phys.** 38 : L1205-L1207.
- Joseph, M., Tabata, H., Saeki, H., Ueda, K. and Kawai, T. (2001). "Fabrication of the low-resistive p-type ZnO by codoping method". **Physica B** 302-303 : 140-148.
- Klingshirn, C. (1975). "The Luminescence of ZnO under High One- and Two-Quantum Excitation". **Phys. Stat. Sol. B** 71 : 547-556.
- Klingshirn, C. (2007). "ZnO: Material, Physics and Applications". **Chem. Phys. Chem.** 8 : 782-803.
- Kobayashi, A., Sankey, O. F. and Dow, J. D. (1983). "Deep energy levels of defects in the wurtzite semiconductors AlN, CdS, CdSe, ZnS, and ZnO". **Phys. Rev. B** 28 : 946-956.
- Krishanmoorthy, P. K. and Sircar, S. C. (1969). "oxidation kinetics of copper in the thin film range". **Acta. Met.** 17 : 1009-1012.

- Krozer, A. and Kasemo, B. (1980). "Kinetics of initial oxidation of UHV prepared Zn films". **Surf. Sci.** 97 : L339-L344.
- Kubaschewski, O. and Hopkins, B. E. (1962). "Oxidation of Metals and Alloys". London: Butterworths.
- Lawless, K. R. (1965). "Processus de Nucleation dans les Reactions des Gaz sur les Metaux et Problemes connexes". **Int. Cent. Nat. Rech. Sci.** 122 : 27-31.
- Lawless, W. N. and Gupta, T. K. (1986). "Thermal properties of pure and varistor ZnO at low temperatures". **J. Appl. Phys.** 60(2) : 607-611.
- Li, Z. W., Gao, W. and Reeves, R. J. (2005). "Zinc oxide films by thermal oxidation of zinc thin films". **Surf. Coat. Technol.** 198 : 319-323.
- Liang, H. W., Lu, Y. M., Shen, D. Z., Liu, Y. C., Yan, J. F., Shan, C. X., Li, B. H., Zhang, Z. Z., Zhang, J. Y. and Fan, X. W. (2005). "P-type ZnO thin films prepared by plasma molecular beam epitaxy using radical NO". **Phys. Stat. Sol. (a)** 202 : 1060-1065.
- Limpijumnong, S., Li, X., Wei, Su. H. and Zhang, S. B. (2006). "Probing deactivations in Nitrogen doped ZnO by vibrational signatures : A first principles study". **Physica B** 376-377 : 686-689.
- Liu, Y., Zhao, L. and Lian, J. (2006). "Al-doped ZnO films by pulsed laser deposition at room temperature". **J. Vacuum** 81 : 18-21.
- Look, D. C. (2001). "Recent advances in ZnO materials and devices". **Mater. Sci. Eng. B** 80 : 383-387.
- Look, D. C. (2005). "Electrical and optical properties of p-type ZnO". **Semicond. Sci. Technol.** 20 : S55-S61.

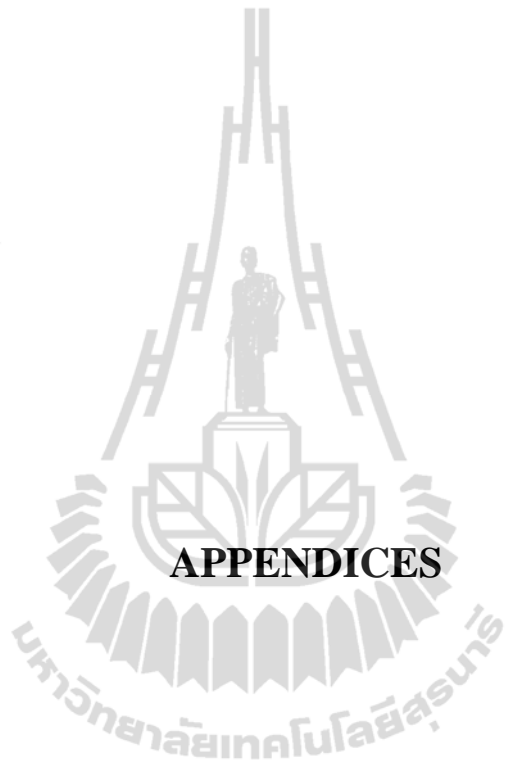
- Look, D. C. and Claflin, B. (2004). "P-type doping and devices based on ZnO". **Phys. Stat. Sol. (b)** 241 : 624-630.
- Look, D. C., Far, G. C., Reunchan, P., Limpijumng, S., Zhang, S. B. and Nordlund, K. (2005). "Evidence for Native-Defect Donors in *n*-Type ZnO". **Phys. Rev. Letts.** 95 : 225502-5.
- Look, D. C., Reynolds, D. C., Litton, C. W., Jones, R. L., Eason, D. B. and Cantwell, G. (2002). "Characterization of homoepitaxial p-type ZnO grown by molecular beam epitaxy". **Appl. Phys. Lett.** 81 : 1830-1832.
- Lori, E. G., Law, Matt., Goldberger, J., Kim, F., Johnson, J. C., Zhang, Y., Saykally, R. J. and Yang, P. (2003). "Low-Temperature Wafer-Scale Production of ZnO Nanowire Arrays". **Angew. Chem. Int. Ed.** 42 : 3031-3034.
- L'vov, B. V., Ugolkov, V. L. and Grekov, F. F. (2004). "Kinetics and mechanism of free-surface vaporization of zinc, cadmium and mercury oxides analyzed by the third-law method". **Thermochimica. Acta.** 411 : 187-193.
- Lyons, J. L., Janotti, A. and Van de Walle, C. G. (2009). "Why nitrogen cannot lead to p-type conductivity in ZnO". **Appl. Phys. Lett.** 95 : 252105-3.
- Miyazaki, E. (1983). "Theoretical study of oxygen chemisorption on zinc surface by cluster models". **Surf. Sci.** 131 : L386-L390.
- Mott, N. F. (1939a). "The oxidation of metals". **Proc. R. Soc., Trans. Faraday Soc.** A 171 : 944-949.
- Mott, N. F. (1940). "The oxidation of metals". **Proc. R. Soc., Trans. Faraday Soc.** A 36 : 472-478.
- Mott, N. F. and Cabrera, N. (1947a). "Theory of the oxidation of metals". **Trans. Faraday Soc., Rep. Prog. Phys.** 12 : 163-184.

- Nakamura, R. and Lee, J. G. (2007). "Formation of hollow ZnO through low-temperature oxidation of Zn nanoparticles". **Materials Letters** 61 : 1060-1063.
- Natsume, Y. and Sakata, H. (2000). "Zinc oxide films prepared by sol-gel spin-coating". **Thin Solid Films** 372 : 30-36.
- Nishino, J. and Nosaka, Y. (2004). "Low temperature preparation of ZnO by a nearby vaporizing chemical vapor deposition method". **J. Cryst. Growth**. 268 : 174-177.
- Noothongkaew, S., Supruangnet, R., Meevasana, W., Nakajima, H., Limpijumnong, S. and Songsiriritthigul, P. (2009). "In situ monitoring of ZnO formation by photoemission spectroscopy". **Appl. Surf. Sci.** 256 : 980-983.
- Nordling, C., Sokolowski, E. and Siegbahn, K. (1957). "Precision method for obtaining absolute values of atomic binding energies". **Phys. Rev.** 105 : 1676-1677.
- Pauling, L. (1960). "The Nature of the Chemical Bond". Cornell University, Ithaca, New York.
- Petravic, M., Deenapanray, P. N. K., Coleman, V. A., Jagadish, C., Kim, K. -J., Kim, B., Koike, K., Sasa, S., Inoue, M. and Yano, M. (2006). "Chemical states of nitrogen in ZnO studied by near-edge X-ray absorption fine structure and core-level photoemission spectroscopies". **Surface Science** 600 : L81-L85.
- Rackauskas, S., Nasibulin, A. G., Jiang, H., Tian, Y., Statkute, G., Shandakov, S. D., Lipsanen, H. and Kauppinen, E. I. (2009). "Mechanistic investigation of ZnO nanowire growth". **Appl. Phys. Lett.** 95 : 183114-6.
- Reeber, R. R. (1970). "Lattice Parameters of ZnO from 4.2° to 296° K". **J. Appl. Phys.** 41 : 5063-5066.

- Reinert, F. and Hufner, S. (2005). "Photoemission spectroscopy-from early days to recent applications". **New Journal of Physics** 7 : 97-126.
- Roberts, M. W. (1962). "Metal oxidation". **Quart. Rev. Chem. Soc.** 16 : 71-75.
- Rossi, G. and Braicovich, L. (1979). "Oxidation of cadmium: An ultraviolet-photoemission and electron energy loss investigation". **Phys. Rev. B** 21 : 3539-3544.
- Sarkar, A., Ghosh, S., Chaudhuri, S. and Pal, A. K. (1991). "Studies on electron transport properties and the burstein-moss shift in indium-doped ZnO films". **Thin Solid Films** 204 : 255-264.
- Sato, Y. and Sato, S. (1996). "Preparation and some properties of nitrogen-mixed ZnO thin films". **Thin Solid Films** 281-282 : 445-448.
- Seah, M. P. and Dench, W. A. (1979). "Inelastic mean free path of electron at different energies". **Surf. Interface Anal.** 1 : 2.
- Shirley, D. A. (1972) "High-Resolution X-ray Photoemission Spectrum of the Valence Bands of Gold". **Phys. Rev. B** 5 : 4709-4714.
- Smith, T. (1973). "Oxidation of Titanium between 25 C and 400 C". **Surf. Sci.** 38 : 292-312.
- Songsiriritthigul, P., Pairsuwan, W., Ishii, T. and Kakizaki, A. (2007). "Design of the first undulator beamline for the Siam Photon Laboratory". **Nuclear Instruments and Methods in Physics Research. A** 582 : 100-102.
- Songsiriritthigul, P., Pairsuwan, W., Ishii, T. and Kakizaki, A. (2001). "Photoemission Beamline at The Siam Photon Laboratory". **Surf. Rev. Lett.** 8 : 497-500.

- Spicer, W. E. and Berglund, C. N. (1964). "d-Band of copper". **Phys. Rev. Lett.** 12 : 9-11.
- Tammann, G., Koster, W. and Anorg, Z. (1922). "Velocity of Action of Oxygen, Hydrogen Sulfide, and Halogens of Metals". **Allgem. Chem.** 123 : 196-224.
- Tougaard, S. and Mohai, M. (1988). "IMFP : Inelastic Mean Free path". [On-line] : <http://www.lasurface.com>.
- Turner, D. W. and Baker, C. (1970). *Molecular Photoelectron Spectroscopy*. London, Wiley-Interscience.
- Uhlig, H. H. (1956). "Initial oxidation rate of metals and the logarithmic equation". **Acta. Met.** 4 : 541-554.
- Unertl, W. N. and Blakely, J. M. (1977). "Growth and properties of oxide films on Zn (0001)". **Surf. Sci.** 69 : 23-52.
- Vincent, O. N. and Uhlig, H. H. (1965). "Logarithmic Oxidation Kinetics of Zinc". **J. Electrochem. Soc.** 112 : 1181-1185.
- Vogel, D., Kruger, P. and Pollmann, J. (1995). "ab initio electronic-structure calculations for II-VI semiconductors using self-interaction-corrected pseudopotentials". **Phys. Rev. B** 52 : R14 316-319.
- Wang, Y. G., Lau, S. P., Lee, H. W., Yu, S. F. and Tay, B. K. (2003). "Photoluminescence study of ZnO films prepared by thermal oxidation of Zn metallic films in air". **Appl. Phys.** 94 : 354-358.
- Wei, Z. P., Lu, Y. M., Shen, D. Z., Zhang, Z. Z., Yao, B., Li, B. H., Zhang, J. Y., Zhao, D. X. and Fan, X. W. (2008). "Fabrication of Nitrogen Doped *p*-ZnO and ZnO Light-Emitting Diodes on Sapphire". **J. Korean Phys. Soc.** 53 : 3038-3042.

- Widemann, H. (1995). **Particle Accelerator Physics**. Vol. II, Berlin, Springer.
- Xiang, Z. D. and Rose, S. R. (2006). "Long-term oxidation kinetics of aluminide coatings on alloy steels by low temperature pack cementation process". **Mater Sci.** 41 : 7353-7360.
- Yang, Y. H. and Yang, G. W. (2010). "Temperature dependence and activation energy of ZnO nanowires grown on amorphous carbon". **Chemical Physics Letters** 494 : 64-68.
- Yuan, G. D., Ye, Z. Z., Huang, J. Y., Zhu, L. P., Perkins, C. L. and Zhang, S. B. (2009). "X-ray photoelectron spectroscopy study of Al- and N-co-doped p-type ZnO thin films". **J. Cryst. Growth** 311 : 2341-2344.
- Zhao, J., Hu, L., Wang, Z., Zhao, Y., Liang, X. and Wang, M. (2004). "High-quality ZnO thin films prepared by low temperature oxidation of metallic Zn". **Appl. Surf. Sci.** 229 : 311-315.
- Zheng, H. and Du, X. L. (2007). "Wet chemical etching of ZnO film using aqueous acidic salt". **Thin Solid Films** 515 : 3967-3970.
- Zou, C. W., Chen, R. Q. and Gao, W. (2009). "The microstructures and the electrical and optical properties of ZnO:N films prepared by thermal oxidation of Zn₃N₂ precursor". **Solid State Communications** 149 : 2085-2089.
- Zou, C. W., Yan, X. D., Han, J., Chen, R. Q., Gao, W. and Metson, J. (2009). "Study of a nitrogen-doped ZnO film with synchrotron radiation". **Appl. Phys. Lett.** 94 : 1719031-3.



Abstract submitted for the Siam Physics Congress 2008, Nakorn Ratchasima (2008)

SPC 2008

NAKORN RACHASIMA, THAILAND

Oral () / Poster (✓)

Onset of the Formation of Zinc Oxide at Room Temperature

S. Noothongkaew^{1}, H. Nakajima², W. Meevasana^{2,3}, and P. Songsirithigul^{1,2}*

¹School of Physics, Suranaree University of Technology, Nakhon Ratchasima, Thailand

²National Synchrotron Research Center, Nakhon Ratchasima, Thailand

³Department of Physics, Stanford University, Stanford, California, USA

Abstract

Zinc oxide (ZnO) have been great interested because of its unique properties, such as wide band gap and transparent conductive material, which are demanded in many promising applications. ZnO is normally formed at elevated temperatures. In this work, the onset of the formation of ZnO at room temperature was investigated using Auger electron and photoemission spectroscopic techniques. The formation of ZnO was observed when a clean Zn surface exposed to O₂ in UHV environment. A very-low-energy ion beam (<3 keV) was also used to intend to promote the growth of ZnO. Oxygen ion was found to enhance the formation of ZnO while Ar⁺ ions had no contribution to the formation of ZnO. The formation of ZnO at room temperature was confirmed by comparing with the ZnO formed by thermal oxidation at 150°C in air.

Keyword: ZnO, Auger electron spectroscopy, photoemission

* Corresponding author. Email: lamduan_57@hotmail.com

Abstract submitted for the Siam Physics Congress 2009, Phetchburi (2009)

SPC2009
PHETCHBURI, THAILAND

Oral () / Poster (✓)

Photoemission for Thickness Measurements of Ultra thin ZnO films

S. Noothongkaew¹, H. Nakajima^{2,3}, W. Meevasana² and P. Songsiriritthigul^{1,2,3}*

¹ Nanospectroscopy Laboratory/ThEP Center, School of Physics, Suranaree University of Technology, Nakhon Ratchasima, Thailand

²National Synchrotron Research Center, Nakhon Ratchasima, Thailand

Abstract

This work demonstrates the application of photoemission spectroscopy using synchrotron light for quantitative determination of the thickness of ultra-thin ZnO films of less than 3 monolayers, which were formed by thermal oxidation of clean Zn substrates at room temperature. The reduction of density of state of Zn 4s electrons and the positive binding-energy shift of Zn 3d level in photoelectron spectra were used as the indicator for the formation of ZnO. Photoelectron spectra taken from these ultra-thin ZnO film samples constitute photoelectrons emitted from the oxide layer and from the underlying Zn substrate. With the known values of the inelastic mean free path of electrons in the oxide and substrate, the ratio between the Zn 3d density of state of the oxide layer to that of the substrate can be used to calculate the thickness of the oxide layer.

Keyword: ZnO, oxidation of Zn, photoemission spectroscopy, synchrotron light, ultra-thin film

* Corresponding author. Email: prayoon@slri.or.th

Abstract submitted for the Siam Physics Congress 2010, Kanchanaburi (2010)

SPC2010
KANCHANABURI, THAILAND

Oral () / Poster (✓)

Magnetic Circular Dichroism (MCD) of Ni sample With UV-PEEM

*S. Shin¹, K. Ono², T. Taniuchi³, Y. Kotani^{2,4}, K. Isogai⁵,
S. Noothongkaew^{6,7,8}, and P. Songsirithigul^{6,7,8},*

¹*Riken Spring-8 Center, Kouto 1-1-1, Sayo-cho, Sayo-gun, Hyogo 679-5148, Japan*

²*Institute of Materials Structure Science, High Energy Accelerator Research
Organization (KEK), Tsukuba, Ibaraki 305-0801, Japan*

³*Institute for Solid State Physics, The University of Tokyo, Kashiwa, Chiba
277-8581, Japan*

⁴*Department of Materials Structure Science, The Graduate University for Advanced
Studies (Sokendai), Tsukuba, Ibaraki 305-0801, Japan*

⁵*The Tokyo University of Science, Japan*

⁶*School of Physics, Institute of Science, Suranaree University of Technology, Nakhon
Ratchasima, Thailand*

⁷*Thep Center, Commission on Higher Education, Bangkok 10400, Thailand*

⁸*Synchrotron Light Research Institute, Nakhon Ratchasima 30000, Thailand*

Abstract

This report presents the observation of magnetic circular dichroism (MCD) of a 50-nm polycrystalline Ni film using photoemission electron microscopy (PEEM) with visible and ultraviolet lasers. The Ni film was prepared on a silicon substrate. PEEM observations were performed in an ultra-high vacuum chamber with base pressure of 2×10^{-10} Torr. The obtained results confirmed that MCD exist on the Ni film, indicating that magnetic domains can be visualized by PEEM imaging.

Keyword: photoemission electron microscope (PEEM), magnetic circular dichroism (MCD).



Contents lists available at ScienceDirect

Applied Surface Science

journal homepage: www.elsevier.com/locate/apsusc

In situ monitoring of ZnO formation by photoemission spectroscopy

Suttinart Noothongkaew^{a,b}, Ratchadaporn Supruangnet^{a,b}, Worawat Meevasana^{a,c}, Hideki Nakajima^{a,d}, Sukit Limpijumnong^{a,b}, Prayoon Songsiriritthigul^{a,b,d,*}

^a Synchrotron Light Research Institute, Nakhon Ratchasima 30000, Thailand

^b School of Physics, Suranaree Univ. of Tech., Nakhon Ratchasima 30000, Thailand

^c Department of Physics, Stanford University, Stanford, CA 94305, USA

^d THEP Center, Commission on Higher Education, Bangkok 10400, Thailand

ARTICLE INFO

Article history:

Received 28 October 2008

Received in revised form 27 February 2009

Accepted 28 May 2009

Available online 6 June 2009

PACS:

82.40.-g

82.65.+r

68.47.Gh

79.60.-i

Keywords:

ZnO

Oxidation of Zn

Photoemission spectroscopy

Synchrotron radiation

ABSTRACT

Exposure of a clean Zn metal to oxygen in ultra high vacuum provides a mean to gradually form ZnO. With *in situ* synchrotron photoelectron measurement, the progressive change in the spectra with the oxygen exposure time is observed. The analysis of the spectra allows the determination of ZnO formation. It was found that the oxidation process takes place until reaching the critical thickness, at which the oxidation rate reduces greatly to nearly zero. The critical thickness was determined to be about 2 monolayers.

© 2009 Elsevier B.V. All rights reserved.

1. Introduction

In spite of the fact that polycrystalline zinc oxide (ZnO) has been used in a wide range of applications for over a hundred year, there are renewed research interests on this material in the last decade. For its electronic and blue-light optoelectronic applications, thin film ZnO has attracted much attention. It has many attractive properties such as a wide direct band gap of 3.27 eV and large exciton binding energy of 60 meV [1–6]. Recent progresses in many growth techniques make it possible to synthesize high quality ZnO thin films. Thermal oxidation of pre-deposited Zn films has been demonstrated to be one of simple techniques to obtain ZnO thin films [7–11]. Because ZnO has great potential for future technological applications, the initial state of the oxidation of Zn, or in other words, the interaction of oxygen with Zn surface atoms, is of great fundamental interest. Extensive experimental work on the initial oxidation of Zn was performed using low-energy electron

diffraction and Auger electron spectroscopy in 1970s [12,13]. To our knowledge, there has been a discontinuity of such a work even though interesting findings at the time were not confirmed. This work devotes to the investigation of the initial states of ZnO formation by using *in situ* high-resolution synchrotron photoemission measurements of clean Zn surfaces exposed to oxygen in an ultra high vacuum (UHV) environment at room temperature.

2. Experiment

ZnO films were formed on polycrystalline Zn foils with 99.99% purity and 0.05 mm thick in UHV environment at room temperature by exposure of a clean Zn surface to oxygen. Initially, the Zn foils were cleaned with alcohol and de-ionized water, respectively, in an ultrasonic bath before loading into the UHV system. Oxidation of the Zn foils was performed and characterized within the experimental station of the photoelectron spectroscopy (PES) beamline, BL4, of the Siam Photon Laboratory [14]. The experimental station is a multi-UHV-chamber system consisting an electron spectroscopy system, a preparation system for surface cleaning, a metal MBE system and in-vacuum sample transfer system. The electron spectrometer, equipped with a Thermo VG

* Corresponding author at: Synchrotron Light Research Institute, P.O. Box 93, Nakhon Ratchasima 30000, Thailand. Tel.: +66 44 217040x400; fax: +66 44 217047. E-mail address: prayoon@slri.or.th (P. Songsiriritthigul).

Scientific Alpha110 electron energy analyzer, utilizes synchrotron light (~ 40 – 240 eV) and electron beam for synchrotron PES and Auger electron spectroscopy (AES), respectively. After loading into the UHV system, the surface of Zn samples was further cleaned by Ar^+ ions sputtering. AES was used to verify the cleanliness of the surface of the Zn foils. To form ZnO by exposure of a clean surface to oxygen, oxygen gas was let into the photoemission system, raising the vacuum pressure from the base pressure of $\sim 1 \times 10^{-10}$ to 5×10^{-7} Torr. The exposure time was varied from 5 to 180 min. After each exposure, the spectra of photoelectrons generated by 51 eV photons were recorded. Normal emission was chosen in order to detect the photoelectrons from Zn covering by an oxide layer.

3. Results and discussions

Fig. 1 shows normalized photoelectron spectra of a clean surface of Zn foils exposed to oxygen for various doses taken with a photon energy of 51 eV at normal emission. The exciting photon energy of 51 eV was chosen in order to compare the measured spectra with the spectrum of a single crystal ZnO taken at 51 eV photon energy by Guzewicz et al. [15] (a slight shift in the binding energy of -0.3 eV, due to different Fermi levels, is applied). The measured spectra are normalized with the photoelectron current measured by a gold mesh placed in between the post-focusing mirror and the sample [14]. The secondary electrons background of the spectra was subtracted using Shirley method [16]. For the clean Zn sample, the spectra contain two steep overlapping peaks at 9.9 and 10.5 eV, labeled A and B, respectively. These two peaks covering the energy region from 9.3 to 11.3 eV are associated with Zn 3d electrons. The spectrum has almost no other feature except a

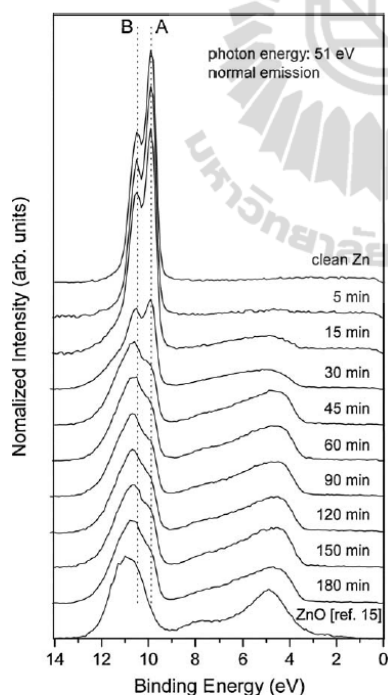


Fig. 1. Normalized photoemission spectra of clean surface of Zn foils exposed to oxygen in UHV at 5×10^{-7} Torr for various exposure times.

relatively much smaller shoulder near the Fermi level which will be discussed later. Upon exposing the clean surface of Zn foils to oxygen at room temperature, the series of the spectra in Fig. 1 clearly show the effect of oxygen exposure. The shape and magnitude of the peaks associated with Zn 3d are varied. The variation is accompanied by another change of the spectra in the valence bands region. It is obvious that oxygen induces a shift of peak B towards higher binding energy whereas the strength of peak A is reduced and a broad lump in the lower region of the binding energy (3–9 eV) appeared. In ZnO, the lump in this low-energy region has been assigned to the valence band states composed mainly of O 2p and Zn 4s. Therefore, the appearance of the lump in the valence band region indicates the incorporation of the O atoms in the form of Zn–O bonding. The overall progressive variation of the spectra with the exposure time can be viewed as the switching of Zn atoms from the metal form to ZnO form.

From Fig. 1, it is interesting to point out that the intensity of the Zn 3d electrons greatly reduces by more than half when the exposure time is increased from 15 to 30 min while there is only minimal increase of the intensity in the lower binding energy region. Clearly, the increase in the intensity in the low binding energy region cannot account for the missing intensity in the Zn 3d region. The explanation may be found in Fig. 2, which shows the zoom-up photoelectron spectra in the valence band region for the clean Zn surfaces without and with oxygen exposures for 15 and 30 min. For the clean Zn sample, the spectrum has a clear shoulder near the Fermi level which is a typical feature of metal valence electron states (Zn 4s). For the sample exposed for 15 min, the intensity of Zn valence electrons near the Fermi level remains virtually the same as those of the clean Zn. This indicates that, in the sample exposed for 15 min, only a very small amount of Zn surface atoms is chemically interacted with oxygen. Majority of Zn atoms still remain in the metallic phase with oxygen covering. After increasing the exposure time to 30 min, the intensity of the observed Zn valence electrons near the Fermi level was reduced more than a factor of 2 indicating that the Zn atoms started to form bonds with O atoms. Although, some amount of Zn valence electrons was still observed, these remaining Zn 4s signals come mostly from the underlying metallic Zn.

The oxygen coverage and the amount of ZnO formed on clean Zn foils for various oxygen exposures can be estimated from the ratio of the Zn 3d electrons emitted from ZnO and the total emitted Zn 3d electrons. Photoelectron spectra of ultra-thin films of ZnO on Zn metal are collective of photoelectrons emitting from both the oxide overlayer and the underlying Zn metal. The ratio of the intensity of Zn 3d electrons emitting from a ZnO layer ($I_{\text{Zn } 3d, \text{ZnO}}$) to the total intensity of Zn 3d electron emitting from the ZnO and the underlying Zn metal ($I_{\text{Zn } 3d, \text{total}}$) may be estimated from the

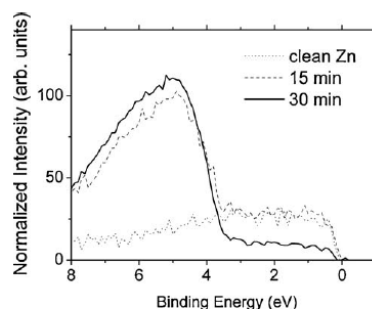


Fig. 2. Photoelectron spectra in the valence band region for the clean Zn surfaces without and with oxygen exposures for 15 and 30 min.

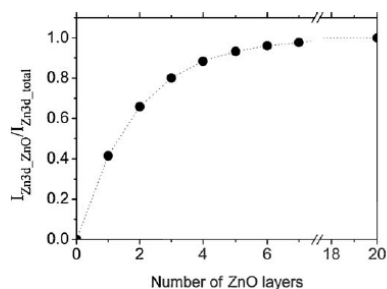


Fig. 3. Calculated ratio of the intensity of Zn 3d photoelectrons emitted from ZnO ($I_{Zn\ 3d,ZnO}$) to the intensity of all Zn 3d electrons ($I_{Zn\ 3d,total}$) as a function of ZnO thickness on thick pure Zn metal.

inelastic mean free path in ZnO and Zn (λ_{ZnO} and λ_{Zn}), which is given by

$$\frac{I_{Zn\ 3d,ZnO}}{I_{Zn\ 3d,total}} = \frac{\rho_{ZnO} \times \sum_{i=0}^n \exp(-i \times d_{ZnO}) / (\lambda_{ZnO})}{\rho_{ZnO} \times \sum_{i=0}^n \exp(-i \times d_{ZnO}) / (\lambda_{ZnO}) + \rho_{Zn} \sum_{j=1}^{\infty} \exp(-j \times d_{Zn}) / (\lambda_{Zn}) + (-n \times d_{ZnO}) / (\lambda_{ZnO})} \quad (1)$$

where ρ_{ZnO} and ρ_{Zn} are the densities of Zn atoms in ZnO and in Zn, respectively. For electrons with kinetic energy around 40 eV, the mean free paths λ_{ZnO} and λ_{Zn} are 4.8 and 4.1 Å, respectively [17]. For simplicity, ZnO is assumed to be a single crystal with n monolayers and with $d_{ZnO} = c/2 = 2.60$ Å. Zn is also considered to be in the *hcp* structure with $d_{Zn} = 2.66$ Å. The calculated intensity ratio of the Zn 3d electrons in ZnO ($I_{Zn\ 3d,ZnO}$) to the total intensity of Zn 3d electrons ($I_{Zn\ 3d,total}$) as a function of ZnO thickness is shown in Fig. 3. It should be noted that the actual Zn samples used in this work are polycrystalline Zn foils. The thickness referred in this work is an “average” or “equivalent” thickness. In the measurements, the normal emission spectra were used so that the distances used in Eq. (1) is consistent with the actual path the electrons traveled. The curve in Fig. 3 will be used to convert the measured $I_{Zn\ 3d,ZnO}/I_{Zn\ 3d,total}$ ratio to the thickness of the ZnO layer.

In the previous paragraph, we have generated the standard curve relating the ratio of intensities (between ZnO 3d electrons to all Zn 3d electrons) to the thickness of ZnO layers. In practice, the binding energy of the 3d electrons from ZnO and Zn metal are overlapped and difficult to separate. However, photoelectrons of Zn metal have a distinctive feature from those of ZnO in the region near the Fermi level (0–2.5 eV) as shown in Fig. 2. Therefore, we use the intensity of the valence electrons in the region near the Fermi level to determine the amount of intensity contributed from the underlying Zn metal. This approach should be reasonably accurate because the ZnO layers contribute only little amount of intensity in this region. The measured spectrum from the clean Zn foil sample is used to represent the spectrum of Zn metal. Fig. 4 shows photoelectron spectra of the samples exposed to oxygen for 5, 15, 30, 45 and 180 min (solid curves). For each sample, the contribution from the Zn metal underneath is determined (dash curves) by scaling the spectrum from the clean Zn foil to fit the region near the Fermi level. By subtracting the two (the solid and dash curves), the remaining spectrum (dot curves) may be considered to be the intensity of the electrons emitting from ZnO. The spectra of the clean Zn samples exposed to oxygen for 60, 90, 120 and 150 min are very similar to those of the samples exposed for 45 and 180 min, and thus are not shown.

At the exposure time of 5 min, as shown in Fig. 4(a), the difference spectrum (dot curve) has a small broad lump in the O 2p

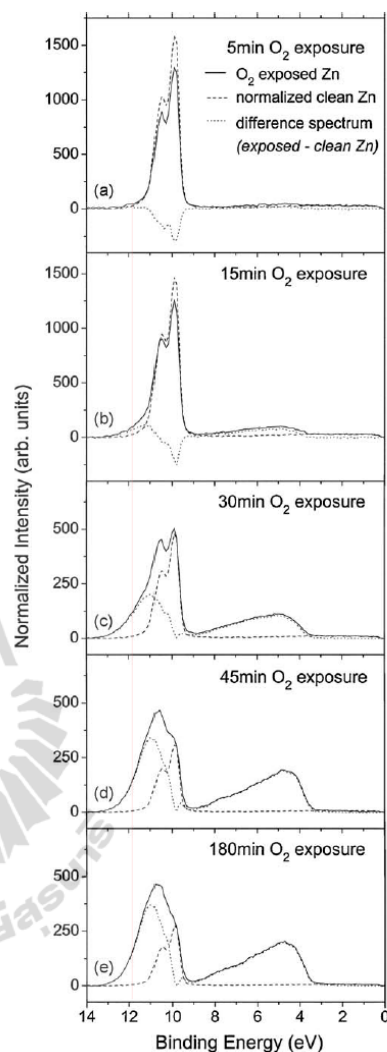


Fig. 4. The photoelectron spectra (solid curve) of the samples exposed to oxygen for 5, 15, 30, 45, and 180 min, the estimated contribution from Zn metal (dash curve), and the estimated contribution from the ZnO layer (dot curve).

energy region and small negative intensity in the Zn 3d region. The intensity in the O 2p region indicates that there is a small amount of oxygen coverage on the sample. This small amount of oxygen, however, contributes additional electron intensity in the 0–2.5 eV region. Because the intensity in that region is used to determine the Zn metal contribution, the calculated contribution from Zn metal (dash curve) becomes slightly too big. As a result, the difference spectrum (dot curve), which should normally be the contribution from the ZnO layer, become fictitiously negative.

For the sample with 15-min exposure time, as shown in Fig. 4(b), the difference spectrum (dot curve) shows the signature of Zn–O chemical bonding. There appears the intensity of Zn 3d electrons with energy shifted towards higher values. However, the

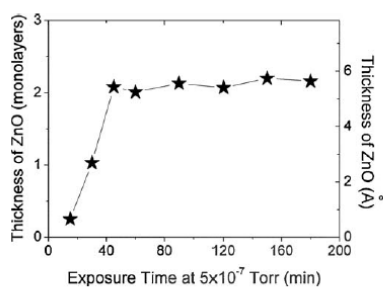


Fig. 5. The average thickness of ZnO formed on a clean Zn surface as a function of oxygen exposure time.

small negative intensity is still observed for the same reason explained above. When the exposure time increases to 30 min, the difference spectrum shows higher intensity of Zn 3d electrons with binding energy shifted towards higher values. The spectrum now contains both the peak in the Zn 3d region and the jump in the lower energy region. It clearly represents the electrons emitting from ZnO. With 45-min of oxygen exposure, the intensity of the difference spectrum increases indicating the increasing amount of ZnO formed on the metallic Zn. However, the ZnO intensity only increases very slightly when the exposure time increases from 45 to 180 min. This indicates the saturation of the ZnO layer formation.

To get a clearer picture of ZnO formation rate, the intensity ratio of the Zn 3d electrons from ZnO to the total Zn 3d electrons is calculated. To be specific, the area under the dot curve (in the binding energy range of 9–13 eV) is used for $I_{\text{Zn } 3d \text{ ZnO}}$ and the area under the solid curve is used for $I_{\text{Zn } 3d \text{ total}}$. After the ratio is obtained, the average thickness of ZnO layer can be read from the reference curve in Fig. 3. The average thickness of ZnO formed on the surface of clean Zn foils as a function of O_2 exposure time is shown in Fig. 5. The average thickness increases with exposure time, or oxygen dose, until the thickness reaches ~ 2 monolayer (or $\sim 5 \text{ \AA}$) of ZnO. At this critical thickness the growth rate of ZnO reduces to nearly zero. It is interesting to point out that when the exposure time was 30 min, the Zn 4s electrons chemically interact with O 2p to form ZnO with an average coverage of ~ 1 monolayer, resulting in the reduction of the Zn 4s electrons near the Fermi edge

as shown in Fig. 2. This indicates that the metallic phase of Zn surface has changed to the semiconductor phase.

4. Conclusions

The formation of ZnO layer has been studied by exposing clean Zn foils to oxygen in ultra high vacuum at various times. The samples are characterized by *in situ* photoelectron spectroscopic technique. This provides the possibility to access the initial oxidation process of Zn. The Zn–O bond formation can be observed from both the shift of Zn 3d level and the build up of the ZnO valence states. By dividing the total photoelectron spectra into the contributions from the Zn metal and ZnO layer forming on top, the thickness of the ZnO layer can be determined. It is found that upon oxygen exposure, the oxidation takes place with approximately constant rate until reaching the critical thickness, at which the oxidation rate has suddenly reduced to nearly zero. The critical thickness was found to be ~ 2 ZnO monolayers, or $\sim 5 \text{ \AA}$. The transition of Zn surface from a metallic to semiconductor phase can be observed when ~ 1 monolayer of ZnO was formed on the surface.

References

- [1] C. Klinshim, Phys. Status Solidi B 71 (1975) 547.
- [2] D.C. Look, B. Claflin, Phys. Status Solidi B Basic Res. 241 (2004) 624.
- [3] A.B. Djuricic, Y. Chan, E.H. Li, Mater. Sci. Eng. 38R (2002) 237.
- [4] K. Ellmer, J. Phys. D: Appl. Phys. 34 (2001) 3097.
- [5] Y.F. Chen, D. Bagnall, T. Yao, Mater. Sci. Eng. 75B (2000) 190.
- [6] D.C. Look, Mater. Sci. Eng. 80B (2001) 383.
- [7] Y.G. Wang, S.P. Lau, H.W. Lee, S.F. Yu, B.K. Tay, X.H. Zhang, H.H. Hng, J. Appl. Phys. 94 (2003) 354.
- [8] Z.W. Li, W. Gao, R.J. Reeves, Surf. Coat. Technol. 198 (2005) 319.
- [9] Ya.I. Alivov, A.V. Chernykh, M.V. Chukichev, R.Y. Koratkov, Thin Solid Films 473 (2005) 241.
- [10] S. Cho, J. Ma, Y. Kim, Y. Sun, G.K.L. Wong, J.B. Ketterson, Appl. Phys. Lett. 75 (1999) 2761.
- [11] J. Zhao, L. Hu, Z. Wang, Y. Zhao, X. Liang, M. Wang, Appl. Surf. Sci. 229 (2004) 311.
- [12] W.N. Unertl, J.M. Blakely, Surf. Sci. 69 (1977) 23, and reference therein.
- [13] I. Abbati, L. Braicovich, R.A. Powell, Surf. Sci. 87 (1979) L243, and references therein.
- [14] P. Songsiriritthigul, W. Pairsuwan, T. Ishii, A. Kakizaki, Surf. Rev. Lett. 8 (2001) 497; H. Nakajima, M. Buddhakala, R. Supruangnet, S. Chumpolkulwong, A. Kakizaki, P. Songsiriritthigul, AIP CP #879 (2007) 543.
- [15] E. Guziewicz, K. Kopalko, J. Sadoski, Z. Golacki, J. Kanski, L. Ilver, Phys. Scripta T115 (2005) 541.
- [16] D.A. Shirley, Phys. Rev. B 5 (1972) 4709.
- [17] M.P. Seah, W.A. Dench, Surf. Interface Anal. 1 (1979) 2; P.J. Cumpson, M.P. Seah, Surf. Interface Anal. 25 (1997) 430.

The 18th International Vacuum Congress

Oxidation of Zn in UHV environment at elevated temperature

Suttinart Noothongkaew^{a,b}, Hideki Nakajima^{a,c}, Anusorn Tong-on^{a,b} and Prayoon Songsiriritthigul^{a,b,c,*}

^a*School of Physics, Suranaree University of Technology, Nakhon Ratchasima, 30000, Thailand*

^b*Synchrotron Light Research Institute, Nakhon Ratchasima, 30000, Thailand*

^c*Thailand Center of Excellence in Physics, CHE, Bangkok, 10400, Thailand*

Abstract

Thermal oxidation of polycrystalline Zn foils at 5×10^{-7} Torr oxygen pressure and at room temperature, 50°C, 70°C, 90°C, and 110°C was studied. *In situ* photoemission spectroscopy using synchrotron light with photon energy of 57 eV was used to monitor the formation of ZnO and to determine the thickness of the oxide overlayer. At the initial oxidation, the oxidation rate follows a two-stage logarithmic equation and later trend to saturate at a certain thickness depending on oxidation temperature. The saturate thickness was found to increase with oxidation temperature. The two-stage oxidation process may be governed by two kinds of space charge presumably formed in the thin oxide overlayer.

© 2009 Published by Elsevier B.V.

PACS: 82.40.-g; 82.65.+r; 68.47.Gh; 79.60.-i

Keywords: ZnO; oxidation of Zn; photoemission spectroscopy; synchrotron radiation

1. Introduction

ZnO is an interesting material and is used in a wide range of applications for over a hundred years. In the last decade, one of the main renewed research interests on ZnO focuses on the synthesize of high quality *p*-type ZnO for electronic and blue-light optoelectronic applications because of its attractive properties such as a wide direct band

* Corresponding author. Tel.: +66-44-217040; fax: +66-44-217047.

E-mail address: prayoon@slri.or.th.

gap of 3.27 eV and large exciton binding energy of 60 meV [1-6]. Among different growth techniques, thermal oxidation is one of simple techniques to synthesize high quality ZnO thin films [7-11]. In addition to the applications of ZnO, it is of great fundamental interest to understand the initial state of the oxidation of Zn. Such an investigation was performed by using low-energy electron diffraction and Auger electron spectroscopy in 1970 [12-13]. The discontinuity of such an investigation came before any interesting findings were confirmed. Our previous study found that upon oxygen exposure on a clean Zn surface at 5×10^{-7} Torr and at room temperature, the oxidation takes place with approximately constant rate until reaching the saturated thickness, at which the oxidation rate has suddenly reduced to nearly zero. The transition of Zn surface from a metallic to semiconductor phase was also observed when ~ 1 monolayer of ZnO was formed on the surface [14]. The present work focuses on the kinetic behavior of the oxidation of polycrystalline Zn foils covered by thermally pre-oxidized layer. Photoemission spectroscopy using synchrotron light provides the possibility for *in-situ* measurements of ultra thin oxide films from at very partial pressure of oxygen and at low temperature.

2. Experimental

This work was performed at the photoemission spectroscopy (PES) beamline, BL3.2a, of the Synchrotron Light Research Institute of Thailand [15]. The PES system is equipped with a Thermo VG Scientific CLAM2 electron spectrometer. Zn foils with 99.99% purity and 0.05 mm thick were used in this work. The Zn foils were cleaned with alcohol and de-ionized water, respectively, in an ultrasonic bath before loading into the PES system. To obtain a good reference photoelectron spectrum of a clean Zn surface, the measurements were performed at the base pressure of $\sim 2 \times 10^{-10}$ Torr. Thus one of the samples was introduced into the analysis chamber thru a load-lock system to prevent breaking of UHV condition. The clean surface was obtain by 0.5 keV Ar^+ ion sputtering in the analysis chamber.

Oxidation of Zn was done by exposure of Zn foils with “pre-oxidized overlayer” to oxygen in the analysis chamber of the PES system. In order to assure good contact between the thermocouple and the samples to obtain reliable oxidation temperature, a chemically cleaned Zn foil was mounted on the sample holder in air and thus breaking the UHV condition of the PES system was necessary. After that baking-out the PES system was carried out at 130°C for 24 hours. The unavoidable oxide layer formed on the Zn sample during baking was later removed by Ar^+ ion sputtering. The base pressure of the analysis chamber for the measurements of the oxidized sample was $\sim 3 \times 10^{-9}$ Torr. Oxidation of the Zn foil was performed at room temperature, 50°C, 70°C, 90°C, and 110°C. Oxygen gas was let into the analysis chamber of the PES system to increase the vacuum pressure from the base pressure to 5×10^{-7} Torr. The exposure time was varied from 5 to 90 minutes. The thickness of the oxide layer was measured *in-situ* by PES technique using synchrotron light with photon energy of 57 eV from the beamline BL3.2a. Photoelectrons were detected at an emission angle of 50° with respect to the surface normal. After the sample was analyzed, the oxide layer was removed by Ar^+ sputtering to provide a fresh surface of Zn, or a “pre-oxidized sample”, for new oxidation.

3. Results and Discussion

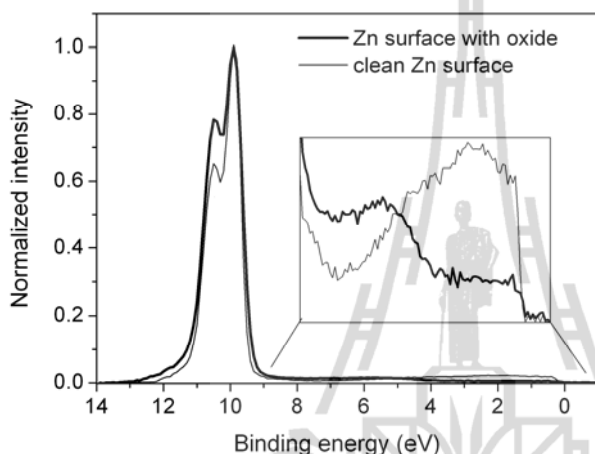


Figure 1. Photoelectron spectra taken from a clean Zn surface and a Zn surface with a pre-oxidized layer. The intensities of the photoelectrons near the Fermi level associated with Zn4s and Zn4s–O2p are shown in the inset figure.

Figure 1 shows the photoelectron spectra obtained from two Zn samples prepared with two different conditions, referring to as a “clean sample” and a “pre-oxidized sample”. The “clean sample” refers to the Zn sample that was chemically cleaned *ex situ*, loaded into the analysis chamber thru the load-lock system and sputtered by 0.5-keV Ar⁺ ions to remove surface contaminations. The measurements of photoelectron spectra of the clean sample was performed at vacuum pressure of $\sim 2 \times 10^{-10}$ Torr. The spectrum of this clean metallic Zn sample shows the density of state (DOS) of valence electrons. The two overlapping peaks at 9.9 eV and 10.5 eV covering the energy region from 9.3 eV to 11.3 eV are associated with Zn 3d electrons. Zn 4s electrons are also observed in the valence band up to the Fermi level.

The photoelectron spectrum of the “pre-oxidized sample” is a typical spectrum obtained from the Zn sample originally covered by thermally-grown ZnO layer and later cleaned by successive 3.0-keV and 0.5-keV Ar⁺ ion sputtering. The photoelectron spectrum of the pre-oxidized sample deviates from that of the clean sample, indicating different surface composition. The reduction of DOS near the Fermi level and the increase of DOS in the region between ~ 4 eV and 9 eV result from the hybridization of Zn 4s electrons and O 2p electrons to form ZnO [14]. The formation of ZnO also gives rise to the high binding-energy shift of Zn 3d electrons. The amount of the ZnO coverage for the pre-oxidized sample was estimated to be ~ 1.2 monolayers. Thus, it should be noted that the surface of the sample before exposing to oxygen already covered by a thin oxide layer.

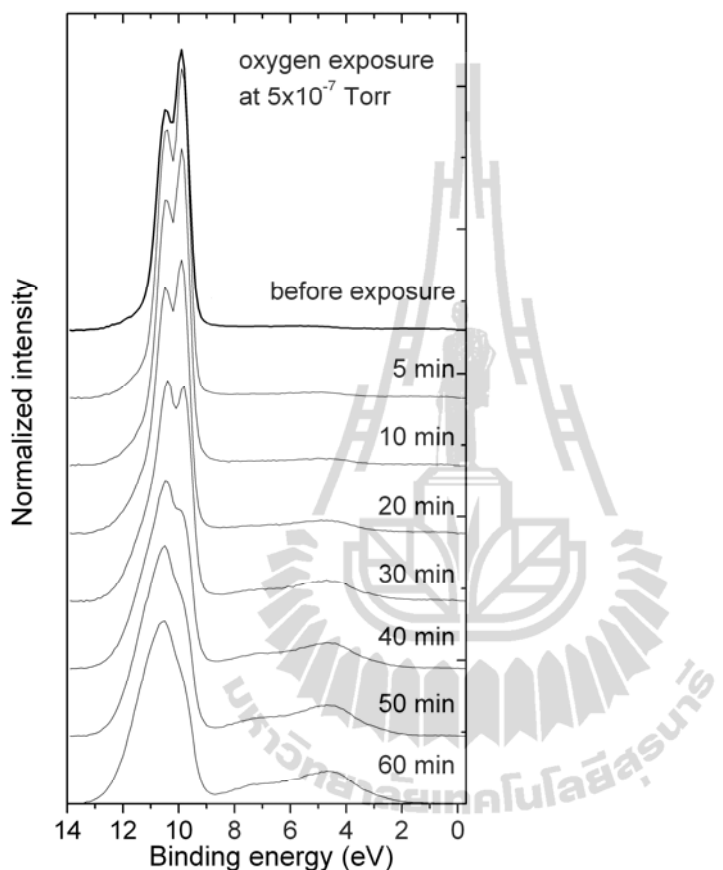


Figure 2. Photoelectron spectra taken from a Zn foil before and after exposed to oxygen at 5×10^{-7} Torr for various

Figure 2 shows the normalized photoelectron spectra of the pre-oxidized Zn sample before and after exposing to oxygen at 5×10^{-7} Torr for various exposure times at the sample temperature of 50°C . The effect of oxygen exposure can clearly be observed from a series of the spectra in Fig. 2. There are the variations of the shape and magnitude of the peaks associated with Zn 3d and of the valence band spectra below $\sim 9\text{-eV}$ binding energy. With increasing exposure time, there are the high binding-energy shift and the decrease in magnitude of the 10.5 and 9.9 eV Zn 3d associated peaks, respectively. In addition, there are the increase of a broad lump in the 3 eV to 9 eV binding energy region and the reduction of the Zn 4s DOS near the Fermi level. Those changes indicate that metallic Zn atoms react with oxygen and transform to ZnO upon oxygen exposure.

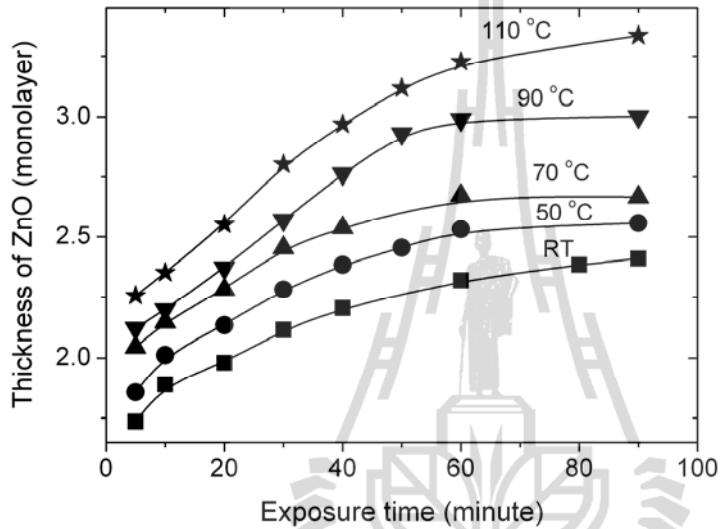


Figure 3. Thickness of the ZnO overlayer after exposing a Zn foil to oxygen at 5×10^{-7} Torr for various time.

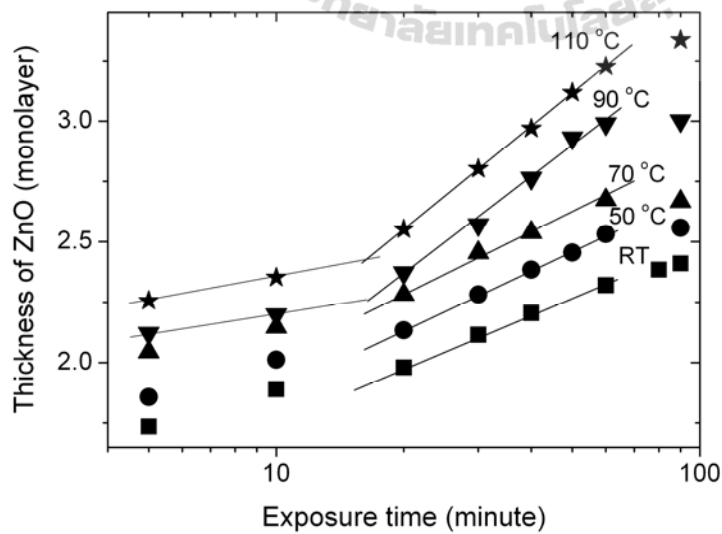


Figure 4 Thickness of the ZnO overlayer after exposing a Zn foil to oxygen at 5×10^{-7} Torr for various time plotted with logarithm of time.

Figure 3 shows the amount, or equivalent thickness, of ZnO formed on the Zn foil for various oxygen exposures and different sample temperatures can be estimated from the ratio of the Zn 3*d* electrons emitted from ZnO and the total emitted Zn 3*d* electrons. The detailed description of the calculations is reported elsewhere [14]. The calculation is based on the fact that a photoelectron spectrum of ultra-thin films of ZnO on Zn metal is collective of photoelectrons emitting from both the oxide overlayer and the underlying Zn metal. From the inelastic mean free path of an electron in ZnO and Zn, one can estimate the ratio of the intensity of Zn 3*d* electrons emitting from a ZnO layer to the total intensity of Zn 3*d* electron emitting from the ZnO with a given thickness and the underlying Zn metal. At oxidation temperatures below 110°C, the thickness of ZnO increases quickly with exposure time in the beginning and trend to saturate after certain amount of ZnO was formed. At room temperature, the oxide thickness trends to saturate at ~2.4 monolayers, which is close to the thickness of ~2.2 monolayers of the ZnO formed from a clean Zn surface without pre-oxide overlayer reported previously [14]. The saturated thickness appears to increase with oxidation temperature.

Figure 4 shows the ZnO thickness plotted with logarithm of time. Below the saturate thickness, the oxidation rate conforms to a two-stage logarithmic equation. For the oxidation at 90°C and above, the oxidation rate for the second stage is much higher than that for the first stage. For lower oxidation temperatures, this rate decreases. The results show that oxidation of Zn at very low partial pressure and at low temperature still has similar two-stage logarithmic oxidation behavior as oxidation of Zn and other metals at the atmospheric pressure [16-18]. This implies that the initial oxidation of Zn at very low partial pressure and at low temperature may be explained with a similar assumption that the oxidation process is governed by two kinds of space charge presumably formed in the thin oxide overlayer. This explanation is normally used for the oxidation of metals at the atmospheric pressure [16-18].

4. Conclusions

Oxidation of polycrystalline Zn foils at 5×10^{-7} Torr oxygen pressure and at low temperature has been investigated. Initially, the oxidation rate follows a two-stage logarithmic equation and later trend to saturate at a certain thickness depending on oxidation temperature. The saturate thickness was found to increase with oxidation temperature. The explanation for the oxidation of metals at atmospheric pressure may also be used for the explanation of the oxidation of Zn at very low partial pressure of oxygen and at low temperature.

5. References

1. C. Klinshim, Phys. Status Solidi B 71 (1975) 547.
2. D.C. Look, B. Claflin, Phys. Status Solidi, B Basic Res. 241 (2004) 624.
3. A.B. Djuricic, Y. Chan, E.H. Li, Mater. Sci. Eng. 38R (2002) 237.
4. K. Ellmer, J. Phys. D: Appl. Phys. 34 (2001) 3097.
5. Y.F. Chen, D. Bagnall, T. Yao, Mater. Sci. Eng. 75B (200) 190.
6. D.C. Look, Mater. Sci. Eng. 80B (2001) 383.
7. Y.G. Wang, S.P. Lau, H.W. Lee, S.F. Yu, B.K. Tay, X.H. Zhang, H.H. Hng, J. Appl. Phys. 94 (2003) 354.
8. Z.W. Li, W. Gao, R.J. Reeves, Surf. Coat. Technol. 198 (2005) 319.
9. Ya.I. Alivov, A.V. Chernykh, M.V. Chukichev, R.Y. Koratkov, Thin Solid Films 473 (2005) 241.
10. S. Cho, J. Ma, Y. Kim, Y. Sun, G. K.L. Wong, J.B. Ketterson, Appl. Phys. Lett. 75 (1999) 2761.
11. J. Zhao, L. Hu, Z. Wang, Y. Zhao, X. Liang, M. Wang, Appl. Surf. Sci. 229 (2004) 311
12. W.N. Unertl, J.M. Blakely, Surf. Sci. 69 (1977) 23 and reference therein.
13. I. Abbati, L. Braicovich, R.A. Powell, Surf. Sci. 87 (1979) L243 and references therein.
14. S. Noothongkaew, R. Supruangnet, W. Meevasana, H. Nakajima, S. Limpijumnong, P. Songsiriritthigul, Appl. Surf. Sci. 256 (2009) 980.
15. P. Songsiriritthigul, B. Kijornrattanawanich, A. Tong-on and H. Nakajima, Nucl. Instru. Methods Phys. Res. A, 82 (2007) 100.
16. H. H. Uhlig, Acta Met., 4 (1956) 541.
17. Vincent O. Nwoko and H. H. Uhlig, J. Electrochem. Soc., 12 (1965) 1181.
18. Y. Ohbuchi, T. Kawahara, Y. Okamoto and J. Morimoto, *Japan. J. Appl. Phys.*, 39, 5A, (2000), 2665.

CURRICULUM VITAE

Name: Miss. Suttinart Noothongkaew

Date of Birth: 30 November 1977

Place of Birth: Suratthani, Thailand

Nationality: Thai

Education Background:

1996-2000 Ramkhumhang University, Bangkok, Thailand.

Bachelor of Science (Physics)

2000-2003 King Mongkut's Institute of Technology Ladkrabang, Bangkok, Thailand.

Master of Science (Applied Physics)

Work Experience

2003 Aksorn Charoentat Act. Co., Ltd., Bangkok, Thailand.